NOVEL LASER BEAMS FOR OPTICAL TRAPPING AND TWEEZING

By

Yaseera Ismail

A dissertation submitted in fulfilment of the academic requirements for the degree of Master of Science in the School of Physics, University of KwaZulu-Natal, Durban.

Supervisor:
Prof. Andrew Forbes

September 2011

Abstract

Optical trapping and tweezing has been around for the last 30 years and since found its place in the fields of physics and biology. Over the years this technique has advanced exceedingly and is a unique tool to carry out research in the micrometre and nanometre scale regime. The aim of this dissertation was to illustrate that an optical trapping and tweezing system is an effective tool for the manipulation of micron sized particles and that using such a system allows one the ability to accurately and precisely measure optical forces in the piconewton scale. A custom built single gradient optical trapping system was built to illustrate the manipulation of micron sized particles. Here we will highlight some of the key components of such a system and give an explanation of how these components affect the optical trap. To enhance this system, we exploit the ability to shape light and in particular laser light to generate novel laser beams. This was achieved using a diffractive optical element known as a spatial light modulator (SLM).

A spatial light modulator is an electronically addressed optical element which when incorporated into an optical system effectively manipulates the phase of light in order to generate various novel laser beams. In particular these novel laser beams include Laguerre-Gaussian, Bessel and recently proposed Bessel-like beams. Each of these beams contains interesting properties which can be beneficially exploited. Laguerre-Gaussian beams are particularly known as ‘donut’ shaped beams since they have a central dark hole. Increasing the order of these Laguerre-Gaussian beams leads to an increase in the central dark region. These beams are of particular interest since they carry orbital angular momentum. This is not easily observed; however, when incorporated into the optical trapping system, leads to the rotation of trapped particles due to the transfer of photons carrying orbital angular momentum. Bessel and Bessel-like beams on the other hand are classes of beam that possess interesting non-diffracting and self-reconstructive properties upon encountering an obstacle. Here the generation and properties of these novel laser beams will be discussed in detail. Furthermore it is well known that these novel laser beams prove highly useful when incorporated into an optical trapping system hence we will illustrate the effects on a trapped particle when incorporating a Laguerre-Gaussian beam carrying a topological charge of one. It is expected that the trapped particle should rotate due to the transfer of orbital angular momentum.

The knowledge gained from beam shaping and the means to trap micron sized particles optically allows one the ability to incorporate this technique in a number of fields, including the promising field of microfluidics. This is an emerging field that deals with investigating fluid properties at the nano and microlitre regime. Optical tweezers integrated into a microfluidic device are beneficial since they are an adequate tool for measuring fluid flow using Stokes' Law.

Declaration 1

The experimental work described in this dissertation was carried out at the Council for Scientific and Industrial Research, National Laser Centre, while registered with the School of Physics, University of KwaZulu-Natal, Durban, Westville, from February 2010 to September 2011, under the supervision of Professor Andrew Forbes.

These studies represent original work by the author and have not otherwise been submitted in any form for any degree or diploma to any tertiary institution. Where use has been made of the work of others it is duly acknowledged in the text.

Signed:_____

On this_____day of_____2011

As the candidate's supervisor I have approved this dissertation for submission.

_____

Prof Andrew Forbes

On this_____day of_____2011

Declaration 2 - Plagiarism

I, ……. declare that

1. The research reported in this thesis, except where otherwise indicated, is my original research.

2. This thesis has not been submitted for any degree or examination at any other university.

3. This thesis does not contain other persons' data, pictures, graphs or other information, unless specifically acknowledged as being sourced from other persons.

4. This thesis does not contain other persons' writing, unless specifically acknowledged as being sourced from other researchers. Where other written sources have been quoted, then:
   a. Their words have been re-written but the general information attributed to them has been referenced
   b. Where their exact words have been used, then their writing has been placed in italics and inside quotation marks, and referenced.

5. This thesis does not contain text, graphics or tables copied and pasted from the Internet, unless specifically acknowledged, and the source being detailed in the thesis and in the References sections.

Signed: ……

Declaration 3 – Publications

Peer-Reviewed Journal Papers:

Y. Ismail, G. Barnes, T. Mhlanga, V. Belyi and A. Forbes, "Shape invariant higher-order Bessel beams," Optics Communications, "Submitted August 2011"

International Conference Papers:

Y. Ismail, G. Barnes, T. Mhlanga, V. Belyi and A. Forbes. Long rang quasi-nondiffracting beams carting orbital angular momentum. International Conference on Orbital Angular Momentum, March 2010, York

Y. Ismail, G. Barnes, T. Mhlanga, V. Belyi and A. Forbes. Higher-Bessel like beams with z-dependent cone angles, Proceedings of SPIE: Laser Beam Shaping XI, doi: 10.1117/12.863345, Vol. 7789 77890C, August 2010, San Diego, United States of America

National Conference Papers:

Y. Ismail, M. G. McLaren and A. Forbes, Optical trapping and tweezing using a spatial light modulator. 2nd African Laser Centre workshop 2009, Kariega, South Africa

Y. Ismail, M. G. McLaren and A. Forbes, Optical trapping and tweezing using a spatial light modulator. 55th South African Institute of Physics conference 2009, University of KwaZulu-Natal, Durban, South Africa

Y. Ismail, R. Rop and A. Forbes, Non-diffracting light. 3rd African Laser Centre workshop, Stellenbosch 2010, South Africa

Y. **Ismail** and A. Forbes, Z-dependent Bessel-like beams. 55th Annual South African Institute of Physics conference 2010, National Laser Centre, Pretoria, South Africa

Y. **Ismail** and A. Forbes, Accurately and precisely determining the strength of an optical trap. 56th Annual South African Institute of Physics conference 2011, UNISA, Pretoria, South Africa

Signed: ……

Table of Contents

List of Tables

List of Figures

expander consisting of lenses L_1 and L_2. The beam was thereafter directed by mirrors M_3 and M_4 into the vertical axis of the trap onto a dichroic mirror which reflected the laser light into a 100x LOMO objective lens onto a stage. The stage held the sample which was illuminated by a Köhler illumination system made up of L_3, L_4 and L_5. A tube lens L_T was used to collect the light that was imaged onto a Scorpion IEEE 1394 CCD camera (model SCOR-20S0).

6.2 Microscope slide containing the sample of silica beads 4 μm diameter in distilled water.

6.3 Illustration of the sample on the microscope slide where the depth of the well the sample is placed in is 100 μm.

6.4 Optical trapping system as set up in the laboratory: the beam passes through two mirrors onto the dichroic mirror which directs the beam into the 100x microscope objective lens. The sample is illuminated below and captured by a Scorpion IEEE 1394 CCD camera (model SCOR-20S0).

6.5 Experimental image of a trapped particle (in focus) surrounded by un-trapped particles (out of focus).

6.6 Manipulation of a trapped particle in triangular movement: the particle is first trapped (a), thereafter movement of the laser beam causes a movement of the particle (b), where the white circle is the position to which the particle was moved while the red dashed circle indicates the position the particle was previously at. This movement is further seen in (c) and (d), whereby the particle was almost returned back to its original position.

6.7 Movement stage while keeping the trapped particle fixed: in frame (a) the trapped particle is represented by a blue circle while a surrounding particle is marked with a red cross. After the movement of the stage (b) we observe that the trapped particle is still at the same position however the surrounding particle marked with the cross has been displaced from its initial position.

6.8 Plot representing the drag force method showing the effects the trapping power has on the trapping force.

6.9 The particle distribution representing the displacement of a trapped particle from its equilibrium position.

6.10 Plot representing the equipartition method showing the effects the trapping power has on the trapping force.

Acknowledgements

My deepest gratitude goes out to my supervisor Prof Andrew Forbes. Thank you for all the time and effort that has been sacrificed to ensure my project stayed afloat. I know the long road that has led to this point had been really bumpy yet you still managed to retain faith in my project so a heartfelt thanks to you. I don't think it is possible to reach one's goals as an individual; there is always a point in life that we tend to turn to others for advice to help us along our path so to everyone within the Mathematical optics group, who were always willing to lend a helping hand, thank you. Sincere thanks also go out to the CSIR-National Laser Centre for allowing me the opportunity to use their facilities to carry out the research presented in this thesis.

A special thanks go out to my family, the most important people in my life, for motivating me every step of the way. I know my master's was a huge step with lots of adjustments however thanks to all of you for allowing me to make my own decisions and always trusting I made the correct ones. Without all of the constant encouragement and support I would not have reached this point. I am eternally grateful to all of you for constantly believing in me.

I must admit the life of every experimentalist tends to be really stressful at times so a heartfelt thanks to my friends at the National Laser Centre who seemed to always find a way of adding some positivity to each and every day. Thanks for all of the motivational as well as very insightful conversations. Every one of you have added value to each day making it easier to get through the enduring times.

During the end, while writing my thesis I found myself being pulled into fruitful conversations about philosophy which makes one search for the inner meaning of life so I think it's best to end on philosophical note to keep one thinking from the father of science himself, Albert Einstein, "The intellect has little to do on the road to discovery. There comes a leap in consciousness, call it intuition or what you will, and the solution comes to you and you don't know how or why..."

Chapter 1

Introduction

Since the first optical trap, discovered over 30 years ago, optical trapping and tweezing has become a well known application to manipulate micron size particles without physical contact. Optical trapping found its place in the world of physics in the early 1960s when Authur Ashkin and colleagues at Bell Laboratories discovered that micron sized particle could be trapped and levitated in the medium of air and water by the use of counter propagating laser beams (Ashkin, 1970). Upon the attempt to further develop this application they discovered the first three dimensional single gradient optical trap, widely known as an optical tweezer (Ashkin *et al.*, 1986). Today optical tweezers are extensively studied both in the fields of physics and biology.

For a biologist this application is useful to trap bacteria and viruses and understanding the limitations of trapping at the single cellular level. On the other hand to a physicist optical tweezing opens a window to determine piconewton forces (Rohrbach & Stelzer, 2002). There are two influential forces that act on a dielectric particle that determines the ability of the particle to be trapped, namely the scattering force which acts in the direction of radiation pressure and pushes the particle along the propagation of the beam of light and the gradient force that acts in the direction of the intensity gradient of the beam of light. A stable trap is achieved when the gradient force exceeds the scattering force. Due to the advancement of technology today, precise and accurate methods can be used to determine these forces, which will be dealt with in section 4.4.

Apart from building a single gradient optical trap for the manipulation of single particle, it is possible to build novel traps which are made possible by incorporating a spatial light modulator into an optical trapping system. A spatial light modulator is a diffractive optical element that is electronically addressed. Incorporating a spatial light modulator into an optical trapping system will

allow one the ability to not restrict trapping to a single particle at a time since it is useful tool for producing an array of optical traps that can be individually controlled (Mellville *et al.*, 2003).

A spatial light modulator can serve other purposes within an optical trap and in particular it allows for versatile beam shaping. Beam shaping using diffractive optics allows for the generation of various types of novel laser beams which will be mentioned in chapter three; those that will be discussed include Laguerre-Gaussian beams that carry orbital angular momentum and Bessel beams which are non-diffracting in nature. Each of these beams has their own interesting properties which can add value to an optical trap. Incorporating these novel beams into an optical trap leads to the advancement of the trap. Instead of just three dimensional manipulation of a trapped particle, it is also possible to rotate or spin particles.

Here we will discuss the procedure to build a single gradient optical trap and use the advancements in fast speed video microscopy to accurately and precisely calibrate the trap. We will look at the generation of novel laser beams using a spatial light modulator especially the generation of Bessel beams and consider an entirely new concept of producing Bessel-like beams with z-dependent cone angles. We will take this a step further and consider the transfer of orbital angular momentum (OAM) to a trapped particle when trapping with a Laguerre-Gaussian beam by incorporating a spatial light modulator into the optical trapping system.

Chapter 2

Laser Beam Propagation

Light is described in terms of electromagnetic radiation which is a form of energy that displays wave-like behaviour as it travels through space. Electromagnetic radiation has both an electric and a magnetic component which oscillate perpendicular to each other and perpendicular to the direction of energy propagation. There exist numerous sources of light however of particular interest is the propagation of laser light. Laser light is monochromatic and directional and it is known to have a high degree of spatial and temporal coherence unlike white light that diverges rapidly as it propagates. Most lasers are built such that they emit a beam with an approximate Gaussian intensity profile. In order to determine the field of a Gaussian beam one can consider two approaches: either using the Fresnel diffraction equation or by solving the time independent Helmholtz equation (Siegman, 1986). By considering the Helmholtz approach we can show that the field of a Gaussian beam consist of the following parameters: beam width, Rayleigh range and beam divergence. There exist other solutions to the Helmholtz equation which include Laguerre-Gaussian beams, Hermite-Gaussian beams (Kogelnik and Li, 1966), Mathieu beams (Gutierrez-Vega *et al.*, 2000) and Ince-Gaussian beams (Bandres & Gutierrez–Vega 2004a; Bandres & Gutierrez–Vega, 2004b). We choose the Helmholtz approach as the appropriate starting point which is discussed in the section that follows.

2.1 General Solution to the Time Independent Helmholtz Equation

The time independent Helmholtz equation consists of all scalar quantities and reads as

$$\nabla^2 E(r,z) - 2ik\frac{\partial}{\partial z}E(r,z) = 0, \tag{2.1}$$

where $E(r,z)$ is the electric field in the radial direction, k is the wave number and ∇^2 is the Laplacian which is given by

$$\nabla^2 = \frac{\partial^2}{\partial x^2} + \frac{\partial^2}{\partial y^2} + \frac{\partial^2}{\partial z^2}. \tag{2.2}$$

Applying the Laplacian to the electric field yields an explicit form of the Helmholtz equation expressed as

$$\frac{\partial^2}{\partial x^2}E(r,z) + \frac{\partial^2}{\partial y^2}E(r,z) + \frac{\partial^2}{\partial z^2}E(r,z) - 2ik\frac{\partial}{\partial z}E(r,z) = 0. \tag{2.3}$$

The paraxial approximation is defined by the condition $\partial^2 E(r,z)/\partial z^2 << k\partial E(r,z)/\partial z$ which means that the longitudinal variation in the modulation function $E(r,z)$ changes very little in the wavelength associated with beam $2\pi/k$. In this approximation the third term in Eq. (2.3) can be neglected, the equation simplifying to

$$\frac{\partial^2}{\partial x^2}E(r,z) + \frac{\partial^2}{\partial y^2}E(r,z) - 2ik\frac{\partial}{\partial z}E(r,z) = 0. \tag{2.4}$$

In order to solve for the electric field in Eq. (2.4), a simple trial solution is considered in the form of a Gaussian envelope as

$$E(r,z) = E_0 \exp(-P(z)) \exp\left(\frac{ikr^2}{2q(z)}\right), \tag{2.5}$$

where $r^2 = x^2 + y^2$, E_0 is the initial electric field and $P(z)$ and $q(z)$ are analytic functions of z. We substitute the trial solution, Eq. (2.5), into Eq. (2.4) and we thus arrive at a form that is easily differentiable

$$\frac{\partial^2}{\partial x^2}E_0\exp(-P(z))\exp\left(\frac{ikr^2}{2q(z)}\right)+\frac{\partial^2}{\partial y^2}E_0\exp(-P(z))\exp\left(\frac{ikr^2}{2q(z)}\right)$$
$$-2ik\frac{\partial}{\partial z}E_0\exp(-P(z))\exp\left(\frac{ikr^2}{2q(z)}\right)=0. \tag{2.6}$$

Carrying out the necessary differentials the field can be simplified as given by

$$E_0\left\{\left[\left(\frac{-2ik}{q(z)}-\frac{k^2r^2}{q^2(z)}\right)\exp\left(\frac{\mathrm{ikr}^2}{2\,\mathrm{q(z)}}\right)\exp(-\mathrm{P(z)})\right]\right\}$$
$$-E_0\left\{2ik\left[\left(\frac{ikr^2}{2q(z)}\frac{\partial}{\partial z}q(z)-i\frac{\partial}{\partial z}P(z)\right)\exp(-\mathrm{P(z)})\exp\left(\frac{\mathrm{ikr}^2}{2\,\mathrm{q(z)}}\right)\right]\right\}=0. \tag{2.7}$$

After some re-arranging in order to group all the common terms the field can be expressed as

$$E_0\left\{\left[\frac{-2ik}{q(z)}-\frac{k^2r^2}{q^2(z)}+\frac{k^2r^2}{q(z)}q'(z)+2kP'(z)\right]\exp(-\mathrm{P(z)})\exp\left(\frac{\mathrm{ikr}^2}{2\,\mathrm{q(z)}}\right)\right\}=0. \tag{2.8}$$

For the above equation to hold true it can be clearly seen that all the terms within the square brackets have to equal zero

$$-2kP'(z)-\frac{2ik}{q(z)}-\frac{k^2r^2}{q(z)}[1-q'(z)]=0. \tag{2.9}$$

For an arbitrary r the above equation can be separable into two parts such that an expression for $q'(z)$ and $P'(z)$ can be determined

$$1-q'(z)=0\Rightarrow q'(z)=1, \tag{2.10}$$

and

$$2kP'(z)+\frac{2ik}{q(z)}=0\Rightarrow P'(z)=-\frac{i}{q(z)}. \tag{2.11}$$

It is well known that $q(z)=z+iz_R$ hence the derivative of the analytic function $P(z)$ is given as

$$P'(z) = -\frac{i}{z + z_R}, \tag{2.12}$$

which can be integrated to give $P(z)$ as

$$\frac{\partial}{\partial z} P(z) = -\frac{i}{z + iz_R} = -i\frac{\partial}{\partial z}\frac{1}{z + iz_R} = -i\frac{\partial}{\partial z}\ln[z + iz_R] \Rightarrow P(z) = -i\ln[z + iz_R]. \tag{2.13}$$

By inverting the term $q(z) = z + iz_R$ we can further write this term as

$$\frac{1}{q(z)} = \frac{1}{R(z)} - \frac{2i}{kw^2(z)}. \tag{2.14}$$

The term $P(z)$ can be simplified such that it takes the form of the phase of the field seen below

$$\begin{aligned} P(z) &= -i\ln[z + iz_R] \\ &= -i\left[\ln(z^2 + z_R^2) - \tan^{-1}\left(\frac{z_R}{z}\right)\right] \end{aligned} \tag{2.15}$$

$$\exp(-iP(z)) = \frac{\exp\left[-i\tan^{-1}\left(\frac{z_R}{z}\right)\right]}{z\sqrt{1 + \frac{z^2 + z_R^2}{z^2}}} \tag{2.16}$$

By substituting the results obtained in Eq. (2.16) into the trial solution Eq. (2.5) and assuming by definition the expression for the radius of curvature and beam width is known the field can be expressed as

$$E(r,z) = E_0\frac{w_0}{w(z)}\exp(-i\zeta(z))\exp\left[-\frac{ikr^2}{2R(z)}\right]\exp\left[-\left(\frac{r}{w(z)}\right)^2\right] \tag{2.17}$$

where $\zeta(z) = \tan^{-1}(z_R/z)$ is the Gouy phase term, $R(z)$ is the radius of curvature and $w(z)$ is the beam width.

2.2 Gaussian Beam Propagation

A Gaussian beam is propagation invariant which means it retains its spatial distribution as it propagates in free space, however there in a change is size as illustrated in Fig. 2.1.

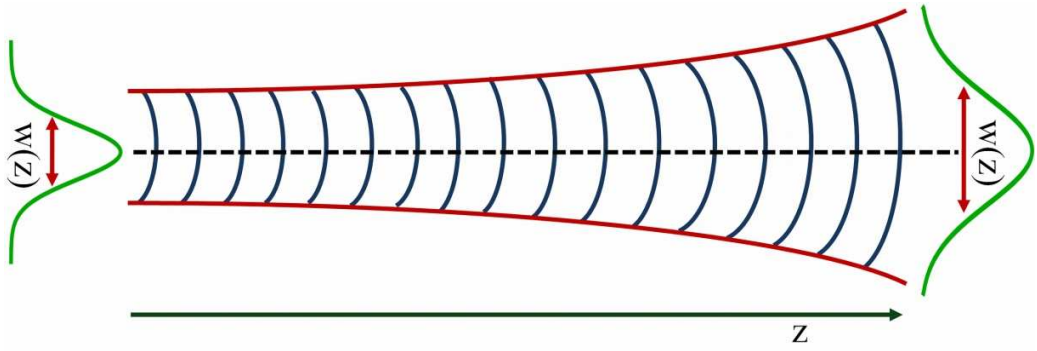

Fig. 2.1 Propagation of a Gaussian beam in free space along the optical axis.

In order to determine the geometric properties of a Gaussian beam, each of the parameters mentioned in Eq. (2.17) have to be considered individually (Saleh & Teich, 1991). We consider a Gaussian beam propagating in free space with respect to the optical axis, where the width of the beam varies as a function of the propagation distance *z* as

$$w(z) = w_0\sqrt{1+\left(\frac{z}{z_R}\right)^2} \tag{2.18}$$

where *z* is the propagation distance and w_0 is the beam waist and z_R is the Rayleigh range. The Rayleigh range is the distance along the direction of propagation from the beam waist to the point at which the cross sectional area of the beam is doubled (See Fig. 2.2) and is given as $z_R = \pi w_0^2 / \lambda$, where λ is the wavelength. As observed, the Rayleigh range is directly dependent upon the beam waist and inversely proportional to the wavelength. As the propagation distance increases the beam width Eq. (2.18) increases linearly, further seen by the dashed line in Fig. 2.2. Clearly w_0 is the point at which the beam width is at its minimum when $z = 0$.

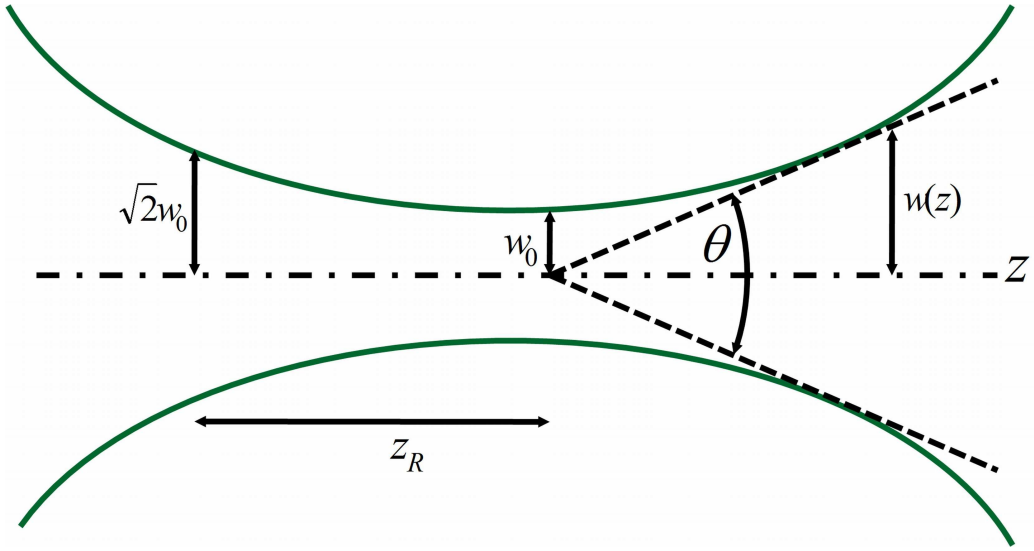

Fig. 2.2 Geometrical interpretation of the beam width with respect to propagation distance.

It is not only the size of the beam that changes with an increase in propagation distance, there is also a change in wavefront of a Gaussian beam which can be expressed in terms of the radius of curvature given as

$$R(z) = z\sqrt{1+\left(\frac{z_R}{z}\right)^2}. \tag{2.19}$$

Similar to the width of the beam, the radius of curvature is dependent on the Rayleigh range and the propagation distance. As z tends to infinity, the radius of curvature changes linearly with respect to z hence the wave-front is planar as observed in Fig. 2.3.

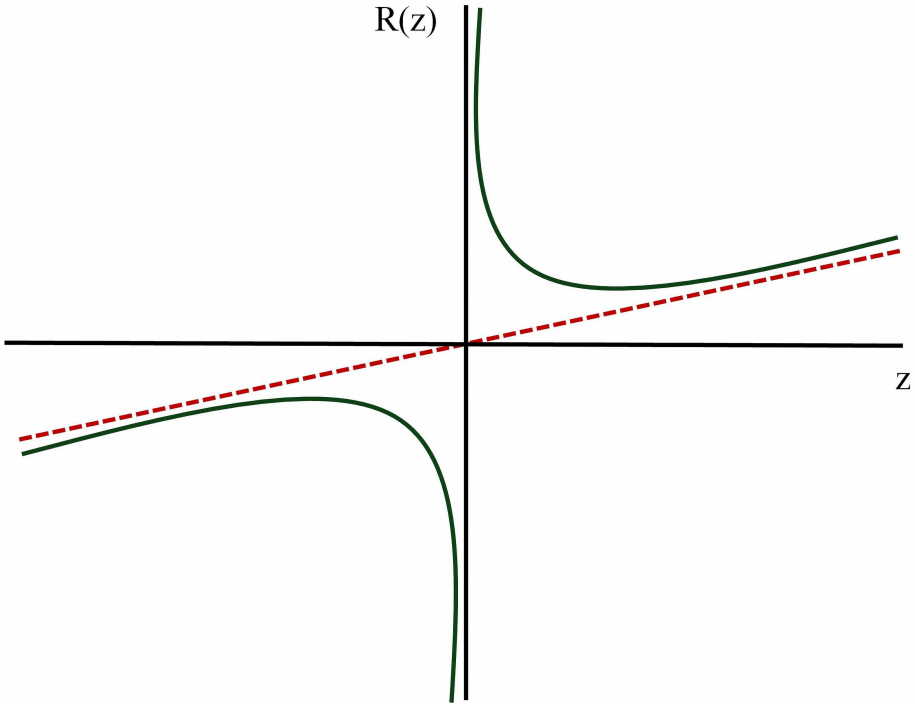

Fig. 2.3 The following plot illustrates a flat radius of curvature as z tends to infinity, the radius of curvature is infinite at z=0.

Consequently when the propagation distance is equivalent to the Rayleigh range then the beam width Eq. (2.18) increases to $\sqrt{2}w_0$ which shows that the beam width is larger than the beam waist by a factor $\sqrt{2}$. The radius of curvature on the other hand is infinite at the beam waist. The divergence of a Gaussian beam is also related to the Rayleigh range such that once the limit of $z >> z_R$ is reached, the beam would diverge rapidly and is defined by

$$\theta \cong \frac{w(z)}{z} = \frac{\lambda}{\pi w_0}. \tag{2.20}$$

Furthermore we identify that the phase of a Gaussian beam can be determined by considering the Gouy phase term which describes the $\pi/2$ phase shift once the beam crosses the beam waist which is defined by

$$\zeta(z) = \tan^{-1}\left(\frac{z}{z_R}\right). \tag{2.21}$$

This Gouy phase term has to be taken into account when information about the wavefront is required as illustrated in Fig. 2.4. Noticeably the phase is zero at $z = 0$ and increases asymptotically towards a value of $\pi / 2$ as the propagation distance increases.

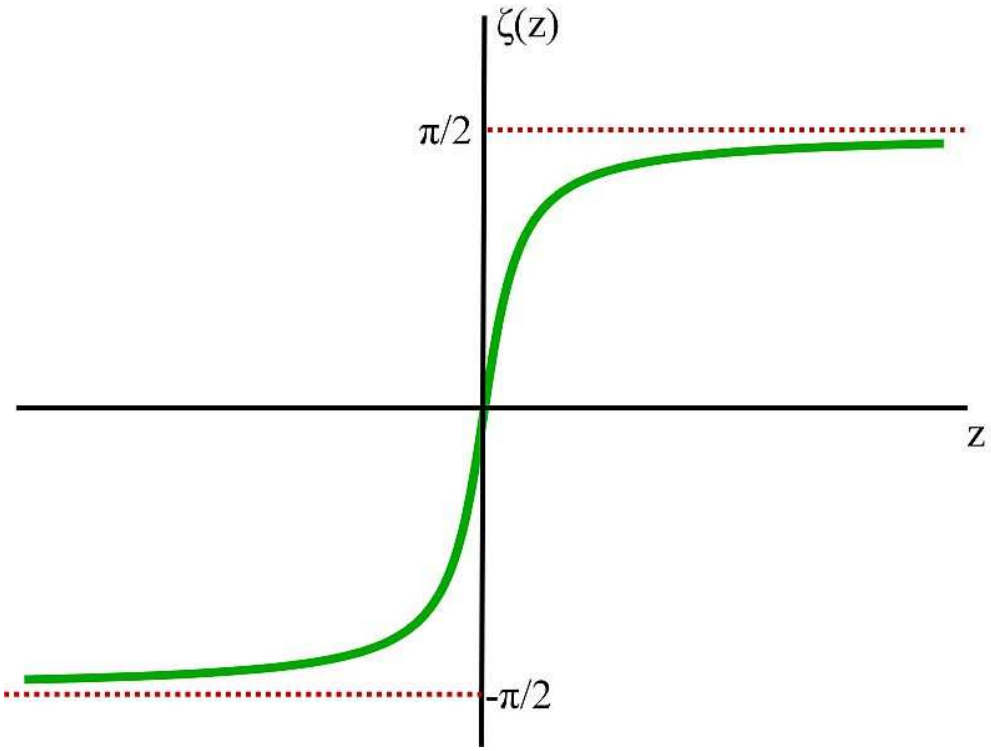

Fig. 2.4 The Gouy phase undergoes a $\pi / 2$ shift upon crossing the beam waist.

Since we have dealt with all the parameters of a Gaussian beam we now look to simplify the field even further. Since it is the intensity of the field that is observed in most experimental setups, instead of the electric field, taking the absolute square of the electric field Eq. (2.17) denotes the intensity of a Gaussian beam as defined as

$$I(r,z) = E_0 c|E(r,z)|^2 = I_0 \, exp\left[-2\left(\frac{r}{w(z)}\right)^2\right], \tag{2.22}$$

where E_0 and I_0 are the electric field and intensity of the beam at the beam waist respectively. This intensity distribution is further illustrated in Fig. 2.5. A Gaussian beam has the highest intensity at the peak (z=0) after which the intensity falls off to zero.

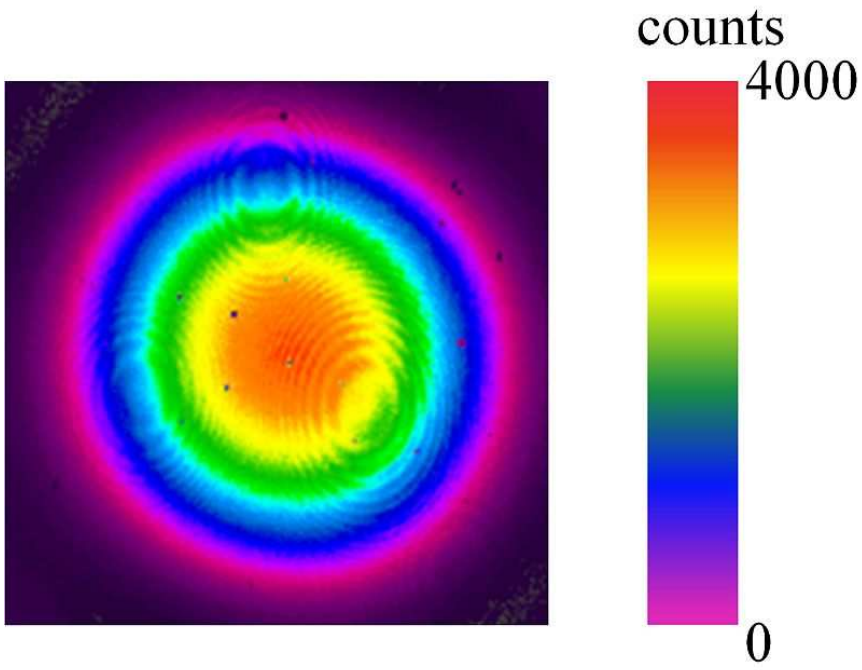

Fig. 2.5 The following represents the transverse intensity profile of a Gaussian beam.

To this point all the parameters to describe a Gaussian field were discussed with respect to free space propagation; however, in every optical system the field will also pass through various optics which include lenses and mirrors just to name a few. Hence to properly understand the propagation of a Gaussian beam within an optical system, the propagation of the field through an optical element should be considered. ABCD matrices are a ray tracing technique that can be used to design an optical system by tracing the light path through the system. Listed in Table 2.1 are the ABCD matrices of simple optical elements that a light beam can encounter (Kogelnik and Li, 1966).

Table 2.1 List of a few common ABCD matrices that a light beam would encounter.

Element	Diagram describing each ray transfer matrix	ABCD Matrix
(a) Propagation in free space where z is the propagation distance.	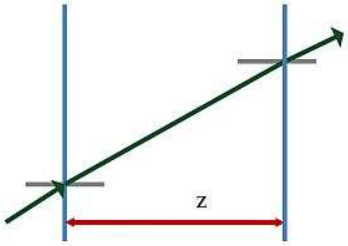	$\begin{bmatrix} 1 & z \\ 0 & 1 \end{bmatrix}$
(b) Thin lens whereby f is the focal length of the lens.	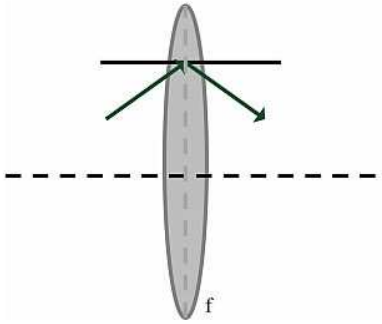	$\begin{bmatrix} 1 & 0 \\ -1/f & 1 \end{bmatrix}$
(c) Reflection from a planar mirror.	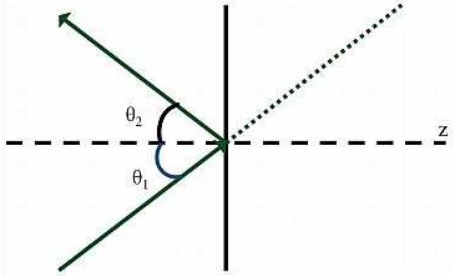	$\begin{bmatrix} 1 & 0 \\ 0 & -1 \end{bmatrix}$
(d) Refraction at a planar interface (n_1 and n_2 are the initial and final refractive indices respectively).	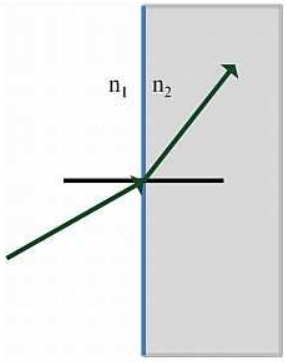	$\begin{bmatrix} 1 & 0 \\ 0 & n_1/n_2 \end{bmatrix}$

These ray transfer matrices are important for the understanding of how light rays are affected within an optical system. As an example, let us consider the effect of a light ray in free space. Since each ray is described in terms of position y and angle θ we can define the initial ray to have a position y_1 and an angle θ_1 passing through a system giving a final ray having a position y_2 and an angle θ_2 (See Fig. 2.6). To determine the position and angle of the final ray, we have to traverse through the system from right to left.

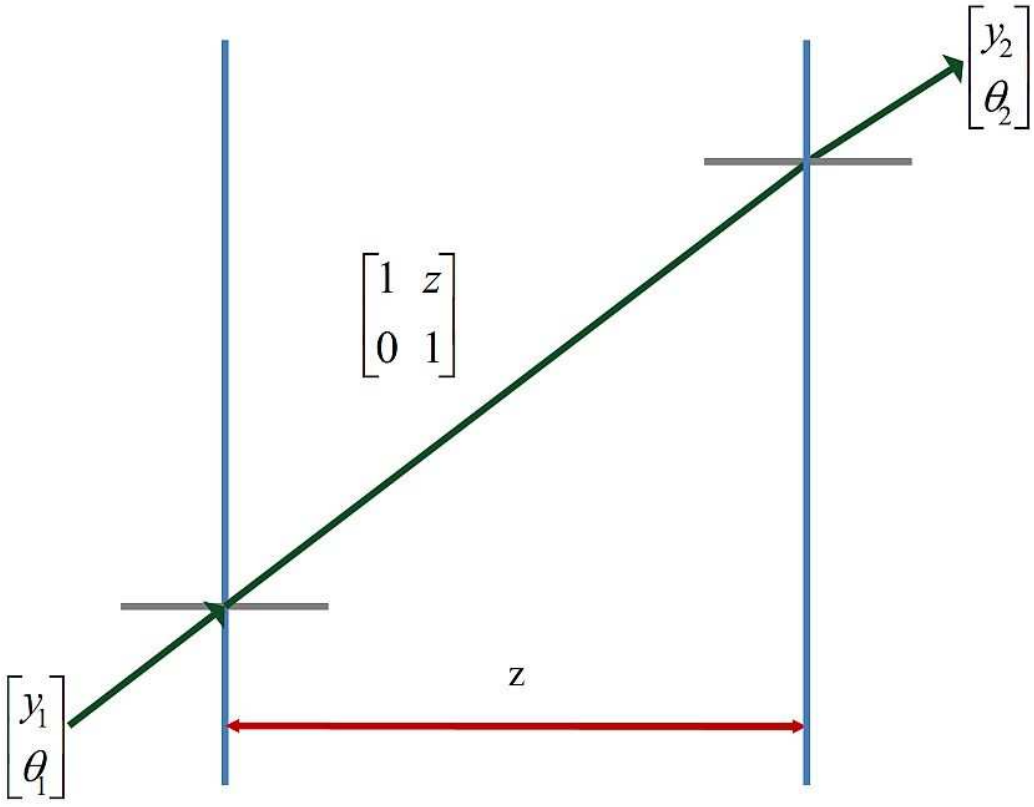

Fig. 2.6 The effects of a single light ray travelling through free space.

Hence to obtain the position and angle of the final ray we simply multiply the initial ray by the free space propagation matrix as seen below

$$\begin{bmatrix} y_2 \\ \theta_2 \end{bmatrix} = \begin{bmatrix} 1 & z \\ 0 & 1 \end{bmatrix} \begin{bmatrix} y_1 \\ \theta_1 \end{bmatrix}. \tag{2.23}$$

From the above equation, it is seen that the position of the final light ray is altered by $y_2 = y_1 + \theta_1 z$ while the direction of the ray remains the same, $\theta_2 = \theta_1$.

This approach can be carried out for the rest of the ray transfer matrices. The propagation of rays through a thin lens is the most familiar, Table 2.1(b) and can be used to determine the width of a beam. The ray transfer matrix for a thin lens is dependent upon the focal length of the lens, f. Since in the image depicts a biconvex (positive) lens, all the light rays passing through the lens will focus at a distance f away from the lens. Since most optical systems use mirrors to direct light rays, Table 2.1(c) illustrates the effects on a light ray upon encountering a planar mirror. For a planar mirror the light rays will enter at angle θ_1 and leave with an angle θ_2, where $\theta_1 = \theta_2$. When a light ray travels through two mediums of different refractive indices n_1 and n_2, Table 2.1(d), the ray will bend due to a change in the angle at the interface of the media.

So far we have considered free space propagation and next we will look at the effects an optical element will have on a beam. The obvious choice would be to look at the propagation of a beam through an optical lens hence we choose a thin lens. Referring to Fig. 2.7.the light rays are well collimated or in other words parallel to the optical axis upon encountering the lens of focal length, f and focused at a distance $z \approx f$ away from the lens.

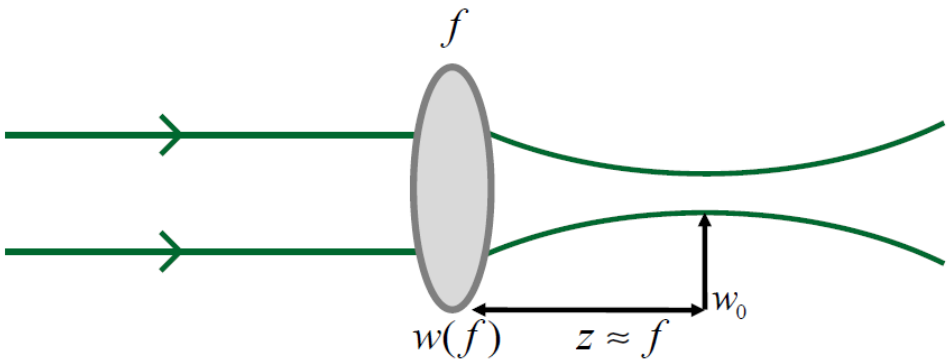

Fig. 2.7 Parallel light rays upon encountering a lens are focused a distance $z \approx f$ after the lens.

In order to determine the width of the beam at the focus of a thin lens we require information about the propagation of a beam through free space as well as through a thin lens which can be extracted from Table 2.1.

Multiplying these two matrices out gives an indication of the ABCD matrix for a beam travelling through a lens as seen below

$$\begin{vmatrix} 1 & z \\ 0 & 1 \end{vmatrix} \begin{vmatrix} 1 & 0 \\ -1/f & 1 \end{vmatrix} = \begin{vmatrix} 1-z/f & z \\ -1/f & 1 \end{vmatrix}. \tag{2.24}$$

The complex radius of curvature of a Gaussian beam can be written as

$$q_2 = \frac{Aq_1 + B}{Cq_1 + D}$$

$$= \frac{-iAz_R + z}{-iCz_R + 1}. \tag{2.25}$$

In order to eliminate the denominator in Eq. (2.25), q_2 is multiplied and divided by the complex conjugate and thereafter taking into consideration only the real values of q_2 yields

$$q_2 = \frac{-iAz_R + z}{-iCz_R + 1} \times \frac{iCz_R + 1}{iCz_R + 1},$$

and hence setting the real parts of q_2 to zero

$$q_2 = ACz_R^2 + z = 0. \tag{2.26}$$

From the ABCD matrix, it is clear that $A = 1 - z/f$ and $C = -1/f$, substituting these results into Eq. (2.26), we are able to solve for the propagation distance

$$z = \frac{z_R^2}{f} \times \frac{1}{\left[\frac{z_R^2}{f^2} + 1\right]}. \tag{2.27}$$

In order to eliminate all unwanted terms we multiply and divide by f^2 and divide out by z_R^2 which leaves a simplified expression for the propagation distance

$$z = \frac{f}{1+\left(\frac{f}{z_R}\right)^2}. \tag{2.28}$$

Substituting the result obtained for the propagation distance Eq. (2.28) into the expression of the beam width Eq. (2.18), yields the beam width at a distance $z \approx f$ given by

$$w(f) = w_0\sqrt{1+\frac{f}{z_R}}. \tag{2.29}$$

Recalling that the Rayleigh range is given by $z_R = \pi w_0^2/\lambda$ and substituting this into Eq. (2.29), results in the expression

$$w(f) = \frac{\lambda f}{\pi w_0}. \tag{2.30}$$

From Eq. (2.30), it is observed the width of the beam is dependent on the focal length of the lens and inversely proportional to the beam waist. This equation proves helpful when setting up an optical system, in allowing determination of the width of the beam at the focus of the beam. The propagation of a beam through a thin lens can also be used to determine an expression for the imaging equation. If an object is placed a distance d_0 in front of a thin lens, the image would appear a distance d_i away from the lens as seen in Fig. 2.8.

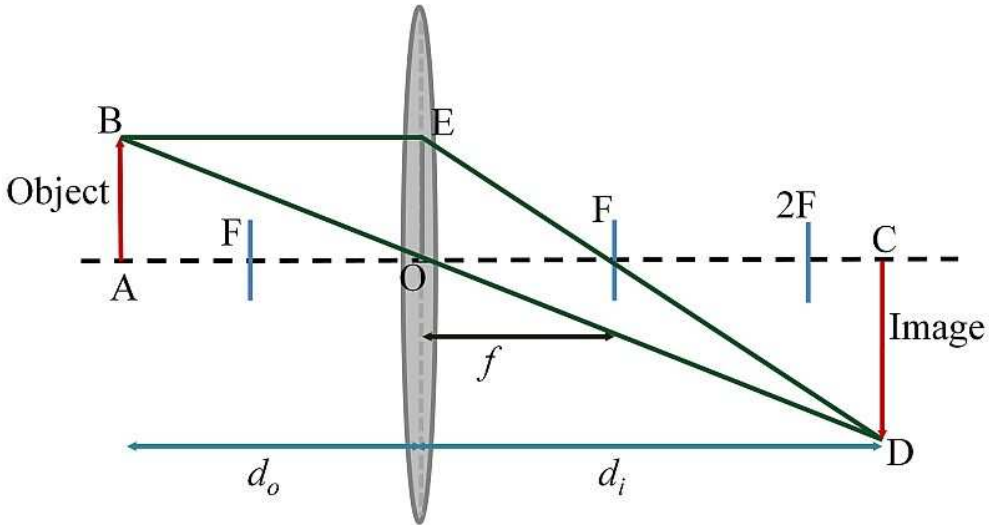

Fig. 2.8 Image of a beam through a thin lens illustrating the effects of imaging of an object.

For convenience, the object is labelled AB while the image of the object is represented by CD. F is the focal length of the lens and OE is the representation of the object at the lens. Now we find similar triangles to find the relation between the object and the image

In triangles EFO and DFC, using similar triangles, the ratio of the equal sides of the triangles can be written as $CD/EO = CF/OF$. This can be expressed in terms of the image distance, object distance and focal length as follows,

$$\frac{CD}{EO} = \frac{CF}{OF} = \frac{d_i - f}{f} = \frac{d_i}{f} - 1. \tag{2.31}$$

Similarly considering triangles DOC and AOE,

$$\frac{CD}{AB} = \frac{OC}{OB} = \frac{d_i}{d_o}. \tag{2.32}$$

Clearly it can be seen that $AB = OE$, hence both equations can be equated to give

$$\frac{d_i}{f} - 1 = \frac{d_i}{d_o}. \tag{2.33}$$

Upon dividing by the image distance and rearranging the terms, we end up with an expression for the imaging equation as

$$\frac{1}{f} = \frac{1}{d_i} + \frac{1}{d_o}. \tag{2.34}$$

Furthermore the magnification, m, can written as a ratio of the image to the object distance

$$m = \frac{d_i}{d_o}. \tag{2.35}$$

It was mentioned that lasers emit a beam width an approximate Gaussian profile. However there was no mention about the quality of the beam itself. This can be determined by measuring the beam quality factor M^2 which is determined by equating the M^2 with the product of the beam waist and the beam divergence

$$w_0\theta = \frac{M^2\lambda}{\pi}. \tag{2.36}$$

Experimentally the M^2 value is determined by measuring the width of the beam as it propagates upon passing through a thin lens of focal length f. Here for convenience a lens with a focal length of 300 mm was chosen and the beam width was measured from a distance 75mm in front of the lens to 600 mm away from the lens. By expanding Eq. (2.18) using the results obtained in Eq. (2.36) we attain a quadratic form of the beam width as given in Eq. (2.37) that can be easily plotted to determine the beam parameters.

$$w^2(z) = \frac{M^4\lambda^2}{w_0^2\pi^2}z^2 - \frac{2z_oM^4\lambda^2}{w_0^2\pi^2}z + \left(\frac{z_0^2M^4\lambda^2}{w_0^2\pi^2} + w_0^2\right). \tag{2.37}$$

By plotting the beam width with respect to the propagation distance, (see Fig. 2.9), and fitting a second order polynomial, the values for the coefficients in the polynomial in conjunction with the expression in Eq. (2.37) can be used to calculate the values of the beam waist, beam quality and z position of the waist using

$$M^2 = \frac{\pi w_0\sqrt{a}}{\lambda} \tag{2.38}$$

$$w_0 = \sqrt{c - \frac{b^2}{4a}} \tag{2.39}$$

$$z_0 = \frac{-b}{2a}. \tag{2.40}$$

Carrying out the necessary calculations, the beam width was measured to be 0.099 ± 0.002 mm, the beam quality was 1.148 ± 0.054 and the *z* position of the waist was 341.72 ± 0.21 mm. Since we expected that the field is a Gaussian distribution with a beam quality factor 1 and we measured the beam quality factor to be 1.148 ± 0.054 we can conclude that we have a good quality Gaussian beam.

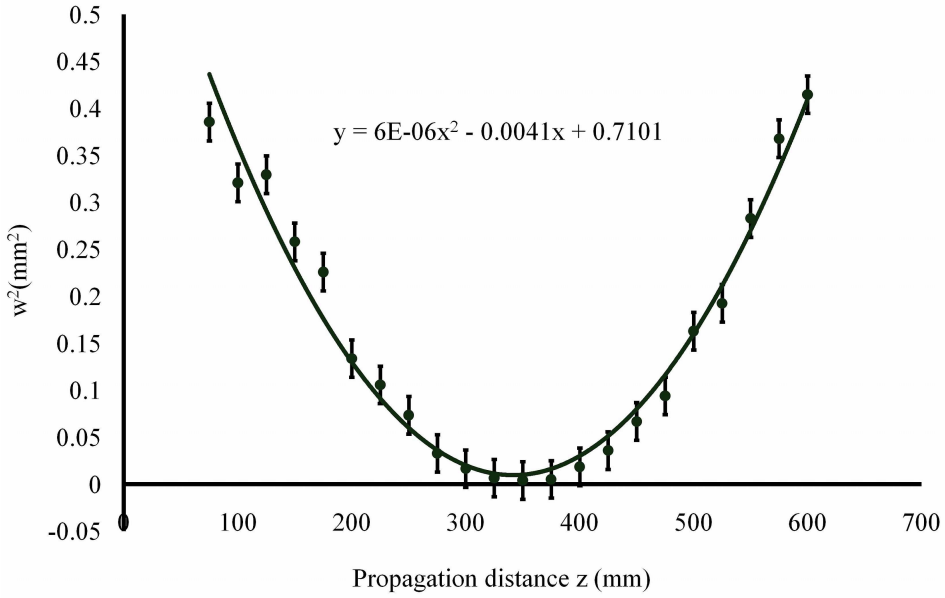

Fig. 2.9 Plot of the change in beam width due to an increase in propagation distance upon passing through a thin lens of focal length 300 mm.

CHAPTER 3

Novel Beams

3.1 Laguerre-Gaussian Beams

As previously mentioned there exist other types of laser beams which, like a Gaussian beam, also hold interesting properties. One such beam is that of a Laguerre-Gaussian field which is also a solution of the Helmholtz equation where the electric field is expressed as (Galvez, 2006)

$$E_p^{\ell}(r,\phi,z) = \left(\frac{\sqrt{2}r}{w(z)}\right)^{|\ell|} \exp\left(-\left(\frac{r}{w(z)}\right)^2\right) L_p^{\ell}\left(\frac{2r^2}{w^2(z)}\right) \exp\left(ik\frac{r^2}{2R(z)}\right) \times \exp(-il\phi) \times \exp(-i(2p+|\ell|+1)\zeta(z)). \tag{3.1}$$

As in the case of a Gaussian beam, most of the parameters retain their symbolism where $w(z)$ is the beam width, L_p^{ℓ} is the generalised Laguerre polynomial, and ℓ and p are the topological charge and the radial order respectively, $R(z)$ is the radius of curvature , $\zeta(z)$ is the Gouy phase shift and ϕ is the azimuthul phase. The term that contains the azimuthal phase, $\exp(i\ell\phi)$, is identified with the amount of orbital angular momentum carried by the beam. It has a quantized $2\pi\ell$ azimuthal phase and leads to an orbital angular momentum of $\ell\hbar$ per photon (Kennedy *et al.*, 2002). This is a general form of a Laguerre field and can be simplified to a Gaussian beam by setting the values of the topological charge and the radial order to zero. If considering the generalised case where the topological charge, ℓ, is non zero, varying the order of the topological charge while keeping the radial order fixed at zero leads to the generation of the different order Laguerre-Gaussian beams carrying integer amounts of orbital angular momentum.

To further understand this concept, consider the wavefront of a beam carrying a topological charge of one. Instead of being planar, the wavefront is helical in shape and the phase of the wavefront will vary phase from 0 to 2π once as seen in Fig. 3.1.

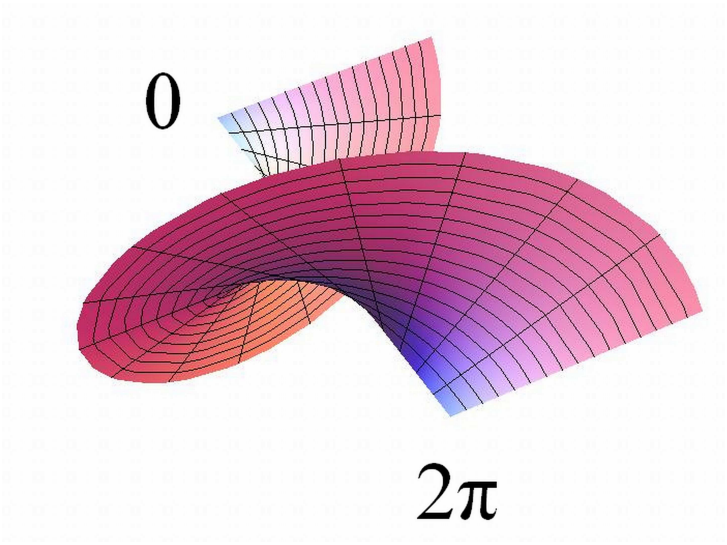

Fig. 3.1 Helical wave-front of a Laguerre-Gaussian beam showing one rotation from 0 to 2π.

Increasing the order of the topological charge leads to an increase in the number of cycles between 0 and 2π where these beams also possess an on axis zero intensity. This region of zero intensity as in the case of the orbital angular momentum is also dependent on the topological charge. By increasing the order of the topological charge the diameter of the region of zero intensity also increases and this is illustrated in Fig. 3.2.

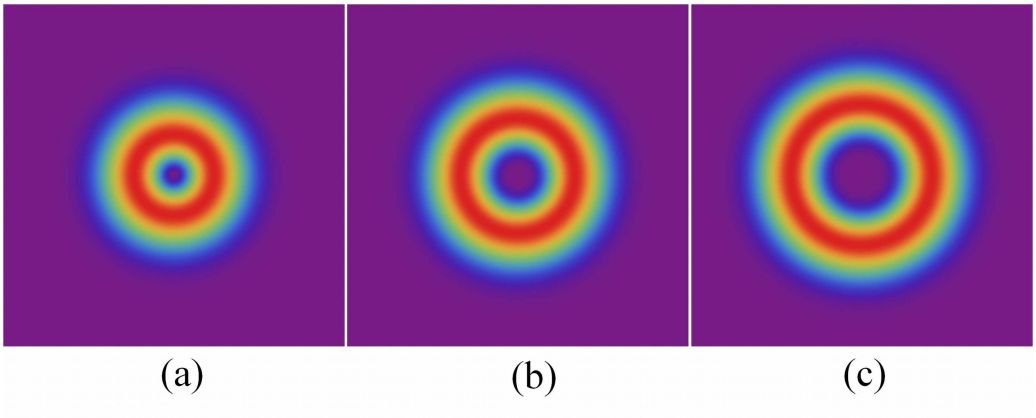

Fig. 3.2 Theoretical images of various orders Laguerre-Gaussian beams: (a) Laguerre-Gaussian beam carrying a topological charge of 1, (b) Laguerre-Gaussian beam carrying a topological charge of 2 and (c) Laguerre-Gaussian beam carrying a topological charge of 3.

There are numerous experimental methods to produce these beams (Arlt *et al.*, 1992; Beijersbergen, 1994; Clifford *et al.*, 1998; Heckenberg *et al.*, 1992; Turnbull *et al.*, 1996). Beijersbergen *et al.* were the first to demonstrate the existence of Laguerre-Gaussian beams by a method known as mode conversion. This method makes use of two cylindrical lenses that are used to define a region in which the Gouy phase of a beam can be manipulated. By enforcing a $\pi/2$ phase shift on a Hermite-Gaussian beam they were able to convert this beam to a Laguerre-Gaussian beam. However there are easier approaches which include the use of diffractive optics, namely phase plates, demonstrated for the first time by (Bazhenov *et al.*, 1990) where a hologram with a screw dislocation was etched onto a plate in order to generate Laguerre-Gaussian beams of azimuthal order ± 1 depending on the left and right handedness of the forked pattern. Other methods include making use of digital holography which is the most cost effective route. In this case by using a spatial light modulator, which is a liquid crystal device that is electronically addressed, the phase of the incoming beam is modulated to produce the desired field. There exist other beams which also carry orbital angular momentum such as higher-Bessel beams, which are the solutions to the Helmholtz equation; due to the fact that they are enveloped by Laguerre-Gaussian beams (Dholakia & McGloin, 2005), also there exist Mathieu beams (Gutierrez-Vega *et al.*, 2000) and Ince-Gaussian beams which are the explicit solution to the wave equation in elliptical cylindrical coordinates and which complete the family of beams that carry orbital angular momentum (Bundres & Gutierrez-Vega, 2004c).

Laguerre-Gaussian beams are useful within optical trapping systems since they cause trapped particles to rotate due to the transfer of orbital angular momentum (Aterson *et al.*, 2001; He *et al.*, 1995). The combination of a higher-order Laguerre-Gaussian beam with a Gaussian beam allows for atoms to be trapped within a magneto optical trap (Snadden *et al.*, 1997). These beams have also been used as toriodal traps for Bose-Einsten condensate (Tempere *et al.*, 2001; Wright *et al.*, 2002) and optical dipole traps (Kuga *et al.*, 1997). They can also write optical wave guides in atomic vapour (Truscott *et al.*, 1999).

3.2 Bessel and Bessel-Like Beams

3.2.1 Bessel Beams

A Gaussian beam as stated previously is well defined and retains its spatial distribution as they propagate. It was also seen that Gaussian beams diffract as they propagate upon reaching a certain distance defined by the Rayleigh range. There exists however a class of beams that are non-diffracting in nature, Bessel beams. They are a solution to the Helmholtz equation (Durnin *et al.*, 1987). Mathematically a Bessel beam is said to exist over an infinite area and carry an infinite amount of power. This holds to be true in theory however this ideal case is not reproducible in the laboratory. In principle we are able to generate a Bessel-Gauss beam where the field is represented as (Gori *et al.*, 1987)

$$E[r,z] = A\frac{w_o}{w(z)}\exp\left[i\left(k-\frac{k_r^2}{2k}\right)z - i\zeta(z)\right]J_0\left(k_r r/(iz/z_R)\right) \times \exp\left[\left(\frac{-1}{w^2(z)}+\frac{ik}{2R(z)}\right)\left(r^2+\frac{k_r^2 z^2}{k^2}\right)\right], \tag{3.2}$$

where A is the amplitude factor, J_0 is the zeroth-order Bessel function while k_r is the radial wave vector and w_0 is the initial beam waist. The remaining parameters $w(z)$, z_R, $R(z)$ and $\zeta(z)$ hold the same definition as for a Gaussian beam. By setting the propagation distance *z* to equal zero, the field is further simplified to a form that is easily recognisable as a Bessel function enveloped by a Gaussian beam

$$E(r,0) = AJ_0(k_r r)\exp\left[-\left(\frac{r}{w_0}\right)^2\right]. \tag{3.3}$$

It is also possible to produce various higher order Bessel beams by merely replacing the starting field by a Laguerre Gaussian field. The field of a higher order Bessel beam is represented by

$$\begin{aligned} E[r,z] = A\frac{w_0}{w(z)}\exp\left[i\left(k - \frac{k_r^2}{2k}\right)z - \zeta(z)\right]J_\ell(k_r r/(iz/z_R))\exp(\pm i\ell\varphi) \\ \times\exp\left[\left(\frac{-1}{w^2(z)} + \frac{ik}{2R(z)}\right)\left(r^2 + \frac{k_r^2 z^2}{k^2}\right)\right], \end{aligned} \tag{3.4}$$

where the order of the topological charge, ℓ ,determines the order of the Bessel beam and the rest of the parameters hold the same definition as explained previously.

The original method for producing these beams introduced by Durnin and colleagues was to use a circular slit to produce an annular ring that was illuminated onto a lens (Durnin *et al.*, 1987),however over the years other methods were demonstrated both internal and external to the laser cavity which include the use of anistropic crystals (Khilo *et al.*, 2001), holography (Vasara *et al.*, 1989; Davidson *et al.*, 1991) and using a conical optical element known as an axicon (Artl & Dholakia, 2000).

Although holography is considered as the most versatile since it is the easiest approach, the use of an axicon is the most efficient since it allows for almost a hundred percent transmission of the incoming light and it eliminates the generation of other orders that would be seen in the case of holography. For this reason experimentalists prefer this method over the rest. From here onwards, producing a Bessel beam by the use of an axicon will be discussed in detail.

An axicon is a conical optical element that transforms any field into a non-diffracting field. When an axicon is illuminated by some arbitrary field, the light rays will propagate along the cone to form a diamond shaped region in which the Bessel field exists. Anywhere within this region the Bessel field will be non-diffracting.

The non-diffracting region of a Bessel beam is defined by $z_{\max}$ and denotes the maximum distance the Bessel field can propagate given by

$$z_{\max} = \frac{k}{k_r} w_0 \approx \frac{w_0}{\theta}, \tag{3.5}$$

where k the wave vector, k_r is the wave vector in the radial direction given by $k \sin\theta$, w_0 is the Gaussian beam waist and θ is the opening angle defined as

$$\theta = (n-1)\gamma, \tag{3.6}$$

where γ is the cone angle of the axicon and n is the refractive index. Since $z_{\max}$ is inversely proportional to the opening angle which is directly proportional to the cone angle of the axicon, it can be concluded that the non-diffracting region is dependent upon the cone angle such that the smaller the cone angle the greater the non-diffracting region. Looking at slices of the non-diffracting region it is clear that the Bessel field will have a maximum radius at $z_{\max}/2$, this radius is defined as

$$r_{\max} = z_{\max} \tan\theta. \tag{3.7}$$

Considering the field entering the axicon, if a Gaussian beam is used as the starting field then the light rays will travel along a cone such that they will interfere and form a region in which exists a zero-order Bessel beam as seen in Fig.3.3.

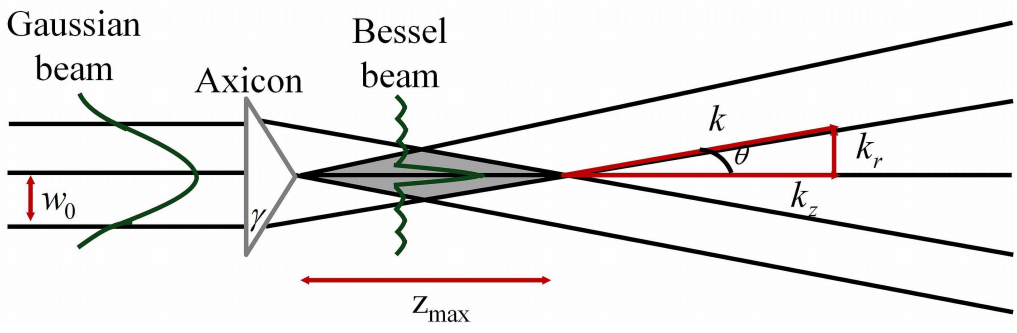

Fig.3.3 Generation of a Bessel-Gauss beam by illuminating an axicon with a Gaussian beam.

Anywhere within this region, z_{max} , the Bessel beam is non-diffracting, however, at the boundary of this non-diffracting region the Bessel field undergoes an abrupt change in spatial transformation from a Bessel field (near-field intensity profile) to a conical field characterised by an annular ring (far-field intensity profile). This is depicted in Fig. 3.4.

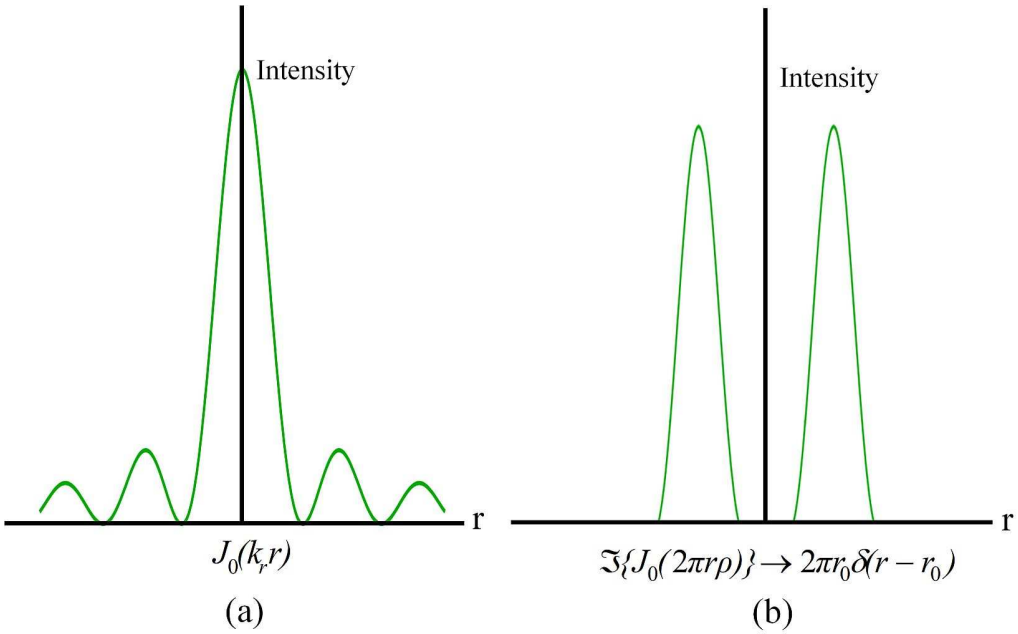

Fig. 3.4 Intensity profile of a zero order Bessel beam: (a) near-field intensity profile where the intensity is greatest at the central position thereafter the intensity decreases moving further away from the central position. (b) far-field intensity profile is an annular ring.

Similar to a zero-order Bessel field, a higher-order Bessel field will also have a conical field in the far-field, however in the near-field, the Bessel field has a central zero-intensity dependent upon the order of the Laguerre-Gaussian beam (see Fig. 3.5.)

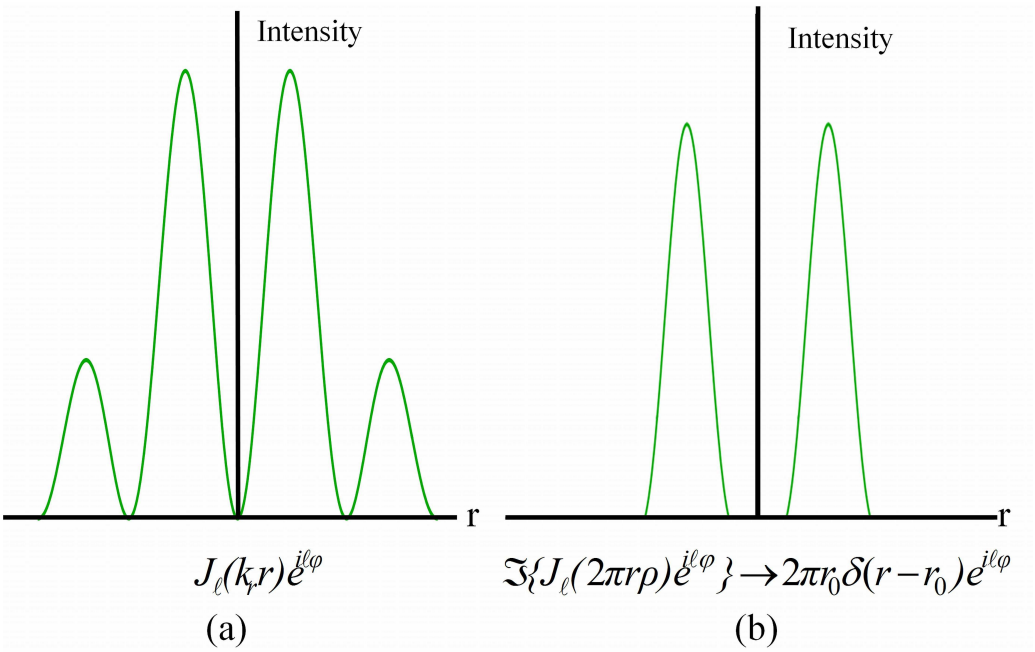

Fig. 3.5 Intensity profile of a higher-order Bessel beam carrying a topological charge of one in the (a) near and (b) far-field.

Bessel beams also hold interesting properties since they are not only non-diffracting, but they are also self-reconstructive, which means these beams have the ability to reconstruct upon encountering an obstruction (Bouchal *et al.*., 1998; Litvin *et al.*, 2009; Sogomonian *et al.*, 1997). Since the light rays travel parallel to the optical axis, placing an obstacle in the path of the beam will cause some of the light to be obstructed by the obstacle, however any of the light rays that are not blocked will reconstruct to form the Bessel beam. A geometric model is used to illustrate the effects of reconstruction of a Bessel beam (see Fig. 3.6).

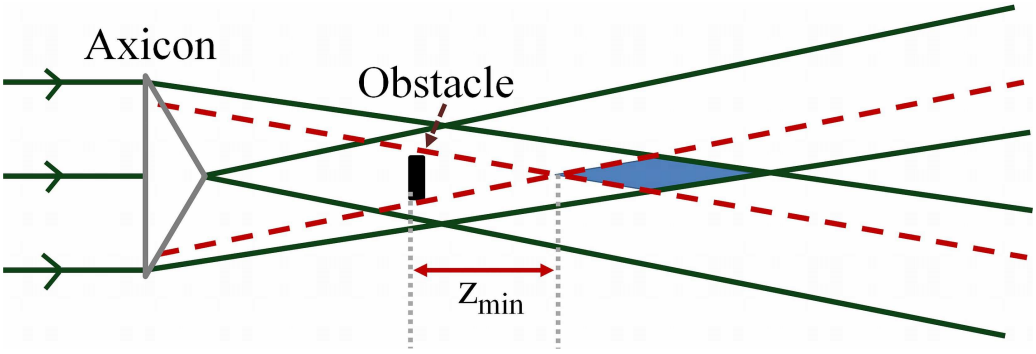

Fig.3.6 Self reconstruction of a Bessel beam upon encountering an obstacle placed within the non-diffracting region.

Since the obstacle will block off some off the light, there exists a shadow region from the obstacle to the point at which the beam will reconstruct. This shadow region is defined by $z_{\min}$ as

$$z_{\min} = \frac{d}{2\tan\theta}. \tag{3.8}$$

As observed in Fig.3.6, the region that is shaded in blue represents the region of reconstruction of the Bessel beam. The only limitation placed on the reconstruction of these beams is that the obstruction has to be placed within the non-diffracting region. The abrupt change in intensity profile from the near to the far field can be considered a major disadvantage to such beams, however we have come up with a way to overcome this problem (section 3.2.2.), and as far as we know this has not been done before.

3.2.2 Bessel-Like Beams

Up until this juncture a single axicon was used to generate various orders of Bessel beams that existed for a finite propagation distance. It has been shown that this limited region of validity of the Bessel beam can be overcome by generating Bessel beams with z-dependent cone angles. These beams are so-named Bessel-like beams and have the advantage of retaining their spatial intensity distribution as they propagate from the near- to the far-field. Many techniques have been considered for the generation of BLBs, including introducing spherical aberrations into an optical system

(Gonchasov *et al.*, 2007; Jaroszewics & Morakes, 1998). The idea here is to form cone–like propagation in order to obtain a uniform on–axis profile. Alternatively these beams are generated using a defocused Galilean-type telescope in order to introduce negative spherical aberrations into the optical system (Aruga, 1997; Aruga *et al.*, 1998) however it was recently shown that it is possible to create such Bessel-like beams using an aberration free method (Belyi *et al.*, 2010) which will be discussed in the remainder of this section. The scheme proposed to produce these Bessel-like beams consists of two axicons and a lens as illustrated in Fig. 3.7.

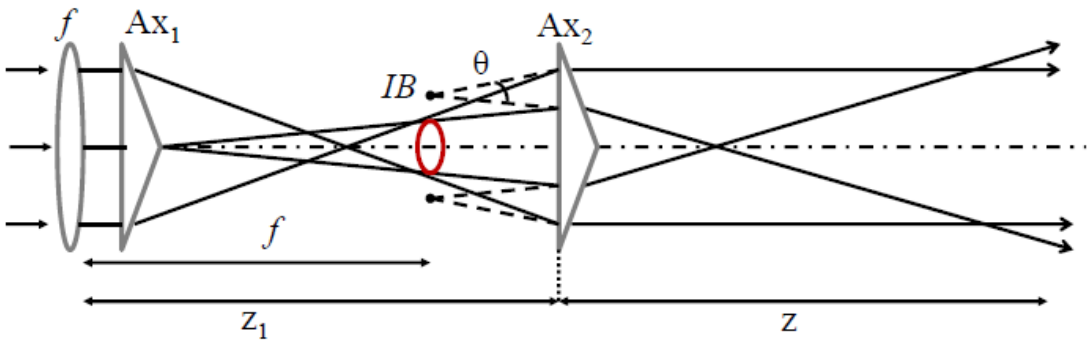

Fig. 3.7 Schematic of optical design to produce z-dependent Bessel-like beams which retain their spatial distribution from the near to the far field.

When a Gaussian beam is passed through the lens and the first axicon an annular ring is produced which is the Fourier transform of the Bessel field produced by the first axicon. This annular ring thereafter illuminates the second axicon such that the Bessel field that is generated exists not only in the near-field, since as it is propagated into the far-field it retains its spatial distribution. The spatial distribution is retained by varying the cone angle as a function of propagation distance such that as $\gamma(z)$ tends to zero the Bessel field will exist in the far-field or as it tends to infinity.

Confirming this idea mathematically, the stationary phase method is implemented in order to deduce firstly that the field entering the second axicon is conical. From the Fresnel integral, the field at the input plane of the second axicon is defined as

$$\mathrm{E}_1(\rho,\mathrm{z}_1) = -\frac{\mathrm{i}}{\lambda \mathrm{z}_1}\exp\left[\frac{\mathrm{i}k_0\rho^2}{2\mathrm{z}_1}\right]\times \int_0^{2\pi}\int_0^{\infty}\exp\left[-\frac{\rho_1^2}{\rho_0^2} - \mathrm{i}k_0\gamma_2\rho_1 - \frac{\mathrm{i}k_0\rho\rho_1}{\mathrm{z}_1}\cos(\varphi-\varphi_1)\right]\rho_1^2\mathrm{d}\rho_1\mathrm{d}\varphi_1, \tag{3.9}$$

where $1/\rho_0^2 = 1/w_0^2 + ik_0/2F - ik_0/2z_1$, w_0 is the beam radius of the Gaussian beam, z_1 is the distance between the two axicons, γ_2 is the cone angle of the second axicon, k_0 is the wave number, ρ is the radius, φ is the angle and F is the focal length of the Fourier lens. Thereafter, applying the stationary phase method to the field yields

$$\mathrm{E}_1(\rho,\mathrm{z}_1) = -\frac{\mathrm{i}\rho\mathrm{F}^2}{(\mathrm{z}_1-\mathrm{F})^2}\left(1-\frac{\gamma_2\mathrm{z}_1}{\rho}\right)^{3/2}\mathrm{x} \exp\left[\frac{\mathrm{i}k_0}{2\mathrm{z}_1}\left(\rho^2 + \frac{\mathrm{z}_1/\mathrm{F}-1+\mathrm{i}\,\mathrm{z}_1/\mathrm{z}_0}{(\mathrm{z}_1/\mathrm{F}-1)^2+(\mathrm{z}_1/\mathrm{z}_0)^2}(\rho-\gamma_2\mathrm{z}_1)^2\right)\right]. \tag{3.10}$$

As calculated above, the field some arbitrary distance z after the second axicon is thereafter determined from

$$\begin{aligned}\mathrm{E}_2(\rho,\mathrm{z}) &= -\frac{\mathrm{i}}{\lambda\mathrm{z}}\int_0^{2\pi}\int_0^{\infty}\mathrm{E}_1\exp\left(\frac{\mathrm{i}k_0\left(\rho^2+\rho_1^2-2\rho\rho_1\cos(\varphi-\varphi_1)\right)}{2\mathrm{z}} - \mathrm{i}k_0\gamma_2\rho_1\right)\rho_1^2\mathrm{d}\rho_1\mathrm{d}\varphi_1 \\ &= \exp\left[\frac{\mathrm{i}k_0\rho^2}{2\mathrm{R}(\mathrm{z})}\right]\left[\mathrm{g}_+(\rho,\mathrm{z})\exp[\mathrm{i}k_0\gamma(\mathrm{z})\rho] - \mathrm{i}\mathrm{g}_-(\rho,\mathrm{z})\exp[\mathrm{i}k_0\gamma(\mathrm{z})\rho]\right],\end{aligned} \tag{3.11}$$

where

$$g_{\pm}(\rho,z) = \frac{f}{2(z+z_1-f)}\sqrt{\gamma_2 - \gamma_1\left(1+\frac{z_1}{z}\right)\pm 1}, \tag{3.12}$$

and the radius of curvature is written as

$$R(z) = z\left[1 + \frac{z}{z_1 - f}\right]. \tag{3.13}$$

We define the cone angle as a function of the propagation distance z as

$$\gamma(z) = \frac{\gamma_2 z_1 + (\gamma_1 - \gamma_2) f}{z_1 + z - f}. \tag{3.14}$$

Using the known asymptotic form of the zero-order Bessel function of the first kind, $J_0 \approx \sqrt{2/\pi z}\cos(z - \pi/4)$, the field after the second axicon is attained as

$$\begin{aligned} E_2(\rho, z) \approx \frac{1}{2}\sqrt{\frac{\pi k_0 \gamma(z)\rho}{2}}\left(g_+(\rho, z) + g_-(\rho, z)\right) \\ \times \exp\left[\frac{ik_0}{2}\left[\frac{\rho^2}{z} + \frac{\rho^2}{R(z)} - \gamma^2(z)R(z)\right]\right] J_0(k_0\gamma(z)\rho). \end{aligned} \tag{3.15}$$

Clearly Eq. (3.14) shows that the cone angle, γ, is dependent upon the longitudinal distance z and it confirms that an increase in z will lead to a decrease in the cone angle. Similarly the above mathematical approach can be carried out for higher-order z-dependent Bessel-like beams (Beyli *et al.*, 2010). These z-dependent Bessel-like beams, just like Bessel beams, also have the ability to self reconstruct; however, since they retain their spatial distribution as they propagate, the position of the obstacle is not limited and can be placed at any point along the propagation axis.

Chapter 4

Optical Trapping and Tweezing

4.1 An Overview

On a daily basis the movement of objects on a macro-scale is observed, a good example would be the forces applied to push and pull a block which results in the movement of the block from one point to the next. The greater question here is, can we achieve this with light? The answer lies in a well known application known as optical trapping and tweezing, discovered over 40 years ago by Authur Ashkin at the Bell laboratories whereby light was used as a tool to manipulate micron sized particles (Ashkin, 1970).

The first stable optical trap was demonstrated in the early 1970s which involved the use of focussing two visible wavelength continuous wave laser beams onto a trapping chamber, containing either of micron sized liquid or gas particles, which was centralised between the two beams as in Fig. 4.1. It was observed that the particles, upon entering the vicinity of the light beams, were accelerated within the chamber in the direction of greatest intensity of light which was due to the forces arising from the radiation pressure of each beam. Furthermore, blocking off one of the beams leads to the trapped particle being dispersed due to Brownian motion.

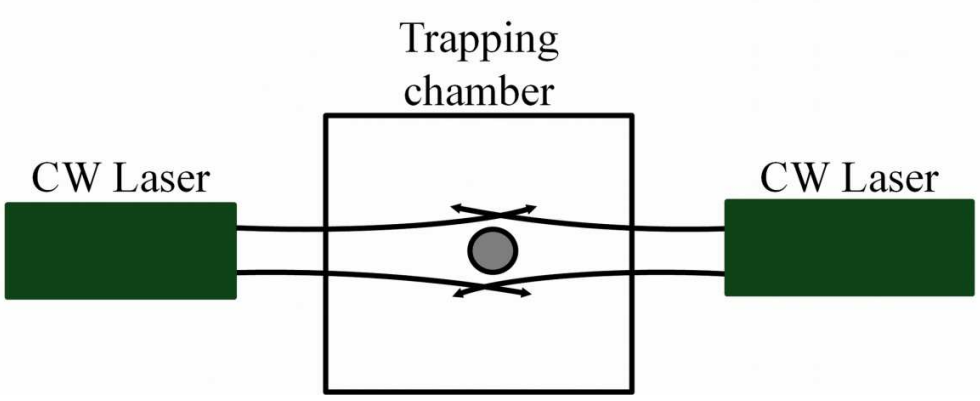

Fig. 4.1 First optical trap demonstrated by Arthur Ashkin, known as the dual beam trap or counter-propagating beam trap.

Approximately 16 years later, Authur Ashkin and colleagues reported the existence of the first single gradient optical trap which was the successor of the counter propagating trap (dual beam trap). Unlike the dual beam trap where the forces of radiation pressure merely accelerated the particles, it was proven that a second component of the radiation pressure existed which acted in the backward direction towards the axial intensity gradient (Ashkin *et al.*, 1986). Since then optical trapping and tweezing has been extensively studied to manipulate micron and recently nano sized particles (Dienerowitz, 2008). With the growing development of the field of holography, optical tweezers over the years has advanced considerably to the extent that it is possible to demonstrate trapping of an array of particles (Mellville *et al.*, 2003; Schonbrun *et al.*, 2005; Woerdemann *et al.*, 2009). Optical trapping is a versatile tool for accurate and precise investigation with respect to Piconewton force measurements. Over the years it has also become a key tool for many applications in the biological field (Abbondazierim *et al.*, 2005; Block *et al.*, 1989; Neuman *et al.*, 2003, Perkins *et al.*, 2004; Shaevitz *et al.*, 2003). There have been an extensive review of the construction and principles of an optical trap (Neuman & Block, 2004; Molley & Padgett, 2003; Smith *et al.*, 1999) which will be discussed in the sections that follow.

4.2 Principle of an Optical Trap

An optical trap is attained by strongly focussing a light beam through an objective lens with a high numerical aperture in order to form a diffraction limited spot. Since light contains photons which carry energy $E = h\nu$ and momentum h/λ, a successful trap is dependent upon the change of linear momentum acting on a particle. As mentioned previously it is the forces due to radiation pressure that determine the magnitude of the trap. The trapped particle is governed by two forces acting upon it, namely the scattering and the gradient force.

The scattering force pushes the particles in the direction of light propagation while the gradient force on the other hand acts in the direction of the intensity gradient. For a stable trap, the gradient force must exceed the scattering force which leads to stable trapping in the axial direction. It is possible to also attain lateral trapping.

In order to describe the forces acting upon the particle, there are three models to consider (which are dependent upon the wavelength of the trapping laser λ and the diameter of the particle a), which arise from the scattering theory of light (Barton & Alexander, 1989; Barton *et al.*, 1989; Gouesbet *et al.*, 1988). For large particles, i.e. $a >> \lambda$, the Mie regime is applicable to determine the respective forces. If the particles are smaller in comparison to the wavelength of the trapping laser, with $a << \lambda$, then the Rayleigh regime should be considered, as illustrated in Fig. 4.2. Both of these regimes will be explained further in the next two sections. There exists a third regime known as a Lorentz-Mie regime where the diameter of the particle is comparable with respect to the wavelength of the trapping laser, note $a \approx \lambda$ (Rohrbach & Stelzer, 2002), however we will not include this regime in our explanation that follows.

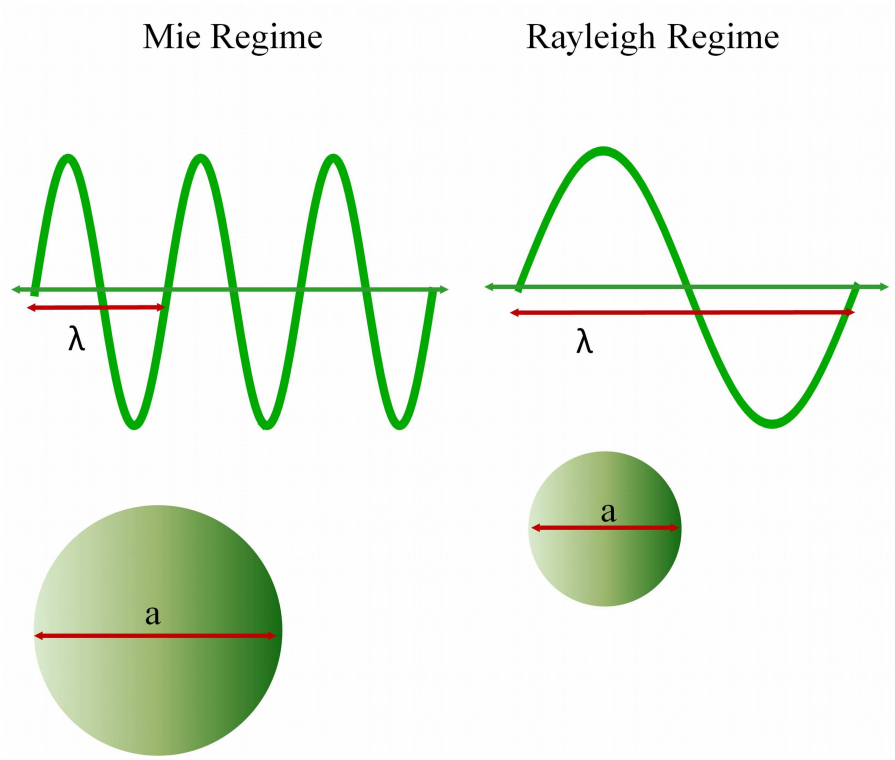

Fig. 4.2 Dependence on particle size and the wavelength of the trapping laser: Mie Regime when the size of the particle is greater than the wavelength of the trapping laser. Rayleigh regime when the size of the particle is less than the wavelength of the trapping laser.

4.2.1 Mie Regime

Within the Mie regime, ray optics is used to describe the forces acting on the particles as illustrated in Fig. 4.3. When the incident light impinges on the particle, it is refracted due to a change in medium, which will cause a change in momentum. According to Newton's third law, an opposite and equal change in momentum acts on the particle. Hence the force that acts upon the particle is equal to the rate of change of momentum which is proportional to the light intensity. As seen in Fig. 4.3(a), if the incident rays are parallel before impinging upon the particles, then the intensity gradient increases from left to right hence the particle will be attracted to the centre of the beam consequently lateral trapping is achieved. On the other hand when the light rays are tightly focused and thereafter impinge upon the particle as in Fig. 4.3(b), then the net force is toward the focus and a stable three dimensional trap is obtained (axial trapping).

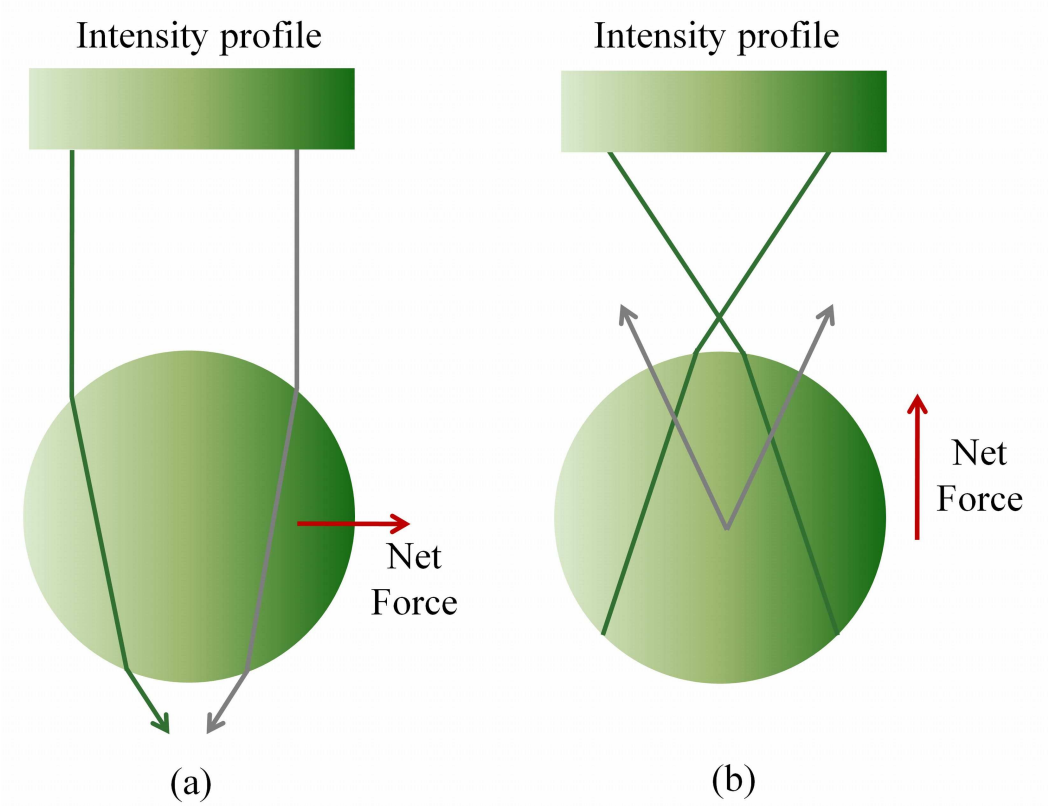

Fig. 4.3 The diagram illustrates the particles behaviour within the Mie regime, (a) when the light rays impinging onto the particle are parallel then the particle is attracted to the centre of the beam (lateral trapping) however (b) when the light is tightly focused before interacting with the particle, the particle is attracted to the focus and a strong axial trap in three dimensions is obtained.

Consider the scattering of a single ray off a particle as seen in Fig. 4.4. If an incident ray P impinges onto the particle, it is refracted and reflected causing a change in momentum.

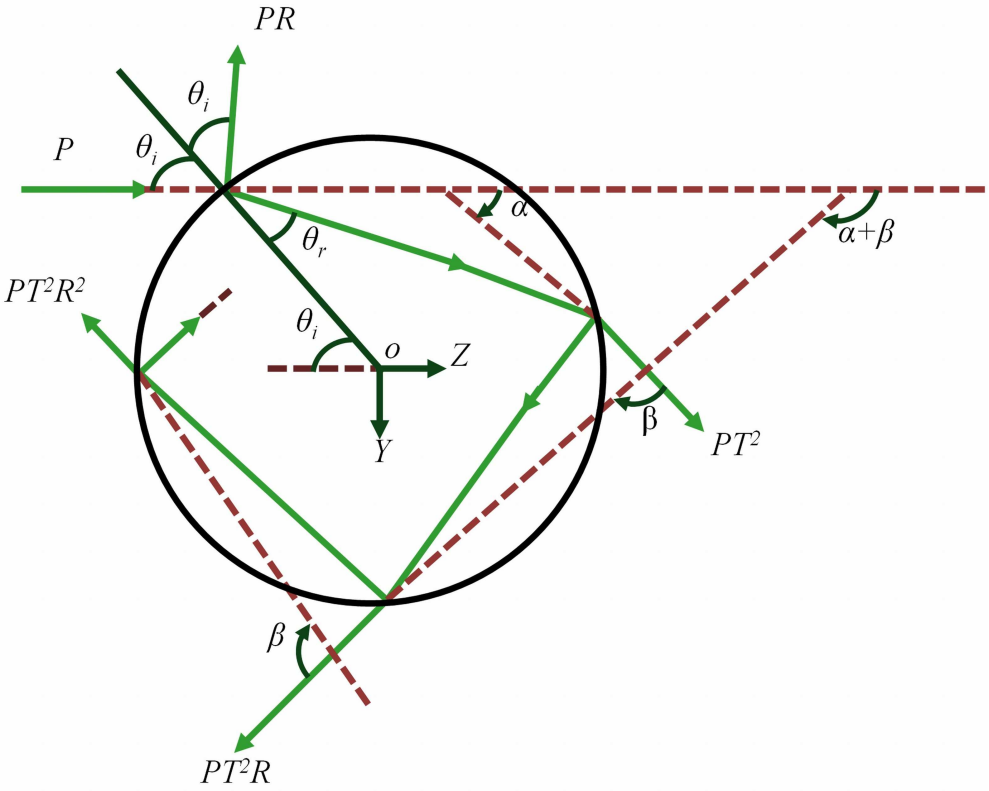

Fig. 4.4 Single ray impinging upon a particle causing a reflection and refraction of rays.

The total force acting on the particle is then the sum of the contributions due to the reflected ray PR and its refractive counterparts $PT^2, PT^2R, PT^2R^2, ..., PT^2R^n$ where R is the Fresnel reflection coefficient and T is the Fresnel transmission coefficient from the surface. From this the net force can be broken up into two components, the scattering force and the gradient force where θ_i is the angle of incidence while θ_r is the angle of reflection (Ashkin, 1992). The two forces respectively are expressed as

$$F_Z = F_{scat} = \frac{n_m P}{c}\left\{1 + R\cos 2\theta - \frac{T^2\left[\sin(2\theta_i - 2\theta_r) + R\sin 2\theta_i\right]}{1 + R^2 + 2R\cos 2\theta_r}\right\}, \tag{4.1}$$

and

$$F_Y = F_{grad} = \frac{n_m P}{c}\left\{R\sin 2\theta - \frac{T^2\left[\sin(2\theta_i - 2\theta_r) + R\sin 2\theta_i\right]}{1 + R^2 + 2R\cos 2\theta_r}\right\}, \tag{4.2}$$

where $\frac{n_m P}{c}$ is the incident momentum per second of which n_m is the refractive index of the medium in which the particle is immersed, c is the speed of light and P is the power. In order to determine the trapping efficiency we consider a dimensionless factor Q that is related to the trapping force as

$$Q = \frac{F_{drag}}{\frac{n_m P}{c}}, \tag{4.3}$$

where $F_{drag} = 6\pi\eta r v$ is Stokes drag and η, r, v are the viscosity of the medium, radius of the particle and velocity of the medium respectively. By varying the dimensionless factors with respect to θ for the scattering, gradient force and for $F_{mag} = \sqrt{F_{scat}^2 + F_{grad}^2}$ as illustrated in Fig. 4.5 we observe that if the incident angle is less than 60^o then the gradient force will exceed the scattering force; furthermore, increasing the angle of incidence leads to the two forces almost cancelling each other out.

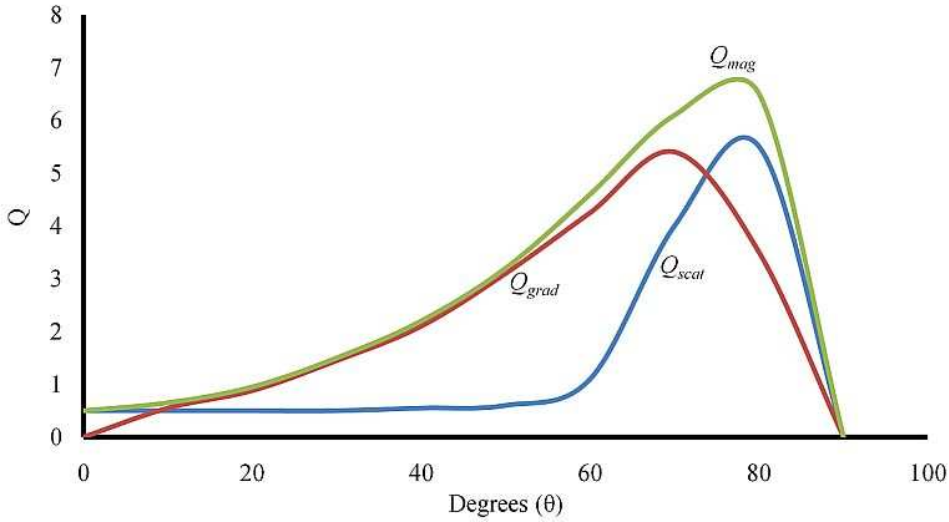

Fig. 4.5 Relation of the dimensionless factors, Q_{scat}, Q_{grad} and Q_{mag} with respect to θ.

4.2.2 Rayleigh Regime

To satisfy the condition for the Rayleigh regime the diameter of the particle must be less than the wavelength of the trapping laser $a << \lambda$. Within this regime the trapped particle acts as an electric dipole being influenced by a spatially varying electric field where the scattering and gradient forces are easily separable. The scattering force is dependent upon the initial intensity of the light beam and is given as

$$F_{scat} = \frac{I_0 \sigma n_m}{c}, \tag{4.4}$$

where c is the speed of light, n_m is the refractive index of the medium, I_0 is the initial intensity and σ is the scattering cross section which is expressed as

$$\sigma = \frac{128\pi^5 r^6}{3\lambda^4}\left(\frac{m^2-1}{m^2+2}\right)^2, \tag{4.5}$$

where λ is the wavelength of the trapping laser, r is the radius of the particle and m is the ratio of the refractive index of the particle to that of the medium. Bear in mind that the value of m must

be greater than one, hence $n_p > n_m$ where n_m is the refractive index of the medium and n_p is the refractive index of the particle.

On the other hand, the gradient force is dependent upon the gradient of the intensity by defined as (Neuman & Block, 2004)

$$F_{grad} = \frac{2\pi\alpha}{cn_m^2}\nabla I_0, \tag{4.6}$$

where α is the polarizability of the particle defined as

$$\alpha = n_m^2 r^3 \left(\frac{m^2 - 1}{m^2 + 2} \right). \tag{4.7}$$

For a strong axial trap in three dimensions the gradient force must exceed the scattering force. Furthermore the direction of the gradient force is dependent upon the refractive index of the particle. When the refractive index of the particle is greater than that of the medium then the force acts in the direction of the intensity gradient however if the refractive index of the particle is less than that of the medium then the force acts in the opposite direction of the intensity gradient and trapping will not be achieved.

4.3 Optical Design Considerations

Constructing a basic Gaussian trap is a simple procedure. Some of the key components include choosing the appropriate laser for the application of the trap, a proper beam expander as well the correct microscope objective lens. It is also vital to decide upon the right imaging and illumination system. A home built optical trapping system can easily be built provided the necessary optical elements are obtained which includes the appropriate laser, mirrors, lenses, a dichroic mirror which is specific to the wavelength of the laser, a microscope objective lens, a stage to hold the sample, a white light source for the illumination and a CCD Camera for viewing the trap as represented in Fig. 4.6. One can obtain a commercial system which is less tedious to set up, however there is a limitation on the applications that can be performed.

With a custom built system there is much more room to re-arrange the trap when the need arises hence the next section deals with a descriptive overview of all the key components mentioned to give an understanding of the correct procedure to build a successful optical trapping system.

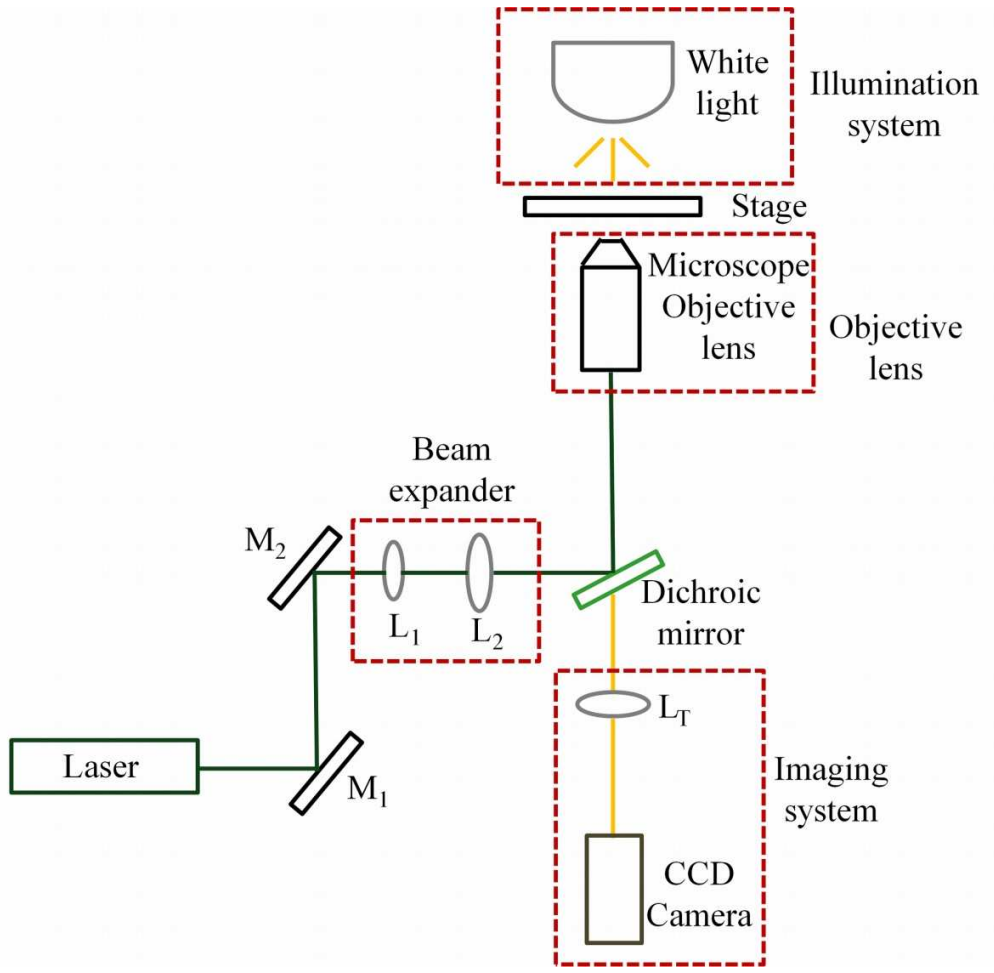

Fig. 4.6 Optical trapping system highlighting the key components required to form a stable trap. M_1 and M_2 are flat mirrors, L_1 and L_2 are lenses used as a beam expander and L_T is the tube lens.

4.3.1 Choice of Laser

The choice of laser is dependent upon a few aspects which include high power output, good pointing stability and low power fluctuations. For this reason mostly continuous wave lasers are chosen with a Gaussian beam. Power fluctuations should be avoided since this would lead to a variation of the trap stiffness. The beam should be well collimated with a high pointing stability since any instability can lead to a displacement of the trap position at the sample plane.

The choice of wavelength is also critical and is dependent upon the type of samples of interest. For biological samples, wavelengths between 750-1100 nm are preferred since there is a minimal absorption of heat at this range, hence the sample will not be destroyed. When considering silica beads, the choice of wavelength is not a severe problem since damage due to absorption is not an issue, although over heating of the medium should be avoided.

4.3.2 Microscope Objective Lens

The microscope objective lens is the key component within the trapping system. It is important to choose an objective lens with a high numerical aperture with a value between 1 to 1.3 in order to attain a tightly focused beam. A standard objective lens can either be finite or infinitely corrected.

For a finite corrected objective lens the sample is imaged a set distance behind the back aperture of the lens onto the camera or detector. With an infinitely corrected objective lens, which is commonly used in most systems, a tube lens is needed to image the sample onto the camera or detector. Generally in most optical trapping systems the objective lens plays a dual role since the same objective lens that is used to attain a diffractive limited spot is also used for the imaging of the specimen plane. This is further illustrated in Fig. 4.7. Even though an objective lens consists of a compound of lenses for simplicity a single lens is illustrated.

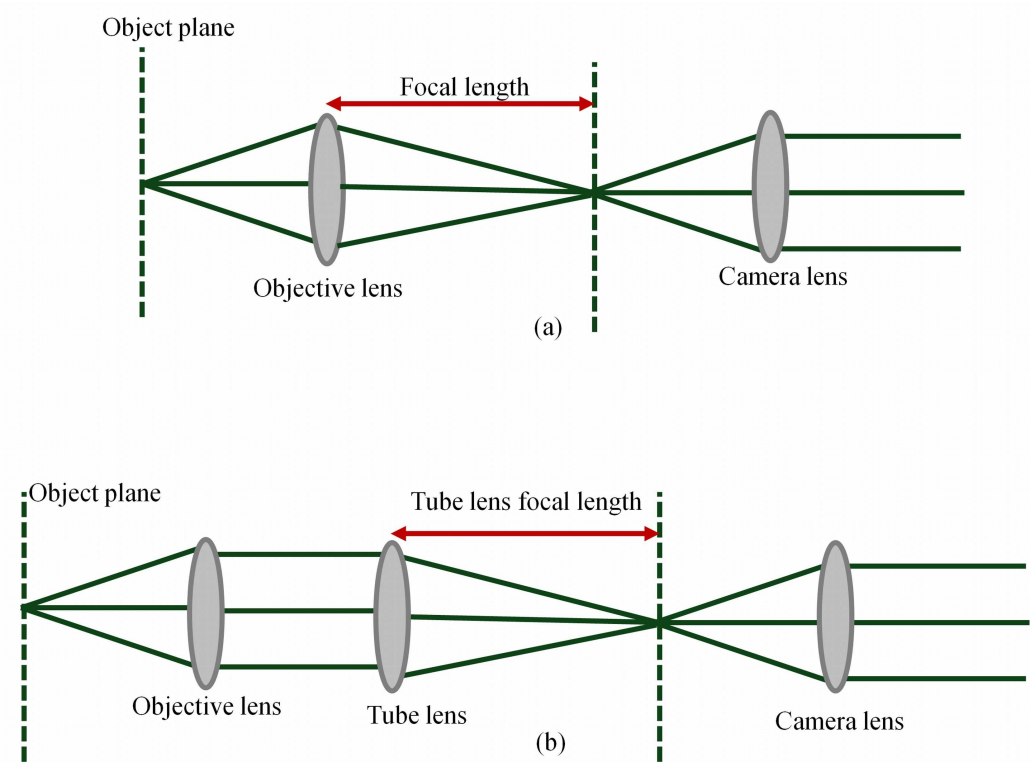

Fig. 4.7. Image illustrating the path that the light ray goes through when passing through an objective lens, (a) a finitely corrected objective lens and (b) an infinitely corrected objective lens.

An objective lens with a high numerical aperture is recommended to attain a strong optical trap. It also is important with respect to the resolution power of the specimen being trapped and imaged. An objective lens with a high numerical aperture collects more light in order to form a brighter image at the image plane. The numerical aperture is defined as

$$NA = n_m \sin\theta, \tag{4.8}$$

where n_m is the refractive index of the medium between the front face of the objective lens to the front of the cover slip of the microscope slide and θ is the half angle of the angular aperture of the lens. The refractive index plays a vital role in attaining a high numerical aperture and for this reason oil immersion objective lenses are the most likely choice since the oil immersion compensates for the low refractive index of the distilled water medium.

4.3.3 Beam Expander

In order to attain an efficient trap the beam diameter has to be of the order of the diameter of the back aperture of the objective lens. If there is an under fill of the objective lens, there would be a decrease in intensity gradient that would lead to a weaker trap. Slightly overfilling the objective lens leads to a tightly focused beam, although care should be taken not to over fill the objective lens as this would lead to heating.

4.3.4 Köhler Illumination

Köhler Illumination was first introduced in 1893, by August Köhler, in order to improve the field of microscopy. He proposed that using the optical design outlined in Fig. 4.8 (which consists of a white light source, a collector and condenser lens respectively, field and aperture diaphragm) would yield an evenly illuminated specimen. The advantage of such a system is that the illumination and the region of interest can be controlled independently. This is achieved by either varying the field diaphragm which is responsible for controlling the region of interest or adjusting the aperture diaphragm which is responsible for adjusting the illumination of the sample.

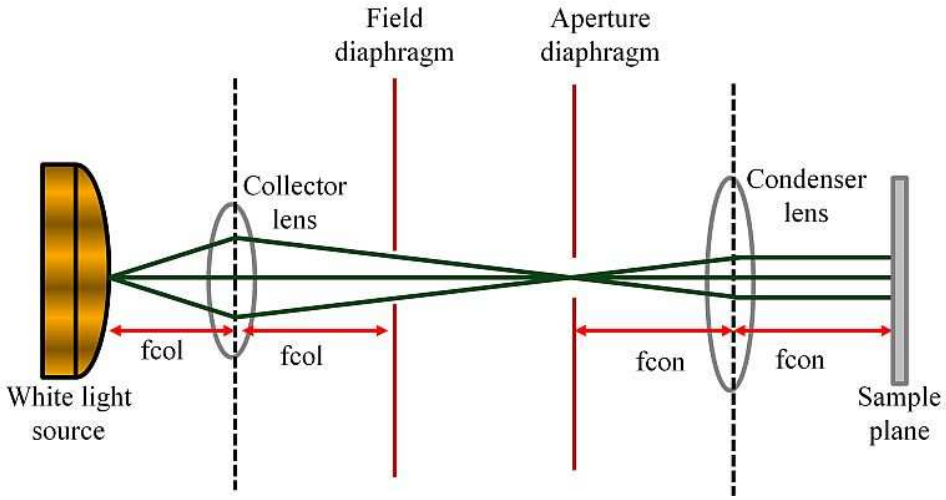

Fig. 4.8 An optical design proposed to obtain an evenly illuminated sample where fcol is the focal length of the collector lens and fcon is the focal length of the condenser lens.

To understand the concept of Köhler illumination the optical design illustrated in Fig. 4.8 can be broken up into two parts. The first part deals with the light source which is coupled to the collector

lens used to re-image the light source to the back focal plane of the condenser lens. At the start the position of the white light source is determined hence the position of the aperture diaphragm gives an indication of the magnification of the white light source. At this point it is important to bear in mind that the light source should cover the entire diameter of the aperture diaphragm. It is also observed that the field diaphragm is uniformly illuminated.

The second part to setting up a Köhler illumination system is the addition of a condenser lens. The primary purpose of this lens is to image the field obtained at the field aperture to the sample plane. By adjusting the position of this lens the sharpness of the sample can be adjusted.

To visualise the concept of Köhler illumination, refer to Fig. 4.9 of an arbitrary specimen. In frame Fig. 4.9(a) notice the sample is unevenly illuminated judging by the dark region on the top end of the sample. By closing the field diaphragm the region of interest is varied as in Fig. 4.9(b). Thereafter adjusting the height of the condenser lens increases the sharpness of the specimen, observed in frame Fig. 4.9(c). Frame Fig. 4.9(d) is basically illustrating the repositioning of the camera such that the specimen being imaged is centred. Finally in frame Fig. 4.9(e), the field diaphragm is opened once again and an evenly illuminated specimen is obtained.

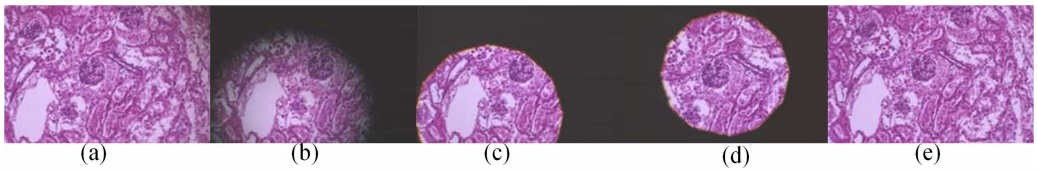

Fig. 4.9 Images illustrating the steps performed to obtain an evenly illuminated sample (Davidson & Feller, 2000).

Furthermore applying this to an optical trapping system improves the quality of the imaging shown in Fig. 4.10 whereby the sample being imaged consists of silica beads 4 μm in diameter in distilled water. It is conclusive that there is an improvement in the quality of the imaged sample with Köhler illumination.

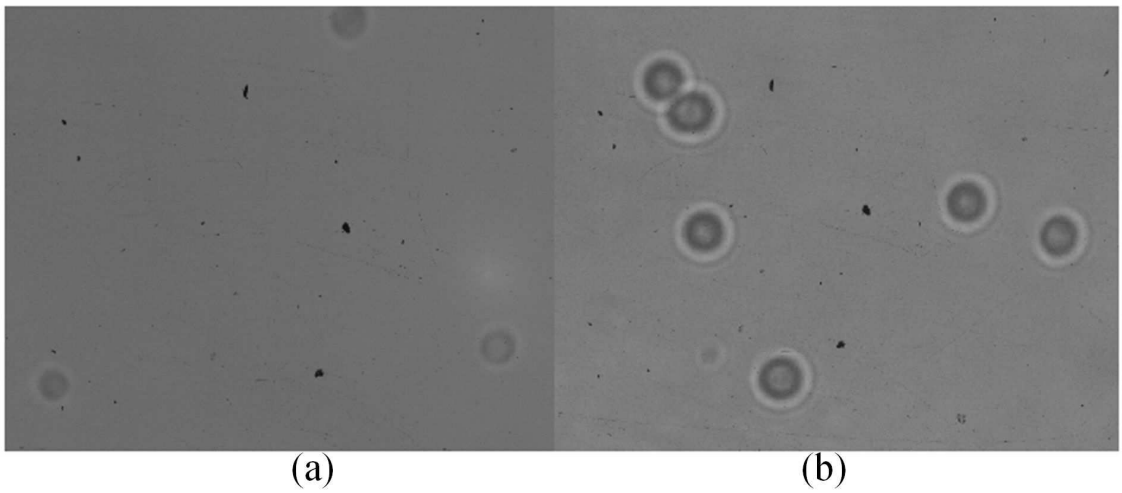

Fig. 4.10 Images illustrating the effects of Köhler illumination on a sample: (a) An image of the sample prior to Köhler illumination and (b) the sample after Köhler illumination.

4.4. Calibrating an Optical Trap

Calibrating an optical trap gives an indication of the efficiency of the trap which can be useful information when dealing with specific applications. There are many methods that can be used to calibrate an optical trap (Neuman & Block, 2004). Here the viscous drag force, equipartition and the power spectrum method will be discussed in order to understand the effects the trapping power has on the strength of the trap.

As previously mentioned we have chosen a video based detection method to view our trap, hence for the calibration methods, it is preferable to either use a CCD (Charged couple device) camera or recently introduced smart camera (Complementary metal oxide semiconductor) CMOS technology. Both of these devices have their own advantages and disadvantages, and it comes down to which sensor best suits the practical application.

There is an ongoing debate as to which of the two technologies is superior. CCD cameras have been around since the early seventies. The advantage of using a CCD would be that it has a lower noise, higher sensitivity and image quality; however they consume a lot more power and dissipate a lot more heat. They are larger in comparison to CMOS cameras and are not able to cope with frame rates greater that 15frames/sec.

CMOS imagers have their disadvantages in that they suffer from a satisfactory amount noise and they have a lower image quality in comparison to a CCD camera however they do consume less power, they cost less, they are smaller in dimensions and they can cope with high speed imaging (Biggs *et al.*, 2006). It is for this reasoning that when dealing with the tracking of particles for the calibration of an optical trap, CMOS cameras are preferred.

There are other choices of detection namely using a quadrant photo detector (QPD) which is a non-video based method. A QPD consists of four silicon based photodiodes. This method offers high sensitivity as well as low noise output and has found its place in the field of optics for highly sensitive force measurements of micro and nano particles.

4.4.1 Viscous Drag Force Method

This is the most direct method of calibrating the force acting on a trapped particle. It makes use of the viscous drag used to dislodge a particle from its equilibrium position in order to determine the strength of the trap. Since we are dealing with micron sized particles the inertial forces are quite small and hence negligible. As a result the drag force is determined from

$$F_{drag} = \beta v, \tag{4.9}$$

where β is the drag coefficient and v is the velocity of the bead. From Stokes' Law it is known that the drag coefficient acting on a particle with a radius of r is given by $\beta = 6\pi\eta r$. When the particle just about releases from the trap the drag force acting on the particle is considered to be equal to the optical trapping force

$$F_{drag} = F_{trap}. \tag{4.10}$$

4.4.2 Equipartition Method

A trapped particle may displace within an optical trap due to the influence of thermal fluctuation of the medium that it is immersed in. This displacement of the particle from its equilibrium position is measured and thereafter the trap stiffness κ can be determined from the equipartition equation expressed as

$$\frac{1}{2}k_B T = \frac{1}{2}\kappa\langle x^2\rangle, \tag{4.11}$$

where T is the temperature, k_B is the Boltzmann constant ($1.3806503\times10^{-23} JK^{-1}$)and $\langle x^2\rangle$ is the mean variation of the particle from its equilibrium position. Since the particle displaces from its equilibrium it acts like a harmonic oscillator, obeying Hooke's law, which means that there is a restoring force that acts on the particle to return it to its trapped position:

$$F_{trap} = -\kappa x, \tag{4.12}$$

where κ is the trap stiffness determined from the equipartition equation and x is the displacement of the particle. This method has its advantages since the measurement is independent on the viscosity of the fluid or the geometry of the particle.

4.4.3 Power Spectrum Method

Once trapped, a particle will displace within the trap as mentioned in the previous section, from which the Brownian motion of the particle can be exploited to determine the trap stiffness. The power spectrum method makes use of this thermal fluctuation as given by Eq. (4.13) which describes a Lorentzian

$$S(f) = \frac{k_B T}{\pi^2 \beta (f_c^2 + f^2)}, \tag{4.13}$$

where T is the temperature, k_B is the Boltzmann constant and f_c is the corner frequency. This power spectrum can be fit with a corner frequency, from which the trap stiffness can be calculated as

$$f_c = \frac{\kappa}{12\pi^2 a^2 \eta}, \tag{4.14}$$

where f_c is the corner, η is the viscosity of the medium and κ is the trap stiffness. Using the power spectrum method to determine the trap stiffness requires a detector system with an adequate bandwidth to record the power spectrum well beyond the corner frequency. Experimentally the power spectrum is attained by a Fourier transformation of the data obtained from the displacement over a period of time from the time to the frequency domain. An example of a power spectrum is shown in Fig. 4.11.

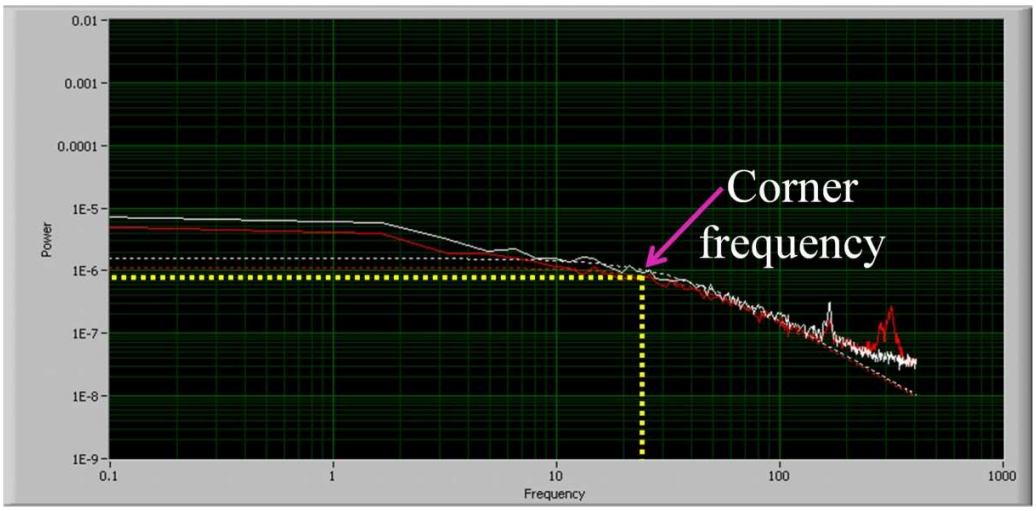

Fig. 4.11 The power spectrum plot illustrating the Brownian motion of a trapped particle.

From the power the corner frequency (roll off frequency) can be extracted which is the frequency at which the particle escapes the trap denoted by the yellow dotted line (refer to Fig. 4.11). At frequencies below the corner frequency ($f < f_c$) the particle is said to be trapped however when the frequency is greater than the corner frequency ($f > f_c$), the particle is said to be free (Gibson et al., 2008; Berg-Sorensen & Flyvberg, 2004).

As previously mentioned it is the displacement of the particle that is used to determine the trap stiffness. This displacement is obtained by tracking the particle using an appropriate tracking algorithm. There are many algorithms that can be used for the tracking which include the centre of mass (Ghosh *et al.*, 1994; Lee *et al.*, 1991) and cross correlation (Gelles *et al.*, 1988; Kusumi *et al.*, 1993). The different types of algorithm can be classified into two types. The first type of algorithm

estimates the absolute position of the particle in each frame independently. An example of this type of algorithm would be the centre of mass. Alternatively the algorithm will determine the position of the particle in one frame with respect to subsequent frame, which is how the cross correlation algorithm works.

For the centre of mass method one would have to measure the distance a particle has moved, the centre of mass is calculated and subtracted from the centre of mass of a subsequent frame. The centre of mass is determined from

$$C_x = \frac{\sum_{i=1}^{n}\sum_{j=1}^{m}(x_i.I_{ij})}{\sum_{i=1}^{n}\sum_{j=1}^{m}I_{ij}}, \tag{4.15}$$

where x_i is the coordinate of the pixel in the x-direction and I_{ij} is the intensity of that pixel. This method makes an assumption that the intensity of the pixel is greater than that of the background. It is therefore vital to narrow the region of interest so that as much of the background can be excluded. Although this approach is valid for particles that are symmetric and asymmetric, it is very susceptible to a change in particle shape and orientation from one frame to the next.

The cross correlation method on the other hand compares the position of a particle, *I*, in one frame to the position of the particle in successive frames. Let the position of the particle in the successive frames be *K*. If *K* which represents the particle being tracked is shifted relative to *I* in increments of one pixel then for each increment a correlation value is determined that describes how well the values of *K* and *I* are alike. This is done by finding the correlation between *K* and *I* from

$$X_{x,y} = \sum_{i=0}^{n}\sum_{j=0}^{m} I_{x+i,\,j+y}(K_{ij}), \tag{4.16}$$

where *x* and *y* describe the distance that *K* has moved over the original position *I*.

Chapter 5

Experimental Generation of Novel Beams for Optical Trapping

5.1 Observation of Various Order Laguerre Gaussian Beams

As previously discussed, there are many ways to generate Laguerre-Gaussian beams. Phase plates are well known for this purpose (Bazhenov *et al.*, 1990) however they are structure dependent hence most people tend to use a Spatial Light Modulator (SLM) since they are versatile. An SLM is a liquid crystal device as illustrated in Fig. 5.1 that is electronically addressed to modulate the phase of the incoming beam appropriately in order to generate the desired output beam. This is achieved by programming a grey scale phase pattern onto the screen of the SLM. It is important for an SLM to be calibrated prior to being used in any application (See Appendix A).

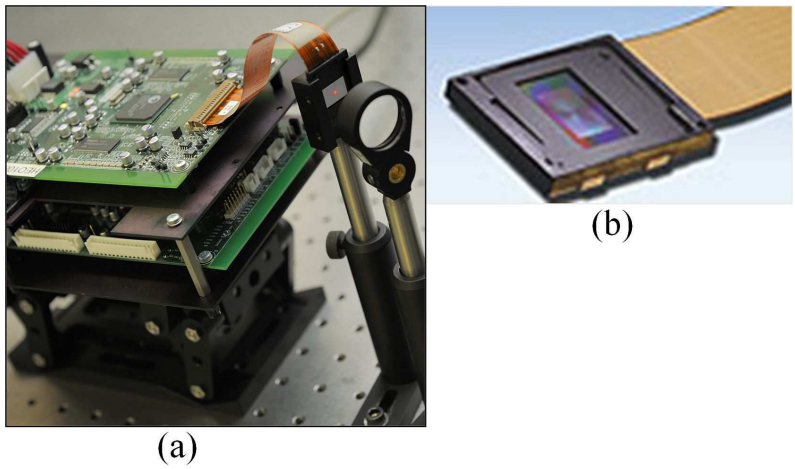

Fig. 5.1 Image of an SLM (a) and (b) is a zoomed in image of the liquid crystal display which has a pixel dimension of 1920 by 1080.

One can build a basic optical system to create these beams where the most vital component is the SLM as seen in Fig. 5.2. A Gaussian beam, Fig. 5.2(a), was directed onto a spatial light modulator (Holoeye PLUTO VIS) with the appropriate grey scale phase pattern, Fig. 5.2(b). The phase of the beam was modulated accordingly and a Laguerre-Gaussian beam, Fig. 5.2(c), was generated which is passed through a lens of focal length 100 mm which was thereafter magnified by a 10x objective lens and detected by a Scorpion IEEE 1394 CCD Camera (model SCOR-20S0). We were able to experimentally generate various order Laguerre-Gaussian beams by varying the grey scale phase pattern that was electronically addressed to the spatial light modulator as illustrated in Fig. 5.3

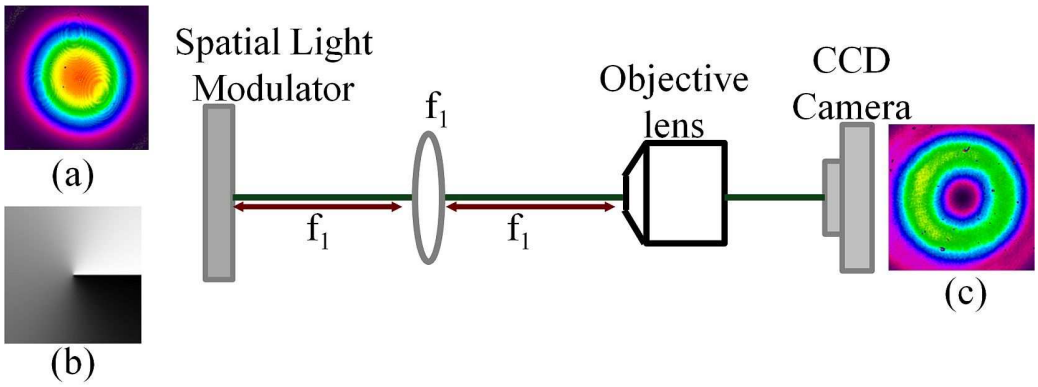

Fig. 5.2 Optical system to generate various order Laguerre-Gaussian beams where (a) is a Gaussian beam, (b) is the greyscale phase pattern and (c) is the corresponding Laguerre-Gaussian beam being generated, where f is an imaging lens with a focal length of 100 mm.

.

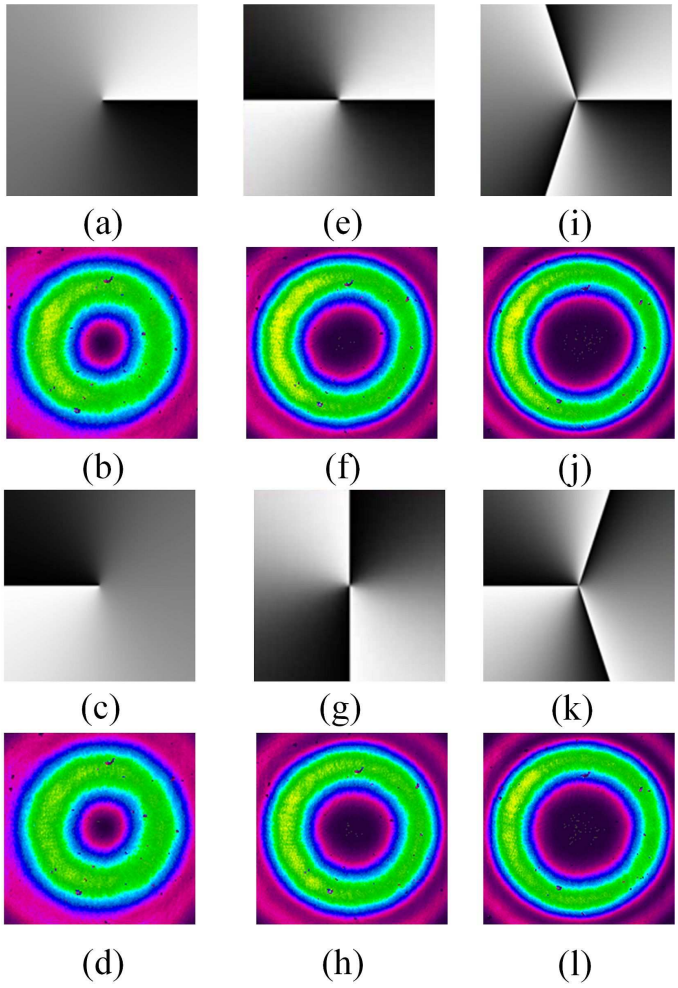

Fig. 5.3 Experimental images of the generation of various order Laguerre-Gaussian beams using a SLM where (a) is the greyscale phase pattern with a topological charge of one, (b) is the corresponding Laguerre-Gaussian beam, (c) and (d) are the greyscale phase pattern and corresponding Laguerre-Gaussian beam respectively except the polarity of the beam changed to negative one. Similarly (e) is the greyscale phase pattern carrying a topological charge of two and (f) is the corresponding Laguerre-Gaussian beam. The same is true for (g) and (h) except there is a change in polarity from positive two to negative two. (i) is the greyscale phase pattern carrying a topological charge of three and (j) is the corresponding Laguerre-Gaussian beam. (k) and (l) are the greyscale phase pattern and corresponding Laguerre-Gaussian beam respectively except the polarity of the beam is changed to negative three.

In order to generate a Laguerre-Gaussian beam carrying a topological charge of one we had to vary the phase of the initial beam from 0 to 2π once which is attained by the grey scale phase pattern as seen in Fig. 5.3(a) where the white region represents a zero phase hence at this point the phase of the beam will remain unchanged while the black region represents a phase of 2π. The Laguerre-Gaussian beam that is generated for this particular grey scale phase pattern is shown in Fig. 5.3(b) where the dark central region is indicative of a zero intensity of the beam. Producing a Laguerre-Gaussian beam carrying a topological charge of negative one is attained in a similar manner except the direction in which the phase varies is reversed as shown in Fig. 5.3 (c) and the corresponding Laguerre-Gaussian beam is seen in Fig. 5.3(d). As in the case of a Laguerre-Gaussian beam carrying a topological charge of two as shown in Fig. 5.3(f), the phase of the beam was varied from 0 to 2π twice which means that the grey scale phase pattern was modulated from white to black twice as seen in Fig. 5.3(e) and furthermore an increase in the topological charge leads to an increase in the region of zero intensity. The same can be said for a Laguerre-Gaussian beam carrying a topological charge of negative two as seen in Fig. 5.3(h) except the grey scale phase pattern varies in phase in the opposite direction as shown in Fig. 5.3(g). Producing higher-order Laguerre-Gaussian beams will follow the same trend as seen in Fig. 5.3(i) to Fig. 5.3(l).

To understand how these beams differ from a Gaussian beam, we look at the way the beam of light travels along the optical axis. In the case of a Gaussian beam, the light rays propagate parallel to the optical axis however for a Laguerre-Gaussian beam the light rays are twisted along the axis as observed previously in Fig. 3.1. This twisting along the optical axis causes the light rays to cancel out at the axis which gives rise to the central zero intensity. The region of central zero intensity is influenced by the order of the topological charge hence an increase in the topological charge leads to an increase in the number of times the light twists along the optical axis. This means there would be an increase in the region of zero intensity since there is an increase in the number of times the light cancels out. This is further highlighted in Fig. 5.4 which illustrates the influence that the topological charge has on the number of twists of the beam.

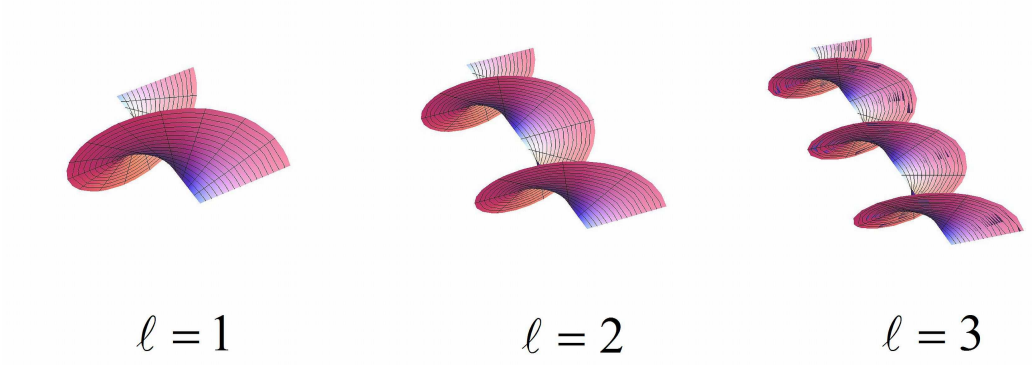

Fig. 5.4 An increase in the order of the topological charge leads to an increase in the number of spirals of the beam and an increase in the region of zero intensity.

The region of zero intensity was determined as represented in Table 5.1 for each of the Laguerre-Gaussian beams mentioned. We see that for a Laguerre-Gaussian beam carrying a topological charge of one the region of zero intensity is approximately 0.554 mm while for a beam with a topological charge of three, this region is approximately 1.795 mm. Overall experimentally we showed that an increase in the order of the beams leads to an increase in the region of zero intensity which was expected since this region is influenced by the order of the topological charge. The polarity of the charge in this case is insignificant since both positive and negative topological charges adhere to the same form. A significant property of these beams is that they carry orbital angular momentum. This is not easily seen however it can be observed by placing these beams into an optical trapping system which brings about the rotation of a trapped particle. This will be discussed further into the experimental analysis (section 6.3).

Table 5.1 Region of zero intensity for the various Laguerre Gaussian beams

Order of Laguerre Gaussian beam (LG_{ℓ}^{p})	Region of zero intensity (mm)
LG_{1}^{0}	0.55
LG_{2}^{0}	1.32
LG_{3}^{0}	1.80
LG_{-1}^{0}	0.56
LG_{-2}^{0}	1.31
LG_{-3}^{0}	1.79

5.2 Realisation of Zero- and Higher-Order Bessel Beams

A Bessel-Gauss beam is easily reproducible using an axicon. The most vital issue that is encountered is the alignment of the axicon itself. If the beam passing through the axicon is misaligned then this will lead to aberrations and should be avoided at all costs. Since it is known that the Bessel field exists for a finite distance only after which the field transforms into a conical field, it is important from the start to be aware of the restriction that is placed upon the system. The cone angle of an axicon is fixed hence in order to vary the region in which the Bessel field exists; the beam waist has to be varied using an appropriate beam expander. Fig. 5.5 illustrates a schematic of the optical setup used to demonstrate the generation of a Bessel-Gauss beam.

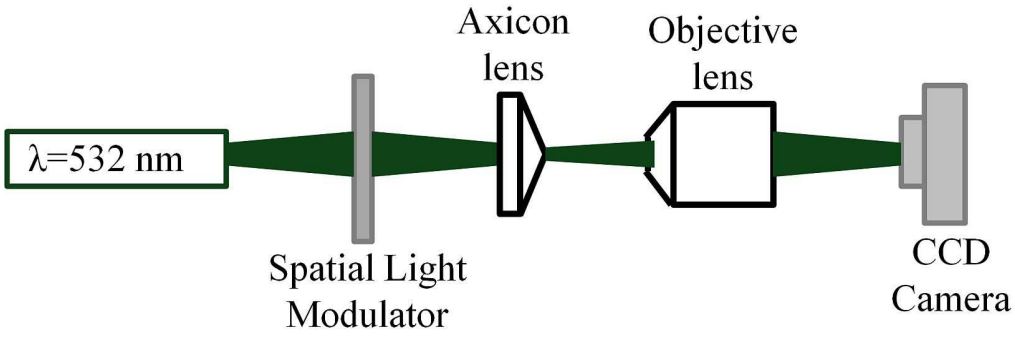

Fig. 5.5 Experimental setup used to generate a Bessel beam using a single axicon and a spatial light modulator to control the field that is passed through the system.

A 532 nm green frequency doubled Nd:YAG laser (model MG-532C-2000) was used with a Gaussian mode which was directed by a few mirrors onto a spatial light modulator in order to vary the beam entering the axicon by varying the phase of the initial beam. The axicon that was used had an opening angle of 5^{o}. The beam was magnified by the objective lens and imaged on a Scorpion IEEE 1394 CCD Camera (model SCOR-20S0). Firstly by projecting a uniform grey scale phase pattern onto the screen of the SLM, a Gaussian beam was allowed to pass through the system in order to generate a zero-order Bessel beam in the near field and thereafter taking the Fourier transform of the Bessel field by placing a lens of focal length 50 mm after the axicon in the system as illustrated in Fig. 5.6, a far-field image of the Bessel beam was obtained which was an annular ring. As expected the near-field intensity profile of a Bessel beam has a bright central spot surrounded by concentric rings. The far-field intensity profile is an annular ring. By changing the phase pattern on the SLM so that the phase is modulated from 0 to 2π once, a first order LG beam can be passed through the axicon which in turn produced a high-order Bessel beam carrying a topological charge of one as illustrated in Fig. 5.7(a). Similar to the Laguerre-Gaussian beam, these beams have a central zero intensity depicted by the dark spot in the centre of the beam followed by concentric rings. Yet again the far-field intensity pattern is an annular ring as seen in Fig. 5.7(b).

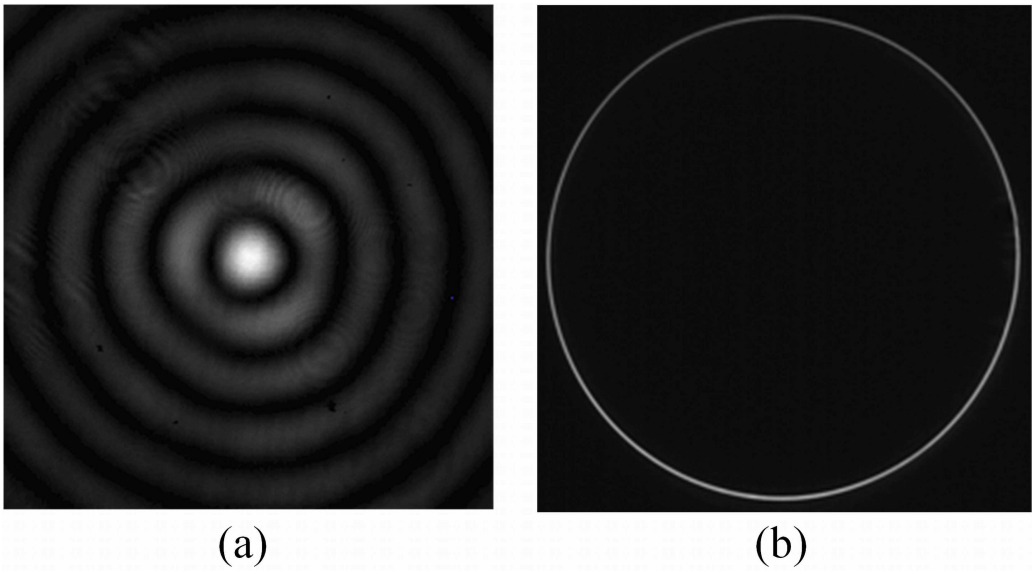

Fig. 5.6 Intensity profile of a zero-order Bessel beam carrying a topological charge of one in near- (a) and far-field (b).

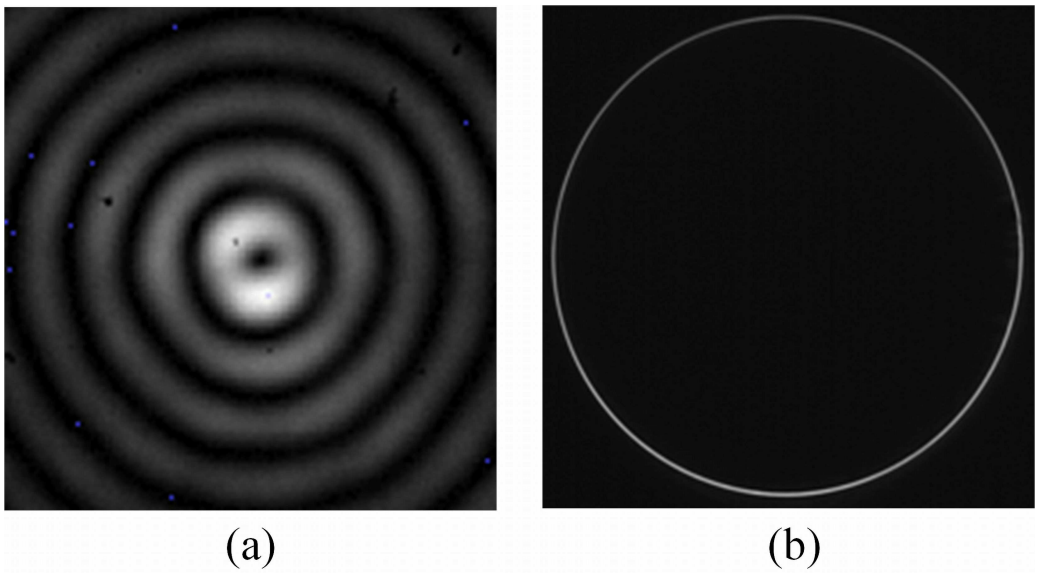

Fig. 5.7 Intensity profile of a higher-order Bessel beam carrying a topological charge of one in near- (a) and far-field (b).

This was carried out for various orders of Laguerre-Gaussian beams which are summarised in Fig. 5.8. As previously mentioned, a higher-order Bessel beam carrying a charge of one is generated by a Laguerre-Gaussian beam of order one. By varying the phase from 0 to 2π once depicted by a change in the gray scale phase pattern going from white to black as in Fig. 5.8(a). The near- and far-field intensity patterns are shown in Fig. 5.8(c) and Fig. 5.8(d) respectively for a Bessel beam of order one. Comparing a higher-order Bessel beam carrying a topological charge of three as in Fig. 5.8(k) to that carrying a charge one, it is noticeable firstly that the phase patterns used to generate the Laguerre-Gaussian beam has changed. For a Bessel beam carrying a topological charge of three the phase pattern varies from 0 to 2π thrice as seen in Fig. 5.8(i) which is seen by the phase pattern varying from white to black three times. This leads to the Laguerre-Gaussian beam having a greater region of zero intensity as in Fig. 5.8(j) and this is further seen in the Bessel beam where by the central dark region of the Bessel beam has also increased as shown in Fig. 5.8(k). The far-field intensity profile however remains the same.

Thus far, the generation of zero and higher order Bessel beams were discussed. We have mentioned that a Bessel field can only exist for a finite distance within its non-diffracting regions after which it undergoes a spatial transformation into an annular ring. This is a major disadvantage to such beams and up until recently there was no way around this problem. We have come up with an improved optical scheme that overcomes this disadvantage by using a double axicon and lens system which will be discussed in the next section.

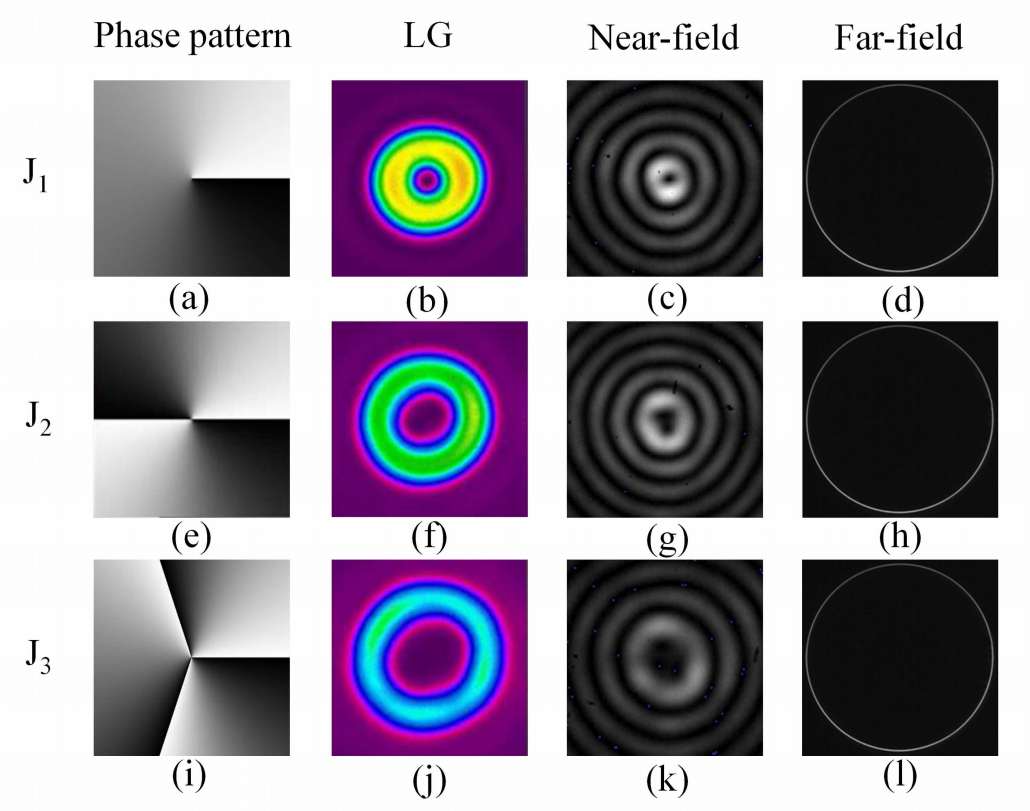

Fig. 5.8 Experimental images of the generation of Bessel beams using a single axicon where (a) is the greyscale phase pattern of order one, (b) is the corresponding Laguerre-Gaussian beam, (c) is the higher-order Bessel beam of order one in the near-field and (d) is the far-field intensity profile of the field which is an annular ring. Similarly (e) is the greyscale phase pattern of order two, (f) is the Laguerre-Gaussian beam of order two, (g) is the corresponding higher-order Bessel beam in the near-field and (h) is the far-field intensity profile which is an annular ring. Yet again (i) is the greyscale phase pattern of order three, (j) is the corresponding Laguerre-Gaussian beam, (k) is the higher-order Bessel beam of order one in the near-field and (l) is the far-field intensity profile of the field which is an annular ring.

5.3 Realisation of Bessel-Like Beams

In order to incorporate the scheme in Fig. 3.7 into an experimental setup, a frequency doubled Nd:YAG laser (model MG-532C-2000, $\lambda = 532$ nm) was directed onto a phase-only SLM (HoloEye PLUTO VIS SLM with 1920×1080 pixels and calibrated for a 2π phase shift at $\lambda = 532$ nm). The SLM was used to vary the beam illuminating the axicon. By changing the phase pattern depicted on the screen of the SLM, the phase of the initial beam was modulated accordingly. Thereafter the respective beam was passed through a lens of focal length 40 mm followed by two axicons placed 75mm apart. The images were captured on a Scorpion IEEE 1394 CCD Camera (model SCOR-20S0). The following setup as constructed in the laboratory is shown in Fig. 5.9

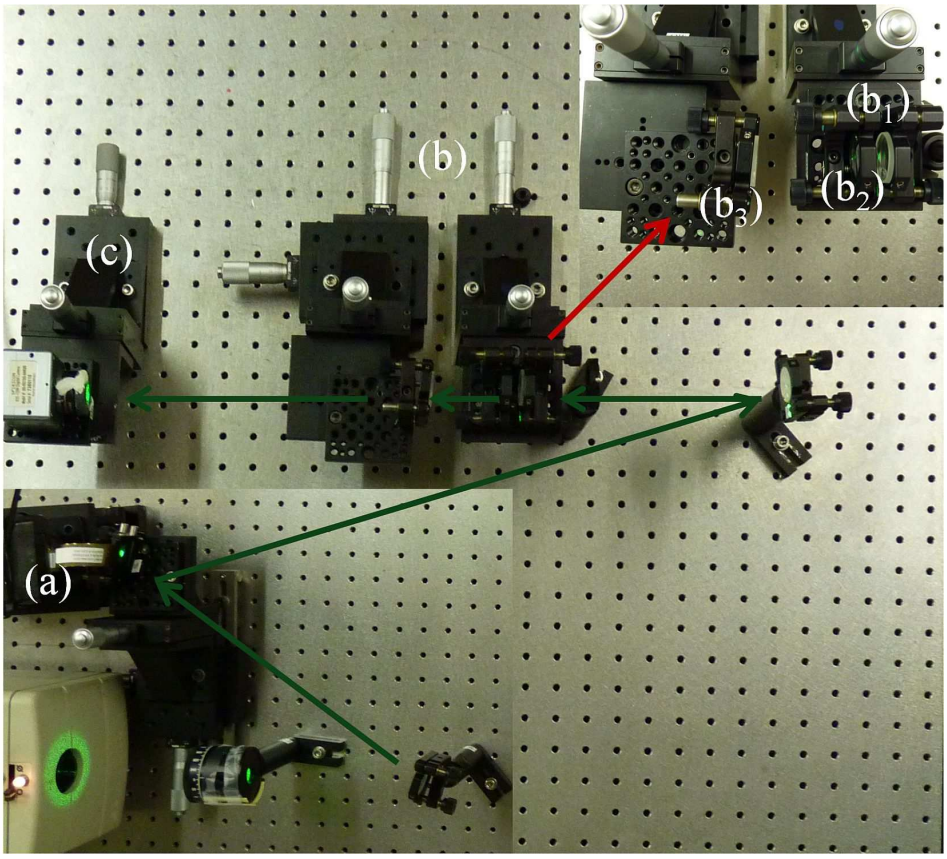

Fig. 5.9 Experimental setup to generate z-dependent Bessel-like beams: (a) Spatial light modulator (SLM); (b) double axicon lens system where (b_1) is the first axicon; (b_2) is a 40 mm lens and (b_3) is the second axicon and (c) is the Scorpion IEEE 1394 CCD Camera (model SCOR-20S0).

To further illustrate the concept of this new proposed optical scheme, Fig. 5.10 is an image of the double axicon and lens system as seen in the laboratory.

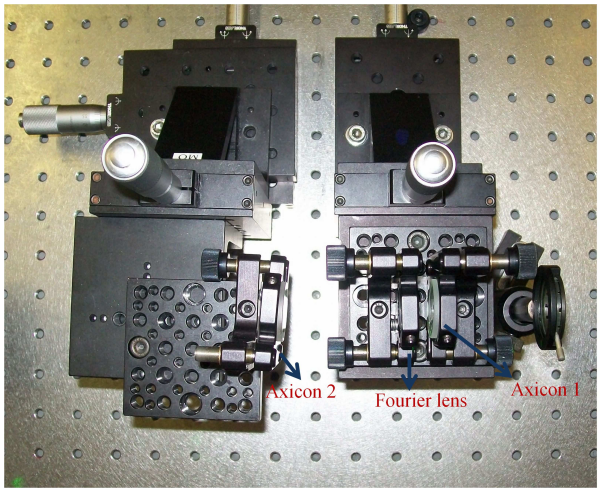

Fig. 5.10 Image emphasising the double axicon and lens system as set up in the laboratory.

When a uniform grey scale phase pattern was projected onto the SLM, a Gaussian beam will be passed through the system without any change which lead to a zero-order Bessel-like beam being produced not only in the near-field however in the far-field as well. By changing the phase pattern on the SLM, various orders Laguerre-Gaussian beams were produced leading to various higher-order Bessel-like beams being generated. For a higher-order Bessel-like beam carrying a topological charge of 1, the phase pattern on the spatial light modulator varied in phase from 0 to 2π once, depicted by the grey scale pattern changing from white to black once as mentioned previously. The Laguerre-Gaussian beam produced had a central zero intensity depicted by the central dark region and carried orbital angular momentum of $\hbar$. The corresponding Bessel-like beam also carried the properties of the Laguerre-Gaussian beam since it also had a central zero intensity surrounded by concentric rings. This was further carried out for various higher-order Bessel-like beams and a summary of some of the experimental results are shown in Fig. 5.11.

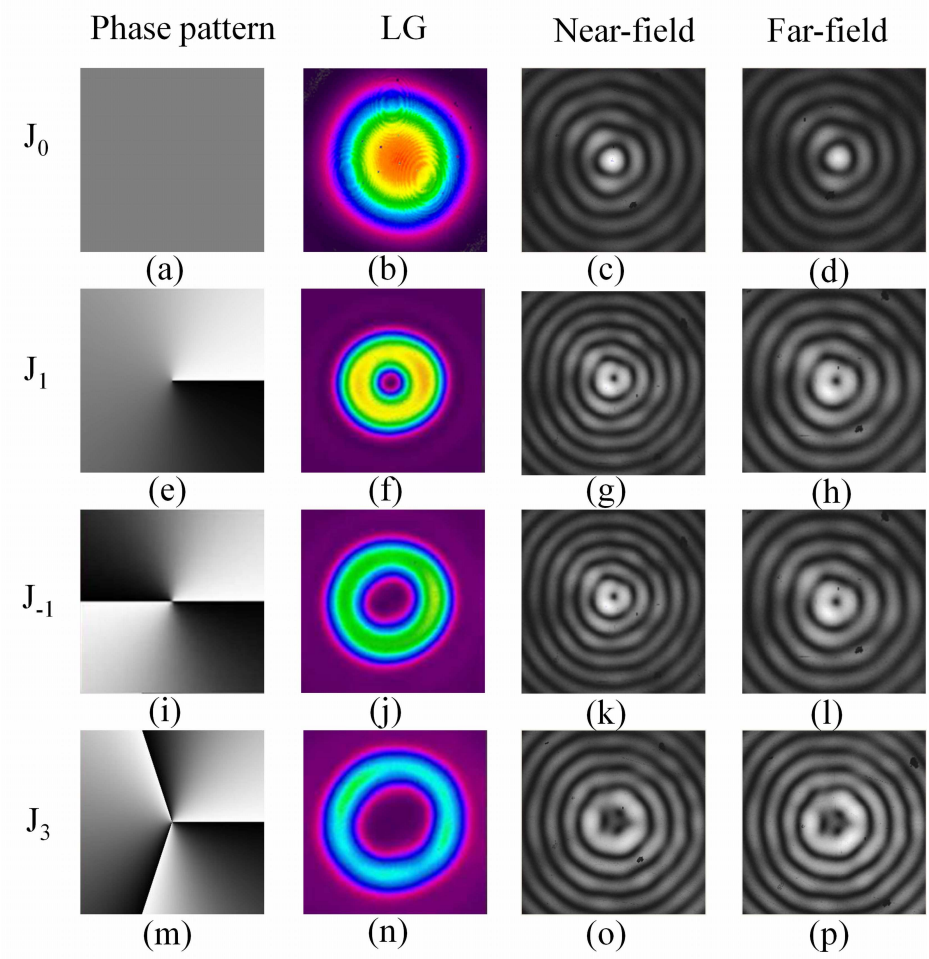

Fig. 5.11 Various order Bessel-like beams retaining their spatial distribution from the near- to the far-field: (a) is a uniform grey scale phase pattern which leaves the phase unchanged hence a Gaussian beam (b) passes through the double axicon system to produce a zero-order Bessel-like beam in the near (c) and far-field (d). The grey scale phase pattern (e) varies in phase once and allows a Laguerre-Gaussian beam of order one (f) to pass through the system producing a higher-order Bessel-like beam carrying a topological charge of one in the near (g) and far-field (h). The same can be said for (i) to (l) except the order of the charge is negative one. The grey scale phase pattern that varies in phase three times (m) leads to a Laguerre-Gaussian beam of order three (n) to pass through the system producing a higher-order Bessel-like beam carrying a topological charge of three in the near (n) and far-field (p).

Similar to Bessel beams, Bessel-like beams also undergo self-reconstruction however the position at which the obstruction has to be placed is not a limiting factor. To illustrate that these beams also possess the ability to self-reconstruct upon encountering an obstruction a ball bearing of diameter 0.120 ± 0.001 mm was placed in the path of a first order Bessel-like beam as shown in Fig. 5.12. The Bessel-like beam before reconstruction is represented in Fig. 5.12(a). Upon placing the ball bearing 200 mm away from the second axicon we observed that the central region of the beam was overshadowed by the obstacle as seen in Fig. 5.12(b) however the outer rings of the beam are still seen. Taking into account the diameter of the obstruction the shadow region was calculated to be 239.08 mm after the obstruction. By placing the camera on a rail we were able to image the beam at various positions after the obstruction to determine the distance at which self reconstruction occurs. We noticed that approximately 250 mm from the obstruction the beam started to reconstruct and at a distance 525 mm from the obstruction we noticed a complete reconstruction of the beam as illustrated in Fig. 5.12(c). Since the Bessel-like beams are not confined to distances $z < z_{max}$, the axial position at which the obstruction has to be placed is not a limiting factor. Of particularly interest is that Bessel-like beams retain their spatial distribution as they propagate hence there is a continuous interference of light rays throughout the optical axis. Due to this an obstruction placed outside the z_{max} region or even off the optical axis will still result in a successful reconstruction of the beam. In our case the obstruction was placed approximately 75.6 mm outside the z_{max} region and noticeably we obtained a well reconstructed Bessel-like beam.

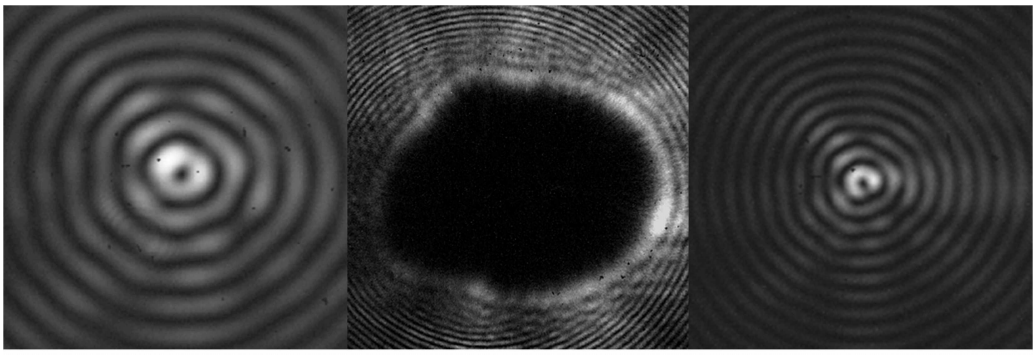

Fig. 5.12 Self reconstruction of a Bessel-like beam carrying a topological charge of 1: (a) the beam before encountering an obstruction; (b) overshadowing of the beam due to the obstruction being placed in its path and (c) the Bessel-like beam has undergone a complete self-reconstruction.

Thus far the existence of Bessel beams and Bessel-like beams with z-dependent cone angles been demonstrated. We have overcome the issue of the abrupt change in intensity distribution from the near- to the far-field as illustrated in Fig. 5.11. We have successfully proven that Bessel-like beams with z-dependent cone angles do exist however at the expense of losing their non-diffracting nature. To validate this statement we considered looking at the diffraction of the various order Bessel-like beams as they propagate. This was done by looking at the width of the beams at set intervals apart. The results obtained are illustrated in Fig. 5.13 and we notice that there is a linear increase in divergence. The zero-order Bessel-like beam diverges much more slowly in comparison to the higher-orders. The higher the order of the Bessel-like beam the greater the divergence.

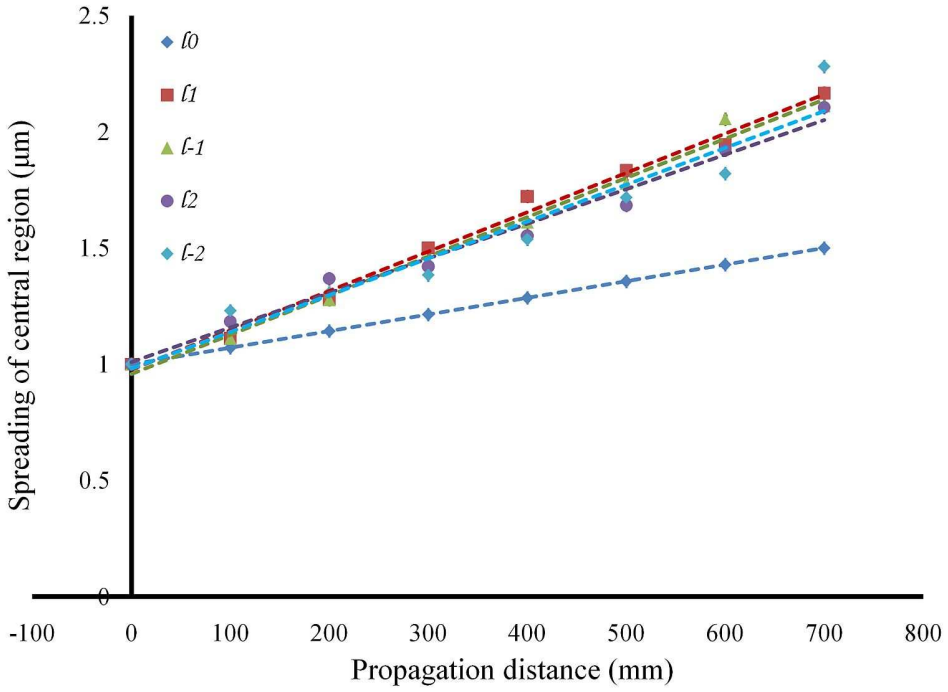

Fig. 5.13 Graph illustrating an increase in divergence of various order Bessel-like beams as they propagate from the near- to the far-field.

To investigate this increase in diffraction, we placed the camera on a rail and imaged a zero-order and a higher order Bessel-like beam with a topological charge of one at intervals of 50 mm increments over a distance of 1000 mm as represented in Fig. 5.14 and 5.15. By comparing the

frames in both figures it is apparent that there is change in magnification of the beam. For the zero-order Bessel-like beam, Fig. 5.14, it was the Gaussian part of the beam that spread out due to an increase in the propagation distance. On the other hand for the Bessel-like beam carrying a topological charge of one, Fig. 5.15, it was the Laguerre-Gaussian part of the beam that spread out. To validate this observation we measured the central region of the zero-order Bessel-like beam in Fig. 5.14 (frame a) to be approximately 13 μm and thereafter compared this value to frame (t) where the central region was measured to be 25 μm which concludes that these Bessel-like beams slightly diffract as they propagate. So far we have dealt with the generation of novel laser beams by passing a Gaussian beam through a spatial light modulator with the appropriate gray scale phase pattern. We showed that we were able to generate various order of Laguerre-Gaussian beams. We applied this concept to the generation of various higher-order Bessel beams using a conical lens known as an axicon. These beams exist for a finite region after which they spatially transform into a conical field. To overcome this abrupt spatial transformation from the near to the far field we considered an optical scheme that allowed us the opportunity to produce Bessel-like beams which retained their spatial distribution as they propagated. We now use the knowledge gained from the propagation of a Gaussian beam (Chapter two) and from the ability to shape a beam to build a single gradient optical trapping system which will be discussed in detail in the chapter that follows and further incorporate a Laguerre-Gaussian beam into an optical trap to observe the rotation of a trapped particle.

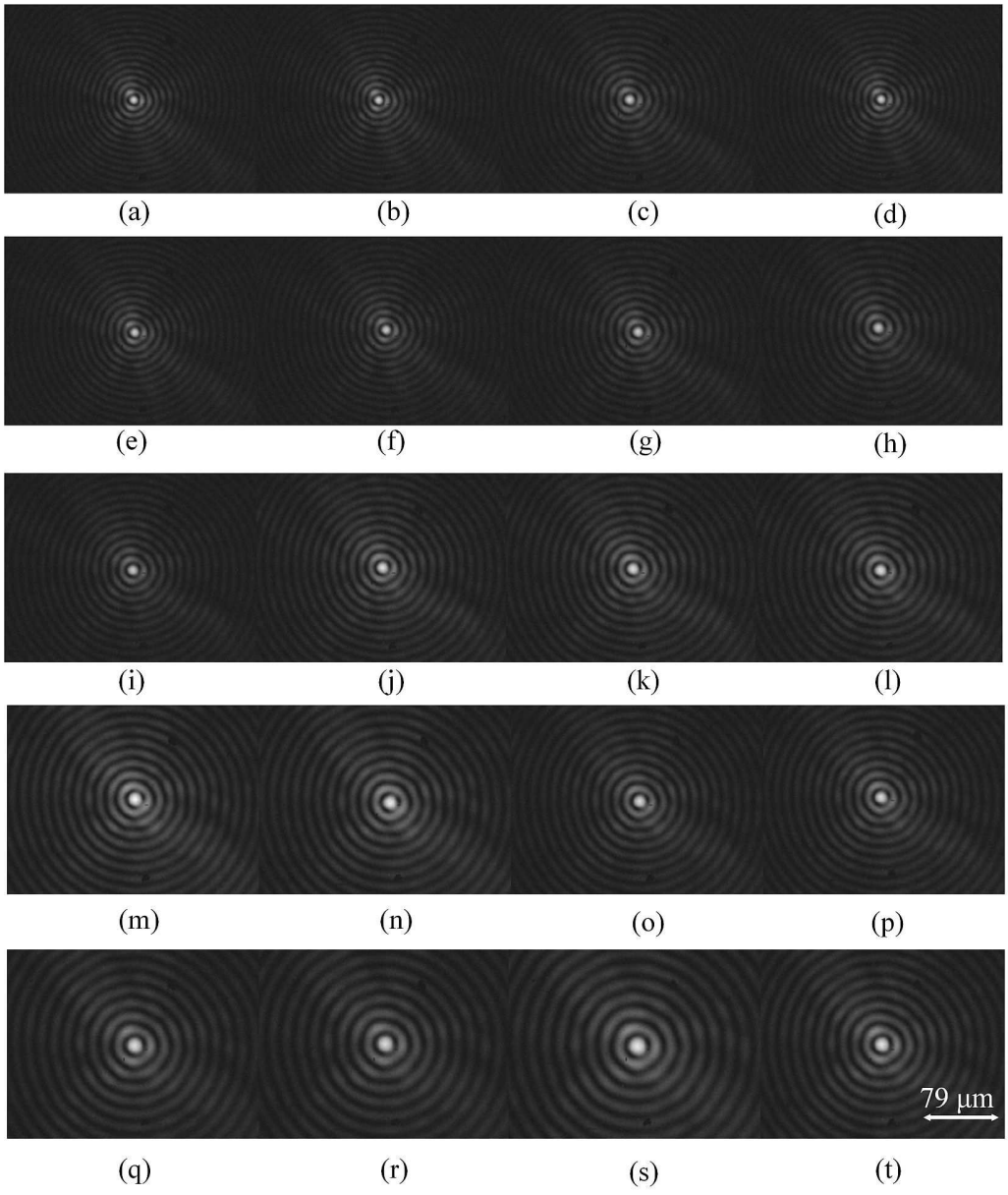

Fig. 5.14 Images of a zero-order Bessel-like beam retaining its spatial distribution as it propagates from the near- to the far-field.

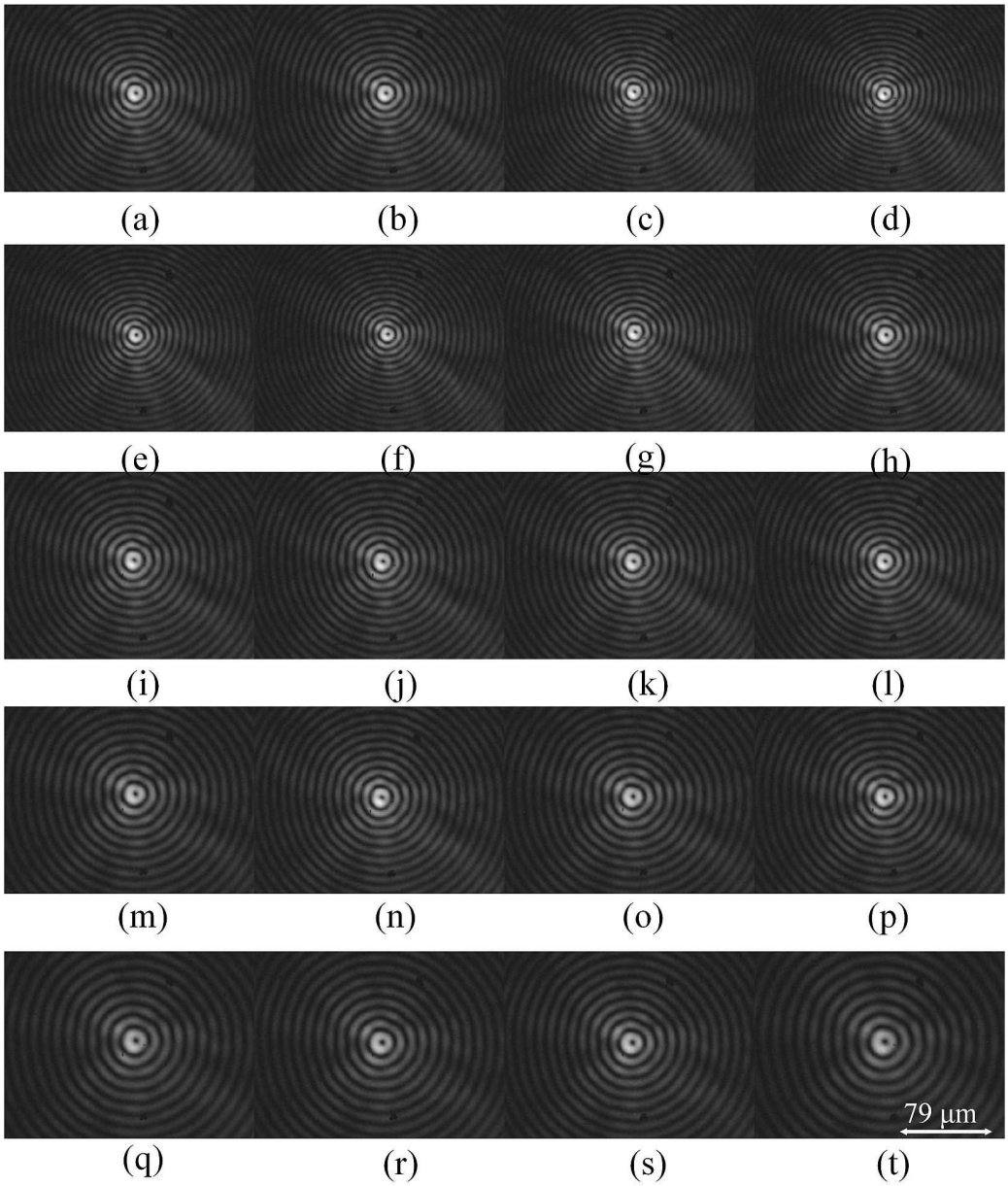

Fig. 5.15 Images of a higher-order Bessel-like beam carrying a topological charge of one retaining its spatial distribution as it propagates from the near- to the far-field.

Chapter 6

Demonstration of Optical Trapping and Tweezing

6.1 Single Gradient Optical Trap

Taking all the design considerations in section 4.3 into account, the optical trap in the laboratory was built according to the illustration depicted in Fig. 6.1. A diode pumped Nd:YAG frequency doubled laser (model MG-532C-2000) that lased at a wavelength of 532 nm was used which had a maximum power output of 400 mW however during the course of the experiments the power was set to 200 mW. The beam was passed through a polariser which attenuated the amount of power that was passed through the system. Mirrors M_1 and M_2 directed the beam towards a beam expander which consisted of two concave lenses of focal length 50 and 150 mm respectively. At this point the beam was magnified by a factor of 3, before it was passed through mirrors M_3 and M_4 which directed the beam towards the vertical axis of the trap. Upon leaving mirror M_4 the beam was steered onto a dichroic mirror which reflected the laser beam downwards into a 100x LOMO objective lens with a numerical aperture of 1.25 while it transmitted any other wavelength from the white light source.

At this point the beam was focused to a point onto a stage which held the sample. The sample was placed on a microscope slide of dimensions 75 mm x 25 mm. With respect to the sample preparation, a vinyl sticker of dimensions 20 mm x 20 mm was placed onto a microscope slide. This vinyl sticker had a hole of diameter 5 mm and thickness of 100 μm in the middle which acted as a well for the sample. The sample was placed on the vinyl sticker and covered by a coverslip (dimensions 20 mm x 20 mm). An image of the sample is shown in Fig. 6.2.

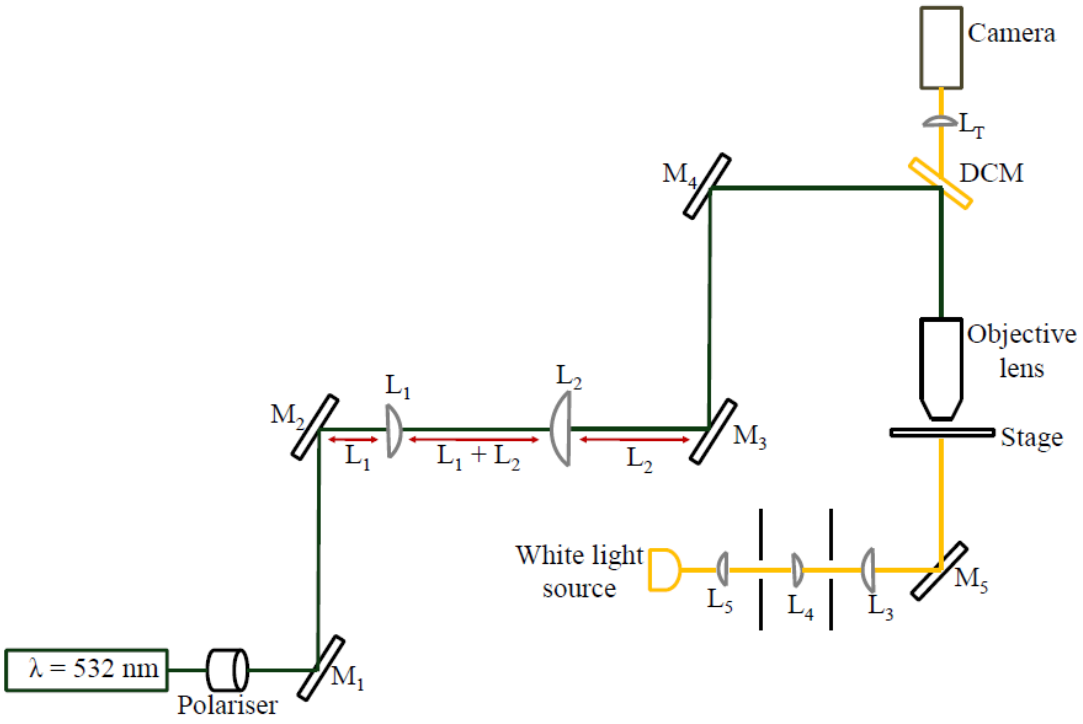

Fig. 6.1 Optical trapping system as built in the laboratory: The beam from a Nd:YAG laser lasing at 532 nm was directed through a polariser and reflected by two flat mirrors M_1 and M_2 towards a beam expander consisting of lenses L_1 and L_2. The beam was thereafter directed by mirrors M_3 and M_4 into the vertical axis of the trap onto a dichroic mirror which reflected the laser light into a 100x LOMO objective lens onto a stage. The stage held the sample which was illuminated by a Köhler illumination system made up of L_3, L_4 and L_5. A tube lens L_T was used to collect the light that was imaged onto a Scorpion IEEE 1394 CCD camera (model SCOR-20S0).

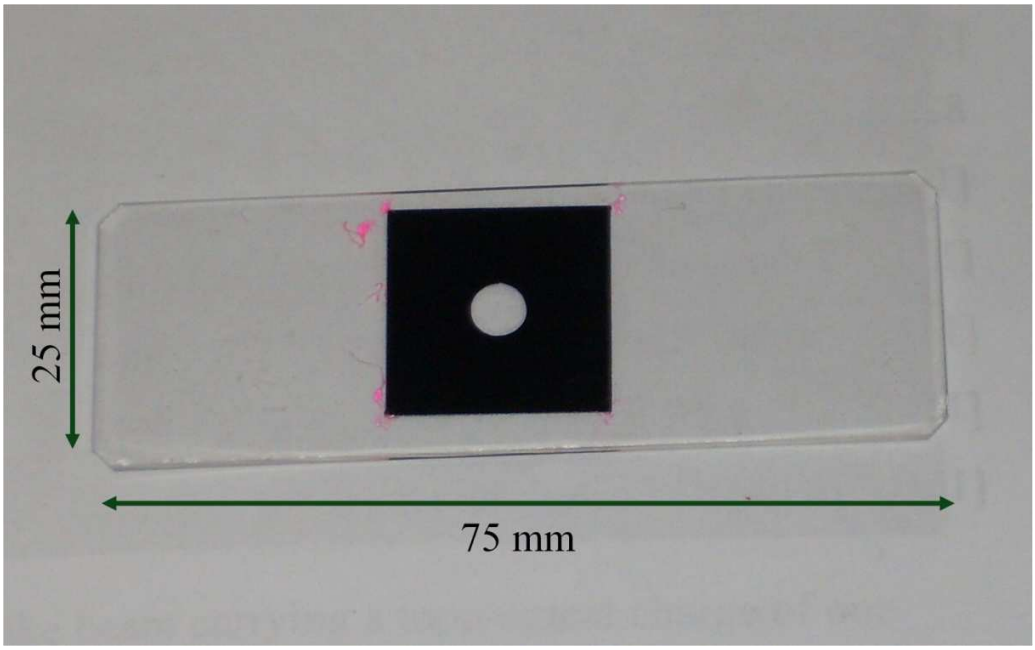

Fig. 6.2 Microscope slide containing the sample of silica beads 4 μm diameter in distilled water.

To give an idea as to what is meant by the well in which the sample sat, refer to Fig. 6.3 where the dimensions of the well is 5 mm x 5 mm with a thickness of 100 μm (i.e. the dimensions of the vinyl sticker) in which the sample was placed.

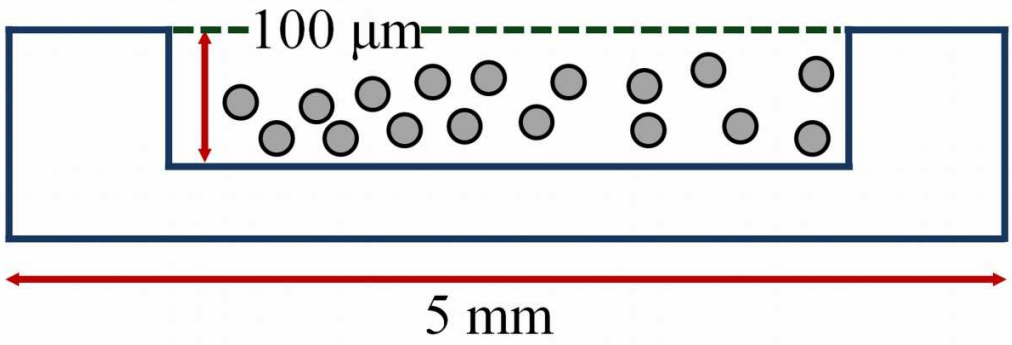

Fig. 6.3 Illustration of the sample on the microscope slide where the depth of the well the sample is placed in is 100 μm.

To ensure that enough light passed through the sample for imaging of the trap a Köhler illumination system was set up so that there was an even illumination of the sample by a uniform amount of light where a white LED (Light emitting diode) was used as the light source.

The trap was imaged to a Scorpion IEEE 1394 CCD camera (model SCOR-20S0) and a tube lens of focal length 150 mm was used to collect the light onto the camera since an infinitely corrected objective lens was used. Fig 6.4 is an image of the trapping system as set up in the laboratory.

Fig.6.4 Optical trapping system as set up in the laboratory: the beam passes through two mirrors onto the dichroic mirror which directs the beam into the 100x microscope objective lens. The sample is illuminated below and captured by a Scorpion IEEE 1394 CCD camera (model SCOR-20S0).

An experimental image of a trapped particle is seen in Fig. 6.5. As observed the particle that is trapped is the one that is in focus while the rest of the particles are out of focus. This is an example of axial trapping.

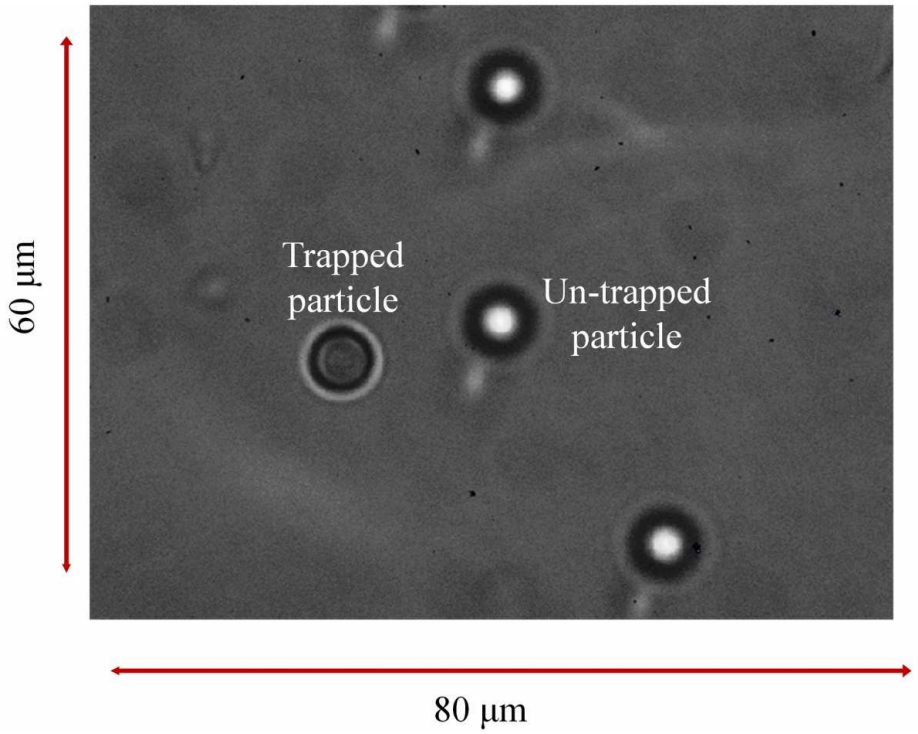

Fig. 6.5 Experimental image of a trapped particle (in focus) surrounded by un-trapped particles (out of focus).

Once a particle is trapped it can be held within the trap until it is forced to dislodge. Alternatively it can be moved around by merely moving the laser beam by manually moving one of the beam steering mirrors. This is illustrated in Fig. 6.6; the solid circle indicates the current position of the particle while the dashed circle indicates the position at which the particle was previously located. The images in Fig. 6.6, demonstrate that the particle was moved in a triangular motion until it was brought back to its initial position.

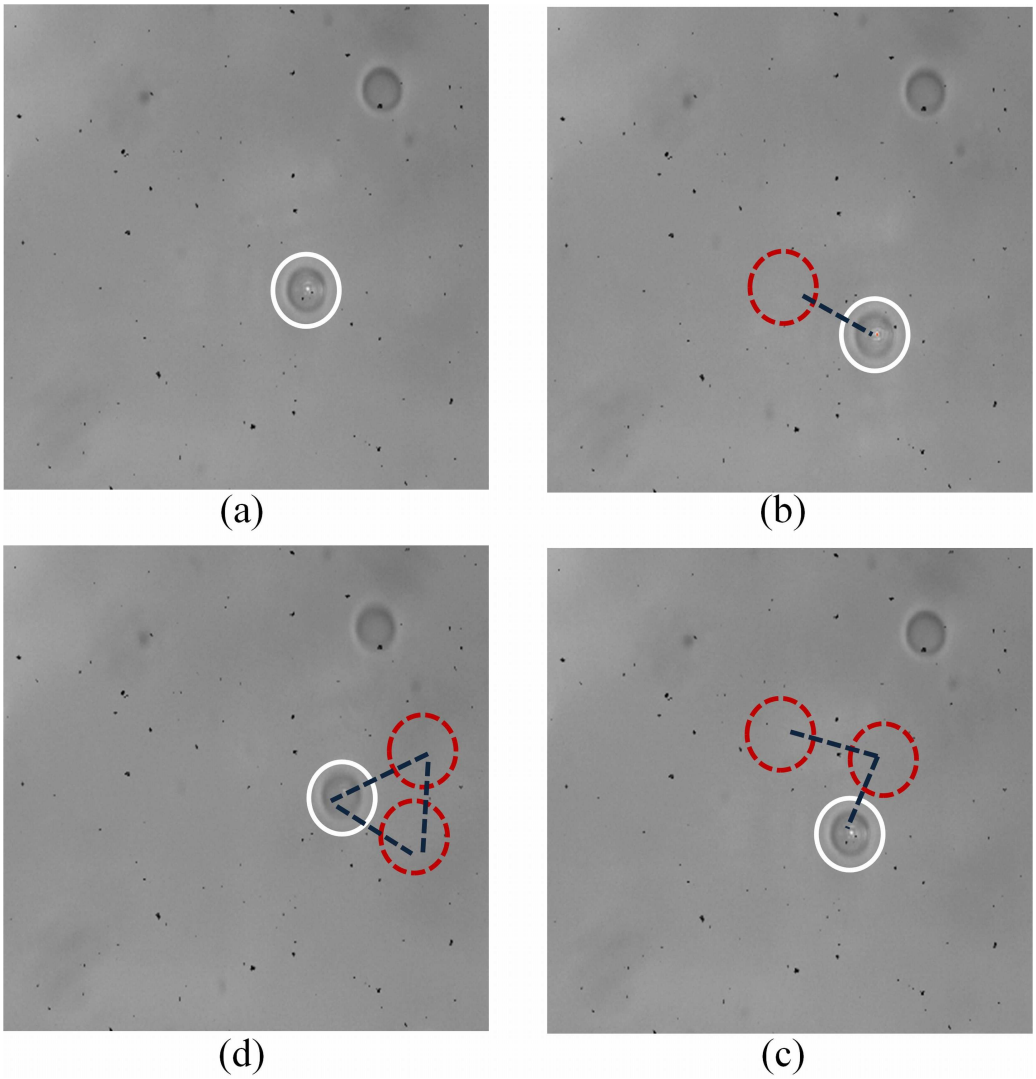

Fig. 6.6 Manipulation of a trapped particle in triangular movement: the particle is first trapped (a), thereafter movement of the laser beam causes a movement of the particle (b), where the white circle is the position to which the particle was moved while the red dashed circle indicates the position the particle was previously at. This movement is further seen in (c) and (d), whereby the particle was almost returned back to its original position.

Furthermore, slight movement of the stage caused the surrounding particles to move, while the trapped particle remains fixed as seen in Fig. 6.7.

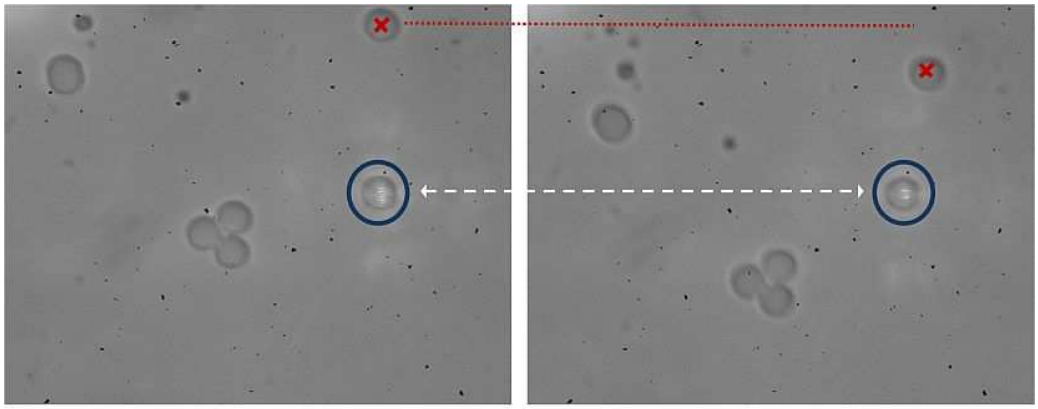

Fig. 6.7 Movement of the stage while keeping the trapped particle fixed: in frame (a) the trapped particle is represented by a blue circle while a surrounding particle is marked with a red cross. After the movement of the stage (b) we observe that the trapped particle is still at the same position however the surrounding particle marked with the cross has been displaced from its initial position.

In Fig. 6.7(a) the particle that is trapped is circled and a surrounding reference particle is marked with a red x, the movement of the stage causes the reference particle to move Fig. 6.7(b) however the trapped particle still remains fixed as seen by the dotted arrow.

6.2 Determining the Strength of the Trap

6.2.1 Calibrating the Trap Using the Drag Force Method

Experimentally, the drag force was measured by accurate control of an automated stage (Optiscan ES10). The stage was set to increase in speed linearly in order to dislodge the particle from its equilibrium position, and hence the velocity at which the particle was dislodged from the trap was obtained by measuring the displacement of the trapped particle. Since the frame rate was set at 15 frames per second the time difference between consecutive frames was 0.0667 s

Using this knowledge the velocity at which the particle escaped the trap was determined as

$$v_c = \frac{\Delta x}{\Delta t}, \tag{6.1}$$

where Δx is the distance that the particle displaces and Δt is the difference in time. Thereafter using the drag force equation seen in Eq. (4.9) the trapping force was determined. For a power output of 10 mW we measured a velocity 2.27×10^{-5} m/s resulting in a trapping force of 0.928 pN. This analysis was carried out for various trapping powers and results attained are depicted in Fig. 6.8. The experimental results confirm the linear relationship between the trap stiffness and the power of the trapping laser. For an output power of 10mW the trapping force was determined to be 0.928 ± 0.505 pN however for a 100mW power output the trapping force was 6.187 ± 1.323 pN. This confirms that the higher the trapping power the stronger the optical trap. As observed there is an increase in the error of the measurement as the power passing through the system was increased. This could be due to a misinterpretation of displacement distance of the particle upon escaping the trap.

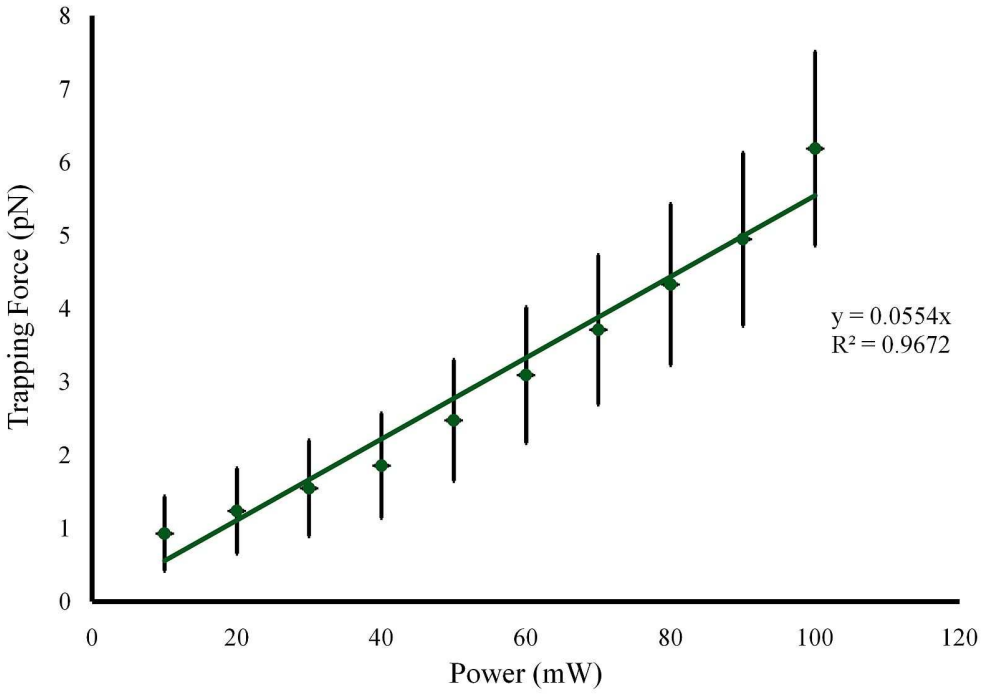

Fig. 6.8 Plot representing the drag force method showing the effects the trapping power has on the trapping force.

6.2.2 Calibrating the Trap Using the Equipartition Method

Here National Instruments-Labview was used as a tool to determine the displacement of the particle from its equilibrium position which was recorded by CMOS camera (Marlin, model F131B). By measuring the displacement of the trapped particle from its equilibrium we obtained an approximate Gaussian distribution as shown in Fig. 6.9. For this particular distribution the variation in displacement from its equilibrium position was 0.0025 μm.

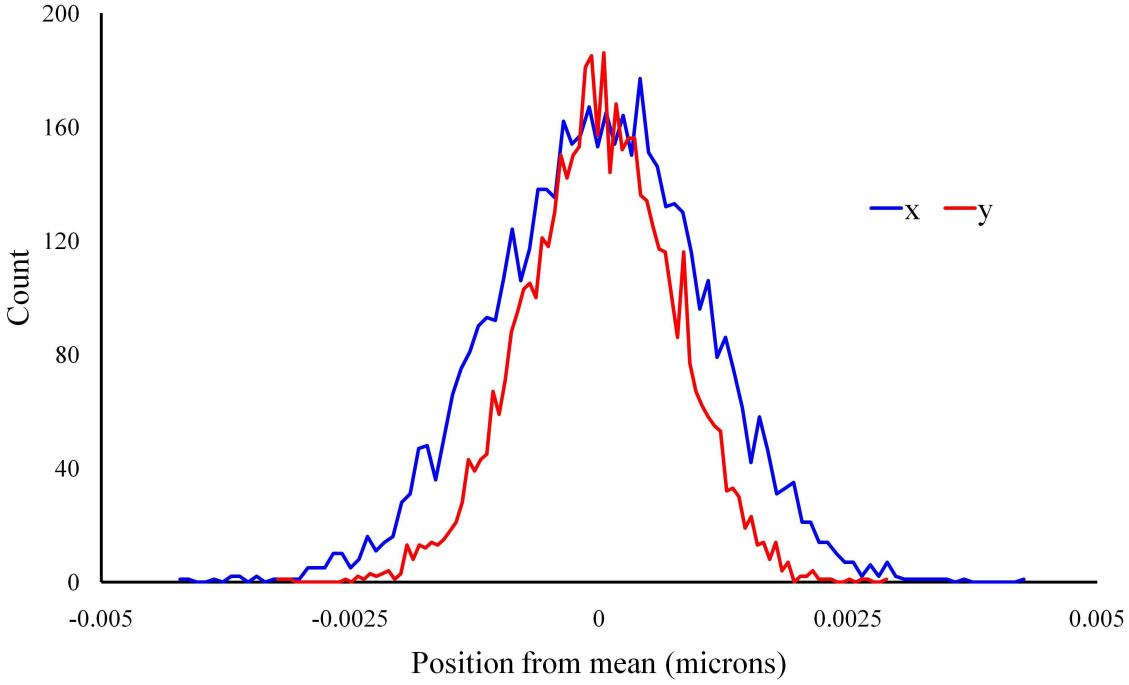

Fig. 6.9 The particle distribution representing the displacement of a trapped particle from its equilibrium position.

By measuring this variation in displacement while varying the power, we were able to use the equipartition equation Eq. (4.11) which makes use of the absolute temperature and Boltzmann's constant to determine the trap stiffness κ, where $\langle x^2 \rangle$ is the variation of the particle from its equilibrium position. It is known that the particle oscillates within the potential well hence the trapping force was determined from Hooke's law where the trap stiffness is directly related to the trapping force. For a power output of 10 mW in the x-direction we measured a variation in displacement of 2.50×10^{-5} m by tracking a trapped particle for a 1000 frames which resulted in a

trapping force of 1.847 pN. The results obtained for the various powers are illustrated in Fig. 6.10. The trapping force at 10 mW trapping power was (1.85 ± 0.18) pN in the x direction and (7.03 ± 1.37) pN in the y direction while at 100 mW the force measured in the x direction was (1.83 ± 0.18) pN and the y direction 7.223 ± 0.176 pN. Yet again we see a near-linear relationship between the trapping force and the trapping power.

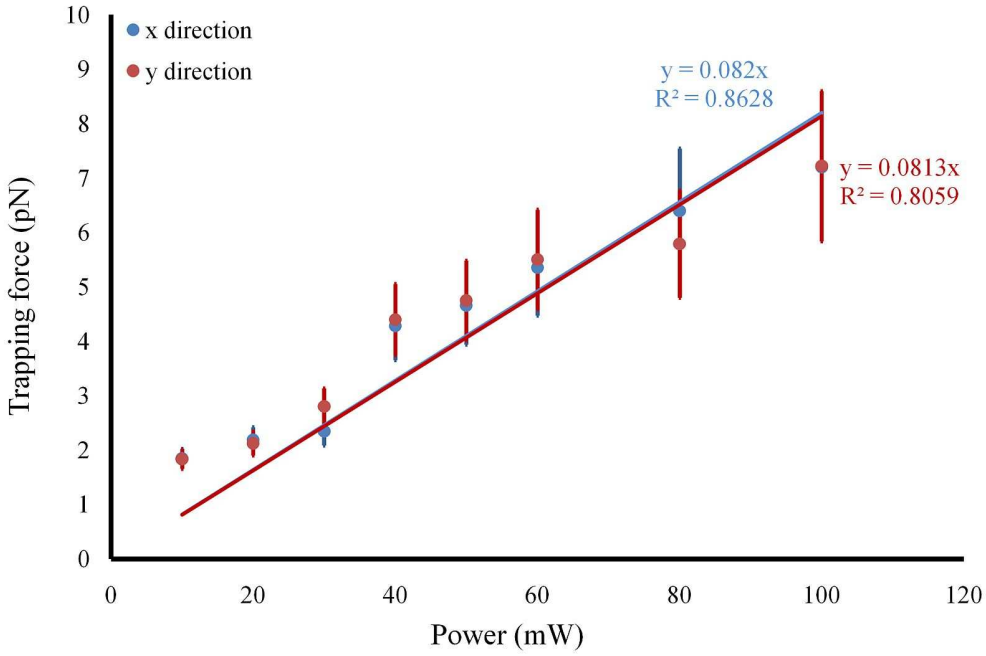

Fig. 6.10 Plot representing the equipartition method showing the effects the trapping power has on the trapping force.

It is apparent that there was an increase in the error of our measurements with an increase in trapping power. This is due to the fact that at higher powers the variation of the trapped particle become more difficult to examine since the particle is more strongly bound.

6.2.3 Calibrating the Trap Using the Power Spectrum Method

For the power spectrum calibration the centre of mass algorithm was used as the appropriate tracking method and National Instruments-Labview as a tool to carry out the tracking which was recorded by a CMOS camera (Marlin, model F131B). Once a particle was trapped, a region of interest was chosen as in Fig. 6.11(left) in order to decrease the field of view in which the software would track. The threshold was increased so the trapped particle is well defined as seen in Fig. 6.11(right) to alleviate any noise from the background while tracking.

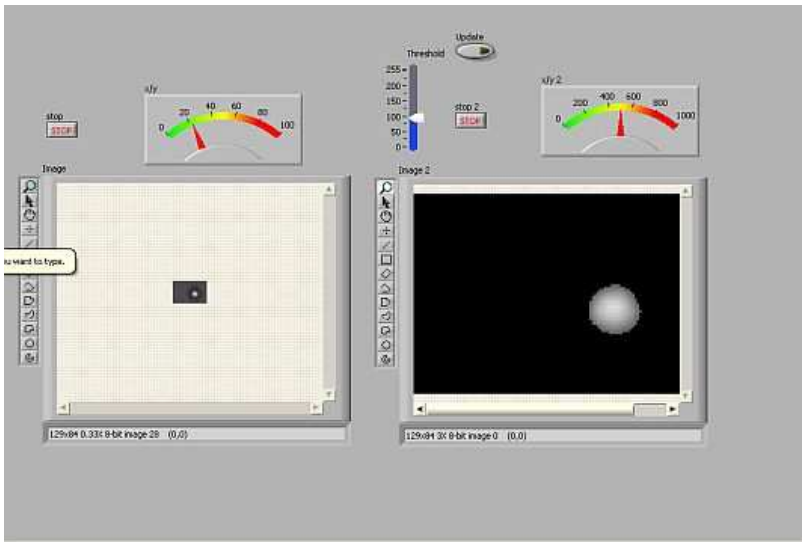

Fig. 6.11 Image of a trapped particle used to determine the corner frequency from the power spectrum method.

Once the particle was trapped, we used the software to track the particle until we obtained 30 000 data points over a period of approximately 30 minutes from which the power spectrum was plotted as seen in Fig. 6.12.

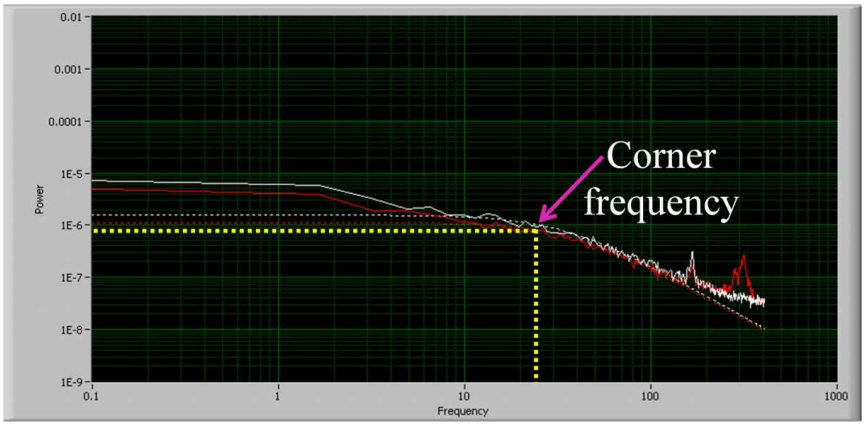

Fig. 6.12 The power spectrum illustrating the Brownian motion of a trapped particle at a trapping power of 100 mW.

By extracting the corner frequency from the power spectrum, the trap stiffness was determined using Eq. (4.5) where f_c is the corner, η is the viscosity of the medium and κ is the trap stiffness. For a power output of 10 mW we measured a corner frequency of 3.35×10^{-6} *Hz* by tracking a trapped particle for 30 000 frames which resulted in a trapping force of 0.860 pN. This analysis was carried out for various powers and the results obtained are illustrated in Fig 6.13. As observed there is a linear relationship between the trap stiffness and the trapping power. For a power output of 10 mW, the trap stiffness was measured to be (0.86 ± 0.21) pN while for a power of 100 mW the trap stiffness was (3.64 ± 0.43) pN. The discrepancies of this method are influenced by the tracking of the particle since the particle was tracked for so many frames to obtain a satisfactory power spectrum, the measurements were taken over a duration of 30 minutes. The centre of mass method was chosen for the tracking particle however this tracking algorithm is very susceptible to a change in environment and noise. Small movement in and around the trap influenced the displacement of the particle and hence the results obtained.

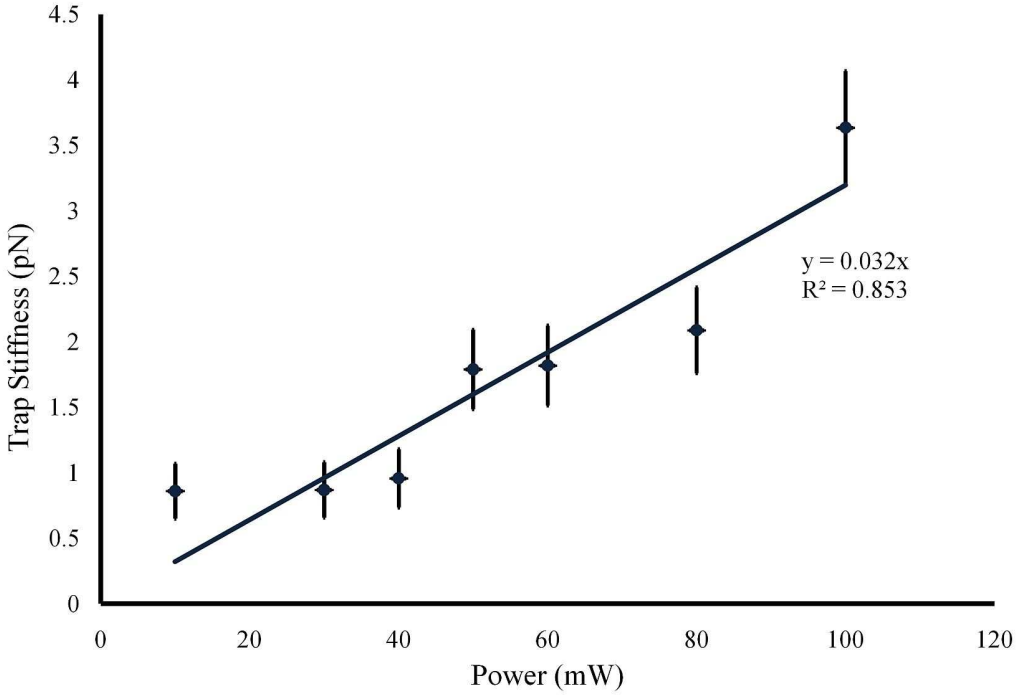

Fig. 6.13 Plot representing the power spectrum method showing the effects the trapping power has on the trapping force.

Overall all three methods confirm a near-linear relationship between the trapping power and the trapping force. Thus far we have looked at a single gradient optical trap however by manipulating a Gaussian beam we are able to build an optical trap to include novel beams. The next section will concentrate on adapting the optical trap to include trapping with a beam carrying orbital angular momentum.

6.3 Optical Trapping Illustrating the Transfer of Orbital Angular Momentum

Until now we have seen trapping due to the transfer of linear momentum. However it is possible to achieve trapping due to the transfer of angular momentum (Rubinstein-Dunlop *et al.*, 1998). Angular momentum can be decomposed into two components namely spin angular momentum which arises due to polarization and orbital angular momentum which arises due to the spatial distribution (Allen *et al.*, 1992). Over the years a considerable amount of work has been carried out with respect to the effects of spin angular momentum dating back to 50 years ago by Beth and

colleagues (Beth, 1936). Demonstrating trapping with respect to spin angular momentum is attained by introducing a quarter wave plate into the optical system. By rotating the quarter wave plate, the polarisation of the beam is varied and hence the trapped particle will tend to spin or rotate (Galajda & Ormos, 2003; Ibenech, 2008). The rest of this section will deal with the transfer of orbital angular momentum. In Chapter two, we discussed the existence of beams carrying orbital angular momentum and mentioned different methods to create such beams, however, from this point onwards, we only consider Laguerre-Gaussian beams. It is known that these beams carry orbital angular momentum dependent on the topological charge of the beam, so that placing these beams into an optical trap will initiate a transfer of orbital angular momentum from the beam to trapped particle, hence causing the particle to rotate. The rate of rotation of the particle can be determined from

$$\Omega = \frac{\omega}{2\pi}, \tag{6.2}$$

where ω is the angular speed given by

$$\omega = \lim \frac{\Delta\theta}{\Delta t}, \tag{6.3}$$

where $\Delta\theta$ and Δt are the change in angular position and time respectively. Using Eq. (6.2) and Eq. (6.3), the torque exerted on the particle can be calculated taking in consideration that within a viscous medium, the torque is associated with the drag torque such that the torque exerted on the particle is dependent upon the drag coefficient and the rate of rotation given as

$$\tau = 8\pi\eta r^3 \Omega, \tag{6.4}$$

where Ω is the rate of rotation, r is the radius of the particle and η is the viscosity of the medium which in this case is 1.003×10^{-3} $Nm^{-2}s$. Since the rotation is caused due to the transfer of orbital angular momentum, the particle has to absorb photons in order to see the rotation. Hence the silica beads are replaced by graphite particle since they absorb more easily. These particles are prepared in dilute ethanoic acid. The rotation due to the transfer of orbital angular momentum by a Laguerre-Gaussian beam carrying a topological charge of one is seen in Fig. 6.14.

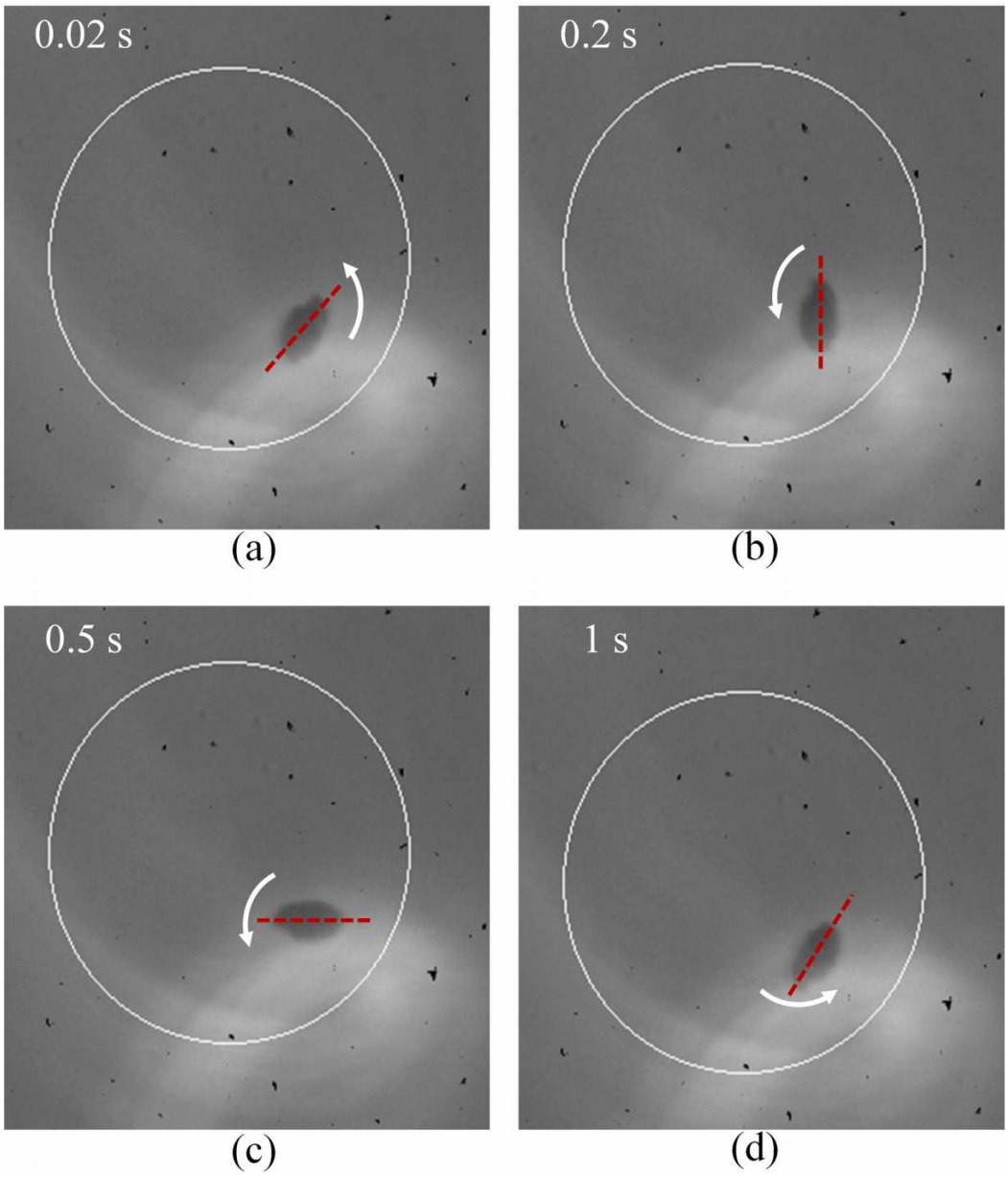

Fig. 6.14 Rotation of a graphite particle with a Laguerre-Gaussian beam carrying a topological charge of one.

The particle rotates in an anti clockwise direction. In order to calculate the rate of rotation the angular position has to be determined. Clearly it is seen in frames (b) and (c) of Fig. 6.14, the particle has rotated by an angular position of $\pi/2$ hence using Eq. (6.3) the angular speed is

determined to be 5.24 rads/s. Using this result, one can calculate the rate of rotation using Eq. (6.2), which is calculated to be 0.83 Hz. Furthermore the torque acting on the particle is determined to be 2.09×10^{-20} Nm using Eq. (6.4). A Similar analysis can be carried out for higher order Laguerre-Gaussian beams. The higher the order of the Laguerre-Gaussian beam, the greater the amount orbital angular momentum carried by the beam since the orbital angular momentum is charge dependent hence it can be stated that the higher the topological charge, the greater the amount of orbital angular momentum carried by the beam, the faster the rate of rotation.

Chapter 7

Discussion

Prior to setting up a single gradient optical trap there were certain considerations that have to be taken into account. One factor that affects the stability of the trap is the beam that is passed through the system hence to build an optimum trap one would require a beam with good beam quality factor. The beam quality factor affects the symmetry of the beam, although it is possible to trap with an elliptical beam, it is preferable to have a beam with a circular symmetry. Typically a Gaussian beam has a beam quality factor close to one and is circularly symmetric. This was experimentally validated by looking at the transverse profile of the beam as it propagated in the z direction where the M^2 value was determined to be 1.15 ± 0.65 which is marginally close to one and satisfactory for the proposed application.

A home built single gradient optical trapping system was built in accordance to the design considerations stipulated in section 4.3 where we used an appropriate beam expander to ensure the beam was large enough to slightly overfill the back aperture of the objective lens. We used a 100x microscope objective lens with a numerical aperture of 1.25 which meant we obtained a tightly focused diffractive limited spot. One can still obtain trapping with a lower magnified objective lens however for optimum trapping a high numerical aperture is required which is the reason for the choice of our objective lens. The sample was illuminated by a Köhler illumination system which we found gives an even distribution of light on the sample. It is important that the sample is well illuminated so that the trap can be visualised on the camera. An infinitely corrected objective lens was used hence a tube lens was included in the system so that the trap was imaged onto the camera.

It was shown that 4 μm diameter silica beads that were prepared in distilled water were successfully trapped, and were able to be manipulated in three dimensions as was shown in Fig. 6.6. Furthermore it was illustrated that movement the stage caused the surrounding particles to move however the trapped particle stayed stably trapped.

Using the three calibration methods discussed in section 4.4 we were able to determine the efficiency of our trapping system by varying the power that we passed through the trap. The drag force method was the most direct method which illustrated the effects that the viscous drag has on a trapped particle. If the viscous drag is strong enough the particle will dislodge from the trap and by determining the velocity with which the particle escaped we were able to use the Stokes' drag to determine the trapping force acting on the particle. Carrying out this analysis at various powers showed that an increase in trapping power leads to an increase in trapping force and that the trapping is linearly related to the trapping power as seen in Fig. 6.8 The trapping force at 100 mW was measured to be (6.19 ± 1.32) pN while at 10 mW we obtained a trapping force (0.93 ± 0.51) pN. This method is dependent upon the size and shape of the particle being trapped and the viscosity of the medium has to be known.

Carrying out the equipartition method yielded a similar trend for the relationship between the trapping force and the trapping power. The variation of the trapped particle from its equilibrium position due to thermal fluctuations that were present in the medium was used to determine the variation from the trapped position and since the particle acts as a harmonic oscillator hence it obeys Hooke's law, the trapping forces were determined. This method is independent upon the size of the particle and the viscosity of the medium. At 100 mW we obtained a trapping force of (7.03 ± 1.37) pN in the x direction and (7.22 ± 0.18) pN in the y direction while at 10 mW the trapping force measured was to be (1.85 ± 0.18) pN in the x direction and (1.83 ± 0.18) pN the y direction.

The last calibration method carried out was the power spectrum method which like the equipartition method makes use of the displacement of the particle from its equilibrium position to determine the trap stiffness. The displacement of a trapped particle was tracked until 30 000 data points was obtained such that a set of data for the displacement of a particle over a period of time was attained. A Fourier transform of the data yielded the power spectrum. This spectrum illustrated the Brownian motion of a trapped particle which showed the region at which the particle was trapped, just about escaped the trap and was said to be free. The frequency at which the particle just about escapes the trap was known as the corner frequency hence the trapping power was varied and the corner frequency was measured for each power such that the trap stiffness was determined. Similar to the other two methods we obtained a linear relationship between the trapping power and the trap stiffness. At 100 mW we obtained a trap strength (3.64 ± 0.43) pN while at 10 mW the trap strength

measured was (0.86 ± 0.21) pN. This method is also dependent upon the size of the particle and the viscosity of the medium.

There are discrepancies in the power spectrum method as opposed to the other two methods however all three methods showed the same linear trend between the trapping power and the trapping force. The reasons for the discrepancies of the results obtained vary for each method. For the drag force method, the velocity at which the particle escapes the trap is used to determine the trapping force, and at higher powers there is a greater error in determining this velocity since it is harder to determine the actual distance the particle displaces. This is due to stronger flow pushing the particle further away from the trap which results in a misinterpretation of the displacement distance. With respect to the equipartition method, at higher power the particle is more tightly bound hence it is harder to visualise the displacement of the particle from its trapped position. At higher powers this displacement is much smaller resulting in a higher error in the measurement of variation of the particle displacement. The power spectrum method gave the lowest measurements of the trapping force. This method makes use of algorithm to track a trapped particle hence one of the reasons for the discrepancies in the results could be due to the choice of algorithm. We used the centre of mass algorithm to track our particles; this algorithm is very susceptible to change of the environment of the particle which means small amounts of noise can affect the tracking process. Overall all the methods emphasise the importance of the trapping power on trapping force. Knowing the efficiency of the system is vital information that is required for certain applications.

Interest does not only lie in the building of single gradient traps however in the past couple years a lot of work has been carried out in novel traps. The generation of novel beams are possible making use of diffractive optics. We used a Gaussian beam as our starting field in all our experiments to generate various novel beams which include Laguerre-Gaussian beams, Bessel beams and Bessel-like beams.

Laguerre-Gaussian beams are of interest since they carry orbital angular momentum. A spatial light modulator was used to vary the phase of our starting field accordingly to produce various order Laguerre-Gaussian beams. It was shown that a using grey scale phase pattern that varied in phase from 0 depicted by white to 2π depicted by black we could generate a Laguerre-Gaussian beam carrying a topological charge of one which should carry orbital angular momentum amount equal to $\ell\hbar$ since the amount of orbital angular momentum carried by the beam is dependent upon the topological charge. We were able to produce various orders Laguerre-Gaussian beams as illustrated

in Fig. 5.3 by varying the grey scale pattern addressed to the spatial light modulator. We further incorporated a Laguerre- Gaussian beam carrying a topological charge of one into the optical trapping system and observed a clockwise rotation of a graphite particle which confirms that these beams do carry orbital angular momentum which can be transferred to a trapped particle.

We also experimentally produced Bessel beams which are a class of non diffracting beams and further went on to experimentally validating the existence of Bessel-like beams. Bessel beams are well known for their non-diffracting and self reconstructive properties. We used an axicon to generate zero and higher-order Bessel beams. In the case of a zero order Bessel beam, we passed a Gaussian beam through the system and generated a Bessel beam in the near field which had an intensity profile of a central bright spot surrounded by concentric rings which in the far field transformed into a conical field represented by an annular ring. Using the knowledge gained from generating various order of Laguerre-Gaussian beams we were able to produce higher order Bessel beams by varying the field that was passed through the axicon. These Bessel beams illustrated the same properties of a Laguerre-Gaussian beam since it also had a central zero intensity and the far field intensity profile obtained was an annular ring.

Considering that this abrupt change in intensity profile from the near to the far field can be a major disadvantage to these beams, we came up with a new optical scheme that overcame this problem. Using a double axicon system such that we varied the cone angle with respect to the propagation distance we were able to successfully produce a Bessel beam that retained its spatial distribution as it propagated from the near to the far field and so named these beams Bessel-like beams.

By passing a Gaussian beam through this double axicon system we produced a zero order Bessel like beam which like a zero order Bessel beam had a central bright spot surrounding by concentric rings however it retained its spatial distribution as it propagated. We replaced the starting field to allow various order of Laguerre-Gaussian beams to pass through the system and produced higher order Bessel like beams which also had a central zero intensity. It is well known that Bessel beams undergo self reconstruction, and to test that the same property holds for Bessel like beams we placed an obstruction in the path of a Bessel-like beam and showed successful reconstruction. The difference between a Bessel and Bessel-like beam is that there is no limitation on the position of obstruction. For a Bessel beam the obstruction has to be placed within the non-diffracting region, however since Bessel-like beams retain their spatial distribution as they propagate the obstruction can be placed at any position along the propagation axis.

Retaining the spatial distribution of a Bessel beam is an advantage, although this was achieved at the expense of losing the non diffracting nature of these beams which was experimentally shown by considering the spreading of the central region of these beams as they propagate, the slight diffraction being linear with an increase in propagation distance. The higher the order of the Bessel-like beam the greater the diffraction. Even though these beams are quasi non-diffracting, Bessel-like beams are an interesting addition to the class of Bessel beam.

Overall using a spatial light modulator is a useful tool to produce novel beams which when incorporated into an optical trapping system can yield interesting results.

Chapter 8

Conclusion

8.1 Summary

The aim of this work was to generate novel beams and utilise them within an optical trapping system. In chapter two we dealt with understanding the properties and behaviour of a Gaussian beam. From the Helmholtz equation we derived the field of a Gaussian beam and thereafter looked at understanding each parameter that affects the field. We showed that a Gaussian beam is propagation invariant hence it retains its spatial distribution as it propagates, although not its size. We also looked at how a Gaussian beam would propagate when encountering an optical element such as a thin lens and from this we were able to show how the imaging equation was derived. By using a thin lens and determining the width of a Gaussian beam at set intervals away from the lens we were able to use the quadratic form of Eq. (2.33) to determine the quality of a beam which is the M^2 value. For our laser the M^2 was approximately one which denoted we had a good quality Gaussian beam.

We went on to using our knowledge of a Gaussian beam to generate various novel laser beams. Using a diffractive optical element known as a spatial light modulator (SLM) to vary the phase of a Gaussian beam according to the appropriate grey scale phase pattern projected onto the screen of the SLM we produced various order of Laguerre-Gaussian beams which carry orbital angular momentum. We showed that these beams diffract slightly as they propagate. A class of non-diffracting zero- and higher-order Bessel beams were produced using a conical optical element known as an axicon. These beams exist for a finite propagation distance after which they undergo a spatial transformation into a conical field depicted by an annular ring. Of interest was the idea of generating Bessel-like beams, which are demonstrated experimentally for the first time. These beams should make their mark in the field of optics due to the fact that they retain their spatial distribution as they propagate from the near- to the far-field or in better terms towards infinity

however they do so at the loss of their non-diffracting nature as seen by the divergence of the various higher-order Bessel-like beams. It was illustrated that like Bessel beams they also undergo self reconstruction.

The principles of an optical trapping system have been investigated, with particular emphasis in understanding how the variation in the size of the particle with respect to the wavelength of the trapping laser could affect the forces acting on the particle. It was verified that the gradient force must exceed the scattering force in order to attain an optical trap. Each of the key components that form an optical trapping system was reviewed from which a successful optical trapping system was built to stably trap micron sized particles in the axial direction and manipulate these particles by movement of the laser beam itself. Furthermore it was observed that a strongly trapped particle remains un-affected by the movement of surrounding particles.

By carrying out various calibration methods, it was demonstrated that it is possible to accurately and precisely determine the strength of the trap. This was achieved by carrying out the drag force, equipartition and power spectrum calibration methods. For the drag force method we obtained a trapping force of (6.12 ± 1.32) pN at 100 mW and (0.93 ± 0.51) pN at 10 mW. The equipartition method measured at 10 mW the trapping force was (1.85± 0.18) pN in the x direction and (1.83 ± 0.18) pN in the y direction while the trapping force at 100 mW was (7.03 ± 1.37) pN in the x direction and (7.22 ± 0.18) pN in the y direction. The power spectrum method made use of the centre of mass algorithm to track the particle to determine the trapping force. At 10 mW power the trap stiffness was determined to be (0.86 ± 0.21) pN while at 100 mW the trap stiffness was (3.64 ± 0.43) pN. It can be concluded that at higher powers one would obtain a stronger trap.

Lastly we considered a novel trap where we introduced a Laguerre-Gaussian beam carrying a topological charge of one into an optical trapping system and were able to rotate a graphite particle with a rotation rate of 0.83 Hz. This proved that orbital angular momentum is easily transferred to a trapped particle.

Overall we showed that novel laser beams can be successfully produced using a spatial light modulator and using an optical trapping and tweezing system can be a useful tool to carry out force measurements and manipulate micron sized particles.

8.2 Future Work: Discovering Avenues in the Field of Microfluidics

As far as future work is concerned, optical trapping and tweezing is a versatile tool that can be incorporated into the emerging field of microfluidics. Microfluidics opens up avenues to carry out research on a microscopic scale instead of in the bulk to investigate flow control analysis for example. This enables one the ability to cut down resources and carry out investigation in the micron scale. An image of a microfluidic channel is represented in Fig. 8.1. Most microfluidic devices (channels) are made up of a material known as PDMS (Polydimethylsiloxane) (Sia & Whitesides, 2003).

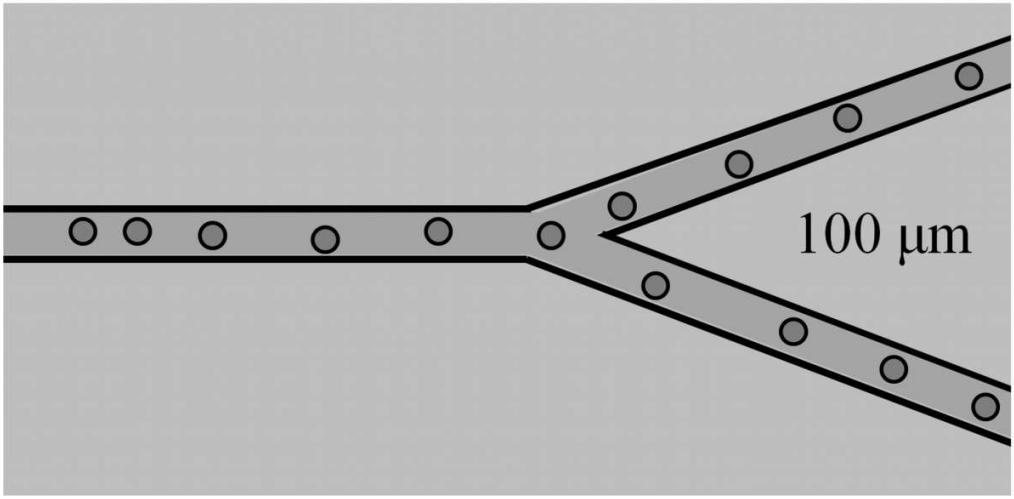

Fig. 8.1 Image illustrating a microfluidic channel with a depth of 100 μm.

Optical trapping proves to be useful in this field since incorporating a spatial light modulator into an optical trapping system allows for the ability to produce an array of optical traps within a microfluidic channel to hold mesoscopic and biological particles which can be addressed independently by chemical reagents in a controlled manner (Eriksson *et al.*, 2007; Merenda *et al.*, 2007, Ozkan *et al.*, 2003; Uhrig *et al.*, 2009). Alternatively using various Laguerre-Gaussian beams which transfer orbital angular momentum to a trapped particle causing it to rotate can influence the mixing of different media within the channel. This will also allow one the ability to measure fluid flow by using the Stokes drag force method (Padgett *et al.*, 2006). An optical trap can also be used to direct particles for optical sorting within a microfluidic channel (Enger *et al.*, 2004; MacDonald *et al.*, 2003, MacDonald *et al.*, 2004; Lin *et al.*, 2008) as illustrated in Fig. 7.2.

This is achieved by trapping a particle as in Fig. 8.2(a) and moving it down the column, Fig. 8.2(b), and thereafter upon reaching the junction releasing the particle from the trap and allowing the fluid flow to push the particle along as indicated in Fig. 8.2(c).

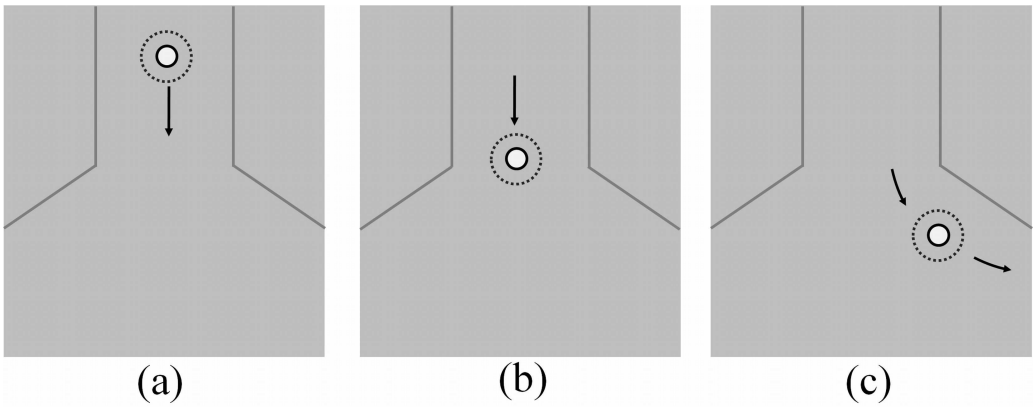

Fig. 8.2 A pair of optical tweezers is a useful tool to sort particles within a microfluidic channel.

Overall optical tweezers incorporated in the field of microfluidic offers a vast number of possibilities that will be beneficial to study. This is all possible using the knowledge gained from beam shaping using optical tweezers as an effective tool for manipulation of micron and nano sized particles.

References

Abbondanzierim E. A., Greenleaf J. W., Shaevitz J. W., Landick R. and Block S. M. 2005. Direct observation of base pair stepping by RNA polymerase. Nature, 438: 460-465.

Allen L., Biejerbergen M.W., Spreeuw R.J.C. and Woerdman J.P. 1992. Orbital angular momentum of light and the transformation of Laguerre Gaussian laser modes. Phys. Rev. A., 15 (11): 8185-8189.

Arlt J. and Dholakia K. 2000. Generation of higher-order Bessel beam by use of an axicon. Opt. Commun. 177, 297-301.

Aruga T. 1997. Generation of long-range nondiffracting narrow light beams, Appl. Opt. 36(16): 3762–3768.

Aruga T., Li W. S., Yoshikado S. Y., Takabe M., Li R., 1999. Nondiffracting narrow light beam with small atmospheric turbulence-influenced propagation. Appl. Opt. 38(15): 3152–3156

Ashkin A. 1970. Acceleration and trapping of particles by radiation pressure. Physical Rev. Lett., 24:156-159.

Ashkin. A. 1992. Forces of a single-beam gradient laser trap on a dielectric sphere in the ray opticxs regime. Journal of Biophysics, 16:569-582.

Ashkin A., Dziedzic J. M., Bjorkholm J. E. and Chu S. 1986. Observation of a single-beam gradient force optical trap for dielectric particles. Opt. Lett., 11(5):288-290.

Aterson L., MacDonald M. P., Sibbett W., Arlt J., Bryant P. E., and Dholakia K., 2001. Controlled Rotation of Optically Trapped Microscopic Particle. Science, 292: 912-914.

Bandres M. A. and Gutierrez-Vega J. C., 2004b. Ince-Gaussian modes of the paraxial wave equation and stable resonators. J. Opt. Soc. Am. A 21: 873-880.

Bandres M. A. and Gutierrez-Vega J. C. 2004. Ince Gaussian beams. Opt. Lett. 29, 144-146.

Barton J. P. and Alexander R. D. 1989. 5th-order corrected electromagnetic field components for a fundamental Gaussian beam. Journal of Appl. Phys., 66:2800-2802.

Barton J. P., Alexander R. D. and Schuab S. A. 1989. Theoretical determination of net radiation force and torque for a spherical particle illuminated by a focused laser beam. Journal of Appl. Phys., 66:4594-4602.

Bazhenov V. Y., Vasnetsov M. V. and Soskin M.S. 1990. Laser modes with screw dislocations in their wave-fronts. JTEP Lett., 52:429-431.

Bazhenov V. Y., Vasnetsov M. V. and Soskin M.S. 1990. Laser modes with screw dislocations in their wave-fronts. JTEP Lett., 52:429-431.

Beijerersbergen M. W., Allen L., van der Veen H, andWoerdman J. P. 1993. Astigmatic laser mode convertors and transfer of orbital angular momentum. Opt. Comm., 96: 123-132.

Beijersbergen M. W., Coerwinkel R. P. C., Kristensen M., and Woerdman J. P., 1994. Helical-wavefrontnext term laser beams produced with a spiral phaseplate. Opt. Commun. 112: 321-327.

Berg-Sorensen K. and Flyvbjerg H. 2004. Power spectrum analysis for optical tweezers. Rev. Sci. Intrum. 75:594-612.

Beth R. A. 1936. Mechanical Detection and Measurement of the Angular Momentum of Light. Phys. Rev., 50:115-125.

Beyli V., Forbes A., Kazak N., Khilo N. and Ropot P. 2010. Bessel-like beams with z-dependent cone angles. Opt. Express, 18(3):1966-1973.

Biggs M., Cabruja E., Forest J. and. Salvi J. 2006. Review of CMOS image sensors. Journal of Microelectronics, 37:433-451.

Block S. M., Blair D. F and Berg H. C. 1989. Compliance of bacterial flagella measured with optical tweezers. Nature, 338:514-518.

Boisset C. G. 1995. Design and Construction of an Active Alignment Demonstrator for a Free-Space Optical Beam Tracking. IEEE Photon Tech. Lett., 7: 676-678.

Bouchal Z., Wagner J. and Chlup M. 1998. Self reconstruction of a nondiffracting distorted beam. Opt. Commun., 151: 207-212.

Bundres M. A. and Gutierrez-Vega J. C. 2004c. Ince Gaussian beams. Opt. Lett., 29(2):144-146.

Clifford M. A., Arlt J., Courtial J., and Dholakia K., 1998. High-order Laguerre–Gaussian laser modes for studies of cold atom. Opt. Commun., 154: 300-306.Czerwinski F., Richarson A. C., and Oddershede L. B. 2009b. Quantifying noise in Optical tweezers by Allan Variance. Opt. Express, 17(15): 255-269.

Davidson M. W. and Fellers T. J. Understanding conjugate planes and Köhler illumination. 1-4.

Davidson N., Friesem A. A. and Hasman E. 1991. Holographic axilens: high resolution and long focal depth. Opt. Lett., 16:523-525.

Dholakia K. and McGloin D. Bessel beam: diffraction in a new light 2005. Contemporary Physics, 46(1):15-28.

Dienerowitz M., Mazilu M. and Dholakia K. 2008. Optical manipulation of nanoparticles: a review. Journal of Nanophotonics, 2: 1-32.

Durnin J., Micelli J.J. and Eberly J.H. 1987. Diffraction free beams. Phys. Rev. Lett., 58: 1499-1501.Galajda P. and Ormos P. 2003. Orientation of flat particles in optical tweezers by linearly polarized light. Opt. Express, 11(5): 446-451.

Enger J., Goksör M., Ramser K., Hagberg P. and Hanstorp D., 2004. Optical tweezers applied to a microfluidic system**.** Lab Chip, **4**: 196–200.

Eriksson E., Scrimgeour J., Enger J. and Goksör M., 2007. Holographic optical tweezers combined with a microfluidic device for exposing cells to fast environmental changes. Proc. of SPIE, 6592: 1-9.

Galvez J. E., 2006. Gaussian beams in optics courses. Am. J. Phys., 74(4): 355-361.
Gelles J., Schnapp B. J. and Sheetz M. P. 1988. Tracking kinesin-driven movements with nanometer-scale precision. Nature, 331:450 -453.

Gibson G. M., Leach J., Keen S., Wright A. J. and Padgett M. 2008. Measuring the accuracy of particle position and force in optical tweezers using high-speed video microscopy. Opt. Express, 16(19): 561-569.

Goncharov A. V., Burvall A. and Dainty C. 2007. Systematic design of an anastigmatic lens axicon. Appl. Opt., 46:6076-6080."

Gori F., Gauttari G. and Padovani C. 1987. Bessel-gauss beams. Opt. Commun., 65(6): 491-495.

Gouesbet G., Maheu B. and Grehan G. 1988. Light scattering from a sphere arbitrarily located in a Gaussian beam, using a Bromwich formulation. Journal of Opt. Soc. of America A5:1427-1443.

Gutierrez-Vega J. C., Iturbe-Castillo M. D. and Chavez-Cerda S. 2000. Alterative formulation for invariant optical fields: Mathieu beams. Opt. Lett., 25, 1493-1495.

He H., Heckenberg N. R., and Rubinsztein-Dunlop H., 1995. Optical particle trapping with higher-order doughnut beams produced using high efficiency computer generated holograms. J. of Mod. Opt., 42: 217-223.

Heckenberg N. R., McDuff R., Smith C. P. and White A. G. 1994. Generation of optical phase singularities by computer-generated holograms. Opt. Lett. 17: 221 – 223-327.

Herman R.M. and Wiggins T.A. 1991. Production and uses of diffractionless beams. J. Opt. Soc. Am. A 8(6):932-942.

Ibenech C. 2008. Torque and optical traps. African Journal of Biotechnology, 7(25): 4663-4666.
Jaroszewicz Z. and Morales J. 1998. Lens axicon: system composed of a diverging aberrated lens and a perfect converging lens. J. Opt. Soc. Am. A 15:2383-2390.

Kennedy S. A., Szabo M. J., Teslow H., Porterfield J. Z. and Abrahams R. I., 2002. Creation of Laguerre-Gaussian laser modes using diffractive optics. Phys. Rev. A.,66:

Khilo N. A., Petrova E.S. and Ryzhevich A.A. 2001. Transformation of the order Bessel beams in unaxial crystals. Quantum Electrons., 31(1):85-89.

Kogelnik H. and Li T., 1966. Laser beams and resonators. Appl. Opt., 5(10): 1550-1567.

Kuga T., Torii Y., Shiokawa N., Hirano T., Shimizu Y., and Sasada H., 1997. Novel optical trap of atoms with a doughnut beam. Phys. Rev. Lett., 78(25): 4713-4716.

Kusumi A., Sako Y., and Yamamoto M. 1993. Confined later diffusion of membrane receptors as studied by single particle tracking (nanovid microscopy).Effects of calcium-induced differentiation in cultured endothelial cells.Biophys. J.,65: 2021-2040.

Lee G. M., Ishihara A., and Jacobson K. A. 1991. Direct observation of Brownian motion of lipids in a membrane. Proc. Nat. Acad. Sci., 88:6274 - 6278.

Lin C., Chen A. And Lin C, 2008. Microfluidic cell counter/sorter utilizing multiple particle tracing technique and optically switching approach. Biomed Microdevices 10:55–63.

Litvin I. A., McLaren M. G. and Forbes A. 2009. A conical wave approach to calculating Bessel–Gauss beam reconstruction after complex obstacles. Opt. Commun. 282: 1078-1082.

MacDonald M. P., Spalding G. C. & Dholakia K., 2003. Microfluidic sorting in an optical lattice. Nature, 426: 421-424.

MacDonald M.P., Neale S., Paterson L., Richies A., Dholakia K., Spalding G.C., 2004. Cell cytometry with a light touch: Sorting microscopic matter with an optical lattice. J. of Bio. Regulators and Homeostatic agents, 7:200-205.

Makynen A., Kostamovaara J. and Myllyla R. 1995. Laser-radar-based three dimensional sensors for teaching robot paths. Opt. Eng., 34: 2596-2602.

Melville H., Milne G.F., Spalding G.C., Sibbett W., Dholakia K. and McGloin D. 2003. Optical trapping of three-dimensional structures using dynamic holograms. Opt. Express, 11(26):3562-3567.Molloy J.E. and Padgett M. J. 2002. Lights, action: optical tweezers. Contemporary Physics, 43(4):241- 258.

Merenda F., RohnerJ., Lamothe E., Pascoal P., Fournier J. M., and Salathé R. P., 2007.Micro-Optics for Optical Trapping in Microfluidics. Proc. of SPIE Vol. 6644:1-10.

Neuman K. C. and Block S. M. 2004. Optical trapping: A review. Rev. Sc. Instr., 75:2787-2809.

Neuman K. C., Abbondanzierim E. A., Landick R., Gelles J.and Block S. M. 2003. Ubiquitous transcriptional pausing is independent of RNA polymerase backtracking. Cell, 115:437-447.

Ozkan M., Wang M., Ozkan C., Flynn R., Birkbeck A., and Esener S., 2003. Optical Manipulation of Objects and Biological Cells in Microfluidic Devices. Biomedical Microdevices 5(1); 61-67.

Padgett M., Leonardo R. D., Leach J., Mushfique H. and Cooper J., 2006. Optical tweezers: an enabling tool for micro-fluidic systems. Proc.of the Symposium on Photonics Tech., 12: 258-216.

Perkins T. T., Li H. W., Dalal R. V., Gelles J. and Block S. M. 2004. Forward and reverse motion of single RecBCD molecules on DNA. Biophysical Journal, 86:1640-1648.

R. N., Ghosh and W. W. Webb 1994. Automated detection and tracking of individual and clustered cell surface low density lipoprotein receptor molecules. Journal of Biophys., 66, 1301-1314.

Rohrbach A. and Stelzer E. H. K. 2002. Trapping forces, force constants, and potential depths for dielectric spheres in the presence of spherical aberrations. Appl. Opt., 14 (13):2494-2507.

Rubinsztein-Dunlop H., Nieminen T. A., Friese M. E. J., and Heckenberg N. R. 1998. Optical trapping of absorbing particles. Advances in Quantum Chemistry 30:469-492.

Saleh B. E. A. and Teich M. C. 1991. Fundamentals of photonics. Chapter 3:80-107.

Schonbrun E., Piestun R., Jordan P., Cooper J., Wulff K. D., Courtial J. and Padgett M. 2005. 3D interferometric optical tweezers using a single spatial light modulator. Opt. Express, 13(10): 3777-3786.

Sogomonian S., Klewitz S. and Herminghaus S. 1997. Self-reconstruction of a Bessel beam in a nonlinear medium. Opt. Commun. 139: 313-319.

Shaevitz J. W., Abbondanzierim E. A., Landick R., Gelles J.and Block S. M. 2003. Backtracking by single RNA polymerase molecules observed at near-base-pair resolution. Nature, 426:684-687.

Sia S. K and Whitesides G. M., 2003. Microfluidic devices fabricated in poly(dimethylsiloxane) for biological studies. Electrophoresis, 24: 3563–3576.

Siegman A. E., 1986. Lasers, University Science Books, Mill Valley,CA: 626-636.

Smith S. P., Bhalotra S. R., Brody A. L., Brown B.L., Boyda E. K. and Prentiss M. 1999. Inexpensive optical tweezers for undergraduate laboratories, Am. J. Phys., 67(1):26-35.

Tempere J., Devreese J. T., and Abraham E. R. I., 2001. Vortices in Bose-Einstein condensates confined in a multiply connected Laguerre-Gaussian optical trap Phys. Rev. A., 64: 1-8.

Toyoda M., Araki K. and Suzuki T. 2002. Measurement and characteristics of a quadrant avalanche photodiode and its application to a laser tracking system. Opt. Eng., 41:145-149.

Truscott A. G., Friese M. E. J., Heckenberg N. R., and Rubinsztein-Dunlop H., 1999. Optically Written Waveguide in an Atomic Vapor. Phys. Rev. Lett. 82: 1438–1441.

Turnbull G. A., Robertson D. A., Smith G. M., Allen L. and Padgett M. J., 1996. The generation of free-space Laguerre-Gaussian modes at millimetre-wave frequencies by use of a spiral phaseplate. Opt. Commun. 127: 183 -188.

Uhrig K., Kurre R., Schmitz C., Curtis J. E., Haraszti T., Clemen A. E.-M and Spatz J. P., 2009. Optical force sensor array in a microfluidic device based on holographic optical tweezers. Lab Chip, 9:661–668.

Vasara A., Turunen J. and Friberg A. T. 1989. Realization of general nondiffracting beams with computer- generated holograms. J. Opt. Soc. Am. A 6(11): 1748-1754.

Woerdemann M., Holtmann F. and Denz C. 2009. Holographic phase contrast for dynamic multiple-beam optical tweezers. J. Opt. A: Pure Appl. Opt., 11:1-11.

Wright E.M., Arlt J. and Dholakia K., 2002. Toroidal optical dipole traps for atomic Bose-Einstein condensates using Laguerre-Gaussian beams. Phys. Rev. A., 63: 013601-8.

Appendix

A1. SLM Calibration Method

A spatial light modulator is a liquid crystal device that is electronically addressed by a circuit board in order to modulate the phase or amplitude of light. The liquid crystal is made up of birefringent molecules arranged in a lattice formation enclosed by two electrodes as seen in Fig. A1. The main characteristic of these crystals is that they are birefringent. They are arranged such that they consist of 1920 by 1080 pixels each having a dimension of 8μm.

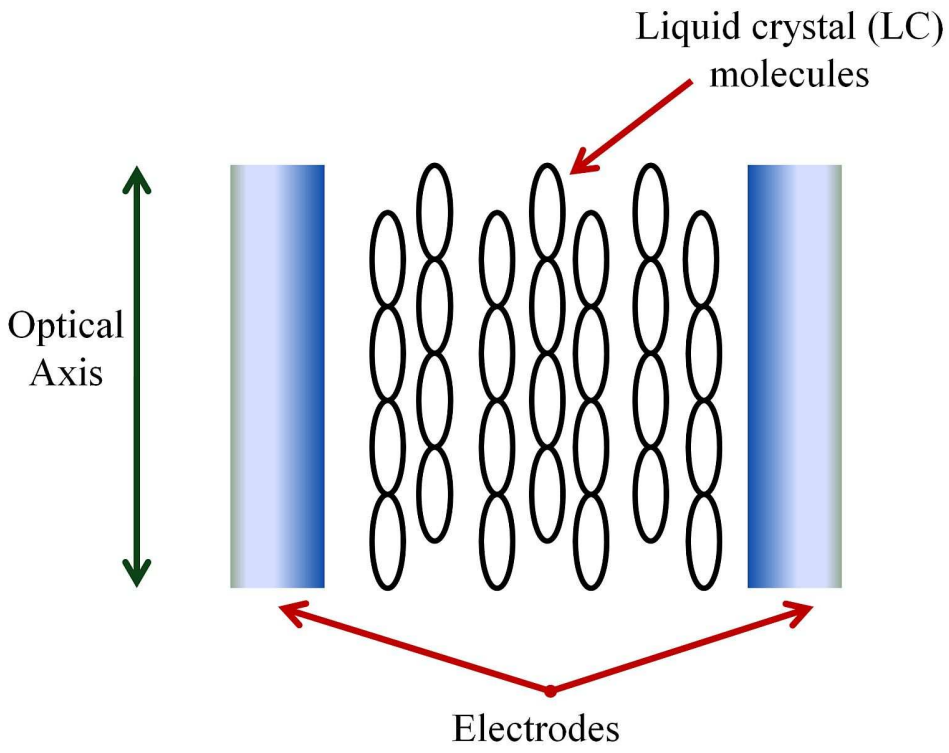

Fig. A1 Illustration of the structure of the liquid display of a spatial light modulator.

When an electric field is applied to the electrodes, the molecules tend to tilt in the direction of the electric field. This brings about a change in the refractive index seen by the light which in turn causes a change in the phase. Keep in mind that the phase is represented by grey-level pattern that is programmed onto the liquid crystal. In order to understand how the phase changes with respect to an applied electric field, we consider two cases which illustrate a 0 and 2 π phase shift. In the case for a zero phase shift there is no applied electric field as observed in Fig. A2(a). The liquid crystal molecules are aligned parallel to the electrodes; however, when a voltage is applied across the electrodes, the molecules will align itself in the direction of the electric field as indicated in Fig. A2(b).

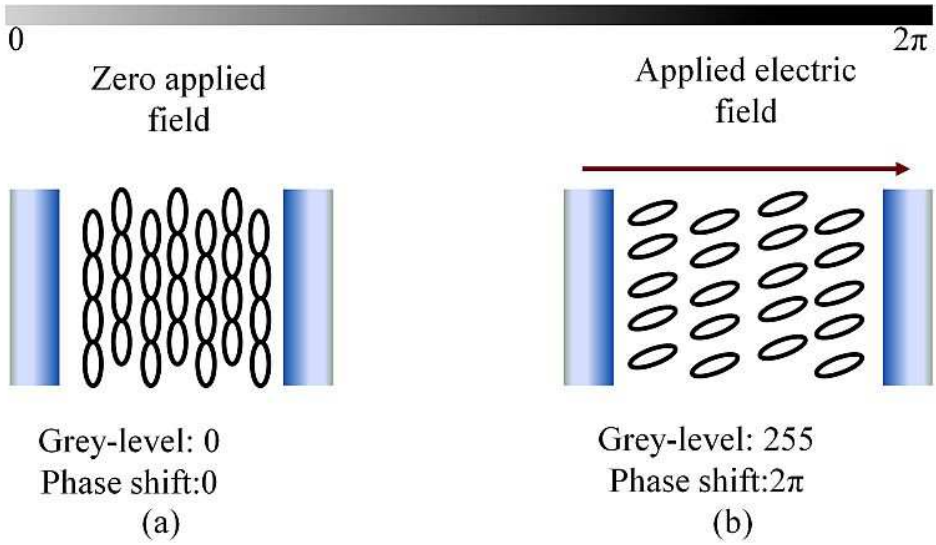

Fig. A2 Illustration of the effects a change in phase has on the liquid crystal.

The phase shift δ is given by

$$\delta = \frac{2\pi}{\lambda}\ell(n_{//} - n_{\perp}), \tag{A1}$$

where δ is the phase shift, ℓ is the path length of the light as it travels through the birefringent medium, $n_{//} - n_{\perp}$ is the change refractive index seen by the light and λ is the wavelength. Since the applied voltage is proportional to the refractive index seen by the light, clearly for a zero applied field the phase shift is zero and noticeably the phase shift is wavelength dependent.

Now if an electric field is applied to the electrodes, the liquid crystal molecules will tend to rotate in the direction of the electric field. This brings about a change in the refractive index as seen by the light and hence a change in the phase shift.

Since the phase shift is wavelength dependent, the SLM has to be calibrated for a specific wavelength in order to ensure an appropriate change in the phase shift from 0 to 2π. For this reason the SLM has to be calibrated prior to being used in any application.

A2 Procedure of Calibration

The SLM is calibrated in order to verify that there is 0 to 2π phase shift over all 256 grey-levels. The first step would be to measure the phase modulation over the entire 256 grey-levels. This is achieved by carrying out the experimental setup represented in Fig. A3. The key components to consider would be that the beam should large enough to illuminate the entire plate as seen in Fig. A4(a) so that the two spots that are reflected on the screen of the SLM have an even distribution of intensity, Fig. A4(b).

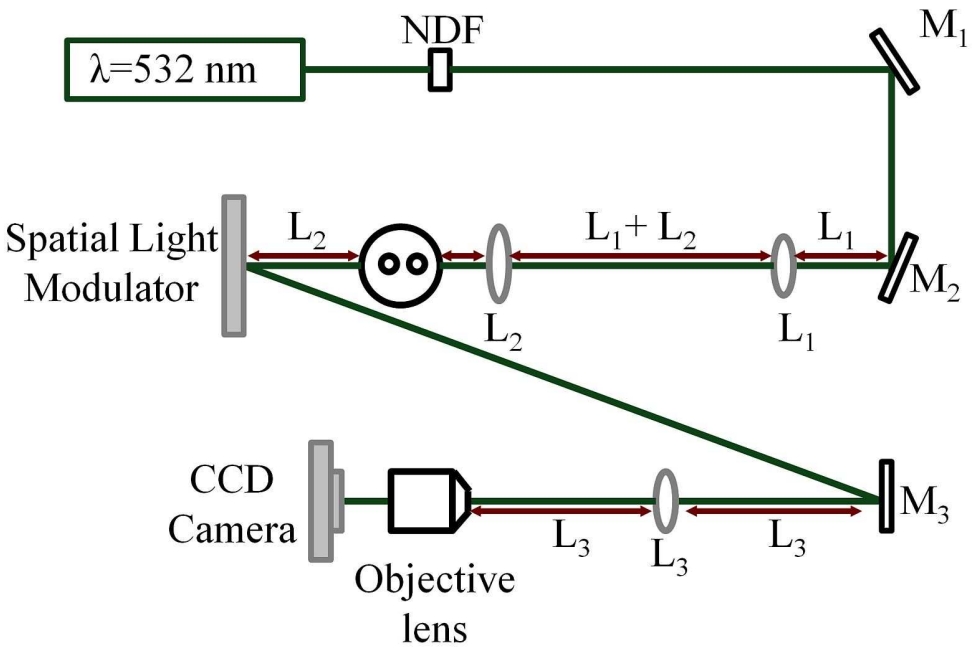

Fig. A3 Optical system used to calibrate an SLM.

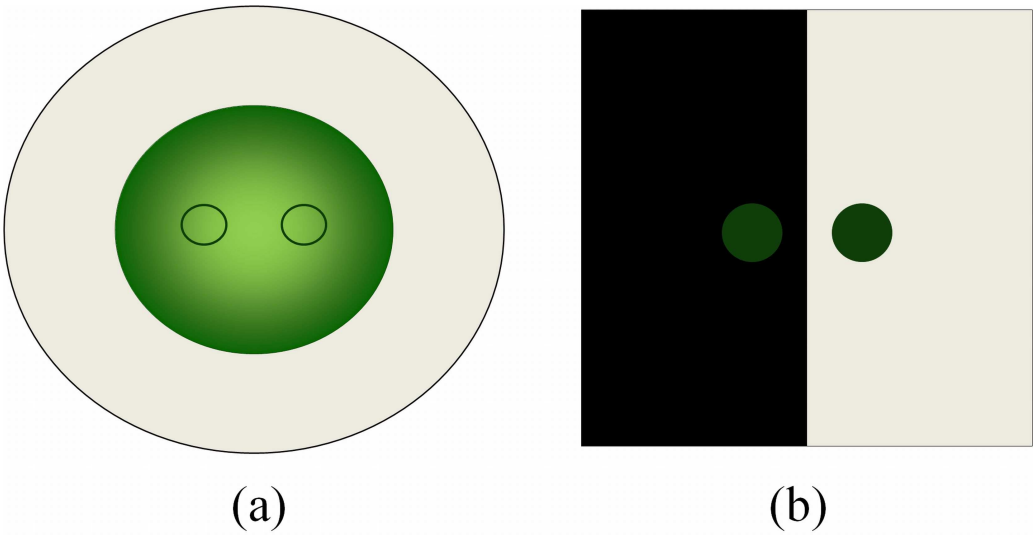

Fig. A4 The following diagram describes the correct illumination required for the calibration of the SLM: (a) the beam has to cover both the spots of the mask and (b) the two spots have to sit evenly on the screen of the SLM as well as there should be an even distribution of intensity.

For this reason beam expanders of focal lengths 15 and 300 mm respectively were used to magnify the beam by a factor of 20 times. A third lens of focal length 200 mm was used to focus the beams onto a 20x objective lens. The purpose of the objective lens was to superimpose both the spots onto each other such that the interference of both beams could be detected. A webcam was used for the detection of the interference pattern presented in Fig. A5.

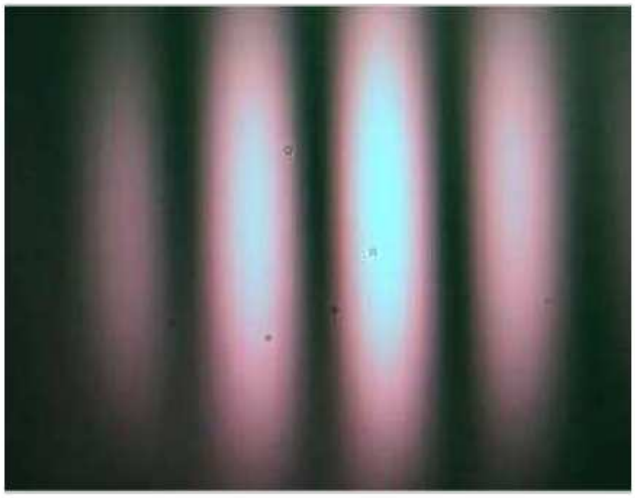

Fig. A5 Interference pattern obtained when both the beams are superimposed on each other.

The interference pattern is scanned horizontally using the software to generate a one dimensional intensity plot of the interference pattern for each grey-level as in Fig. A6. The red dots represent the intensity minima of the intensity pattern for each grey-level.

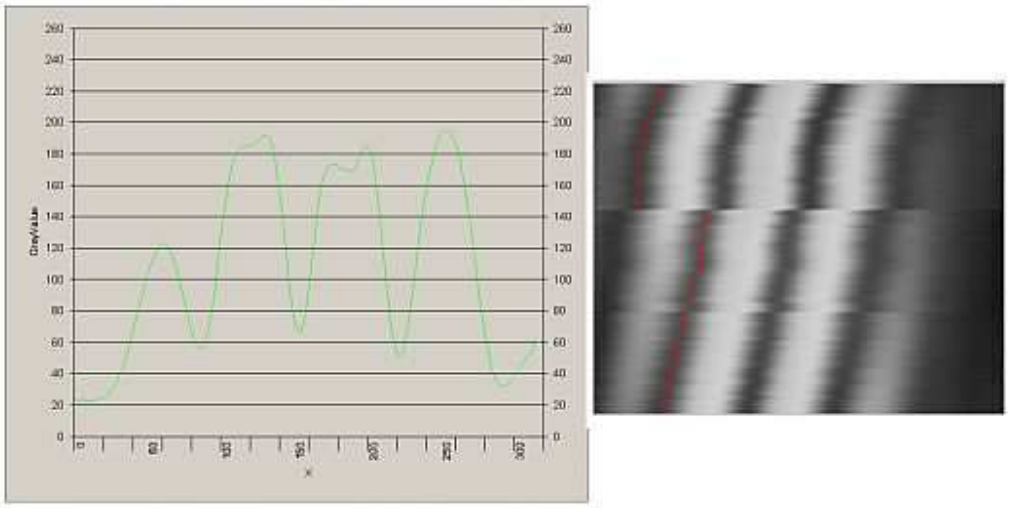

Fig. A6 One dimensional greyscale plot of the interference pattern obtained.

By substituting the appropriate value into the software, it is seen that the grey-level of 255 gives a phase shift of Fig. A7, which shows that the device is not calibrated for this wavelength hence the voltages which address each pixel have to be altered to produce this required 0 to 2π phase shift. Repeating the procedure described will result in the in the appropriate 0 to 2π phase shift shown in Fig. A8.

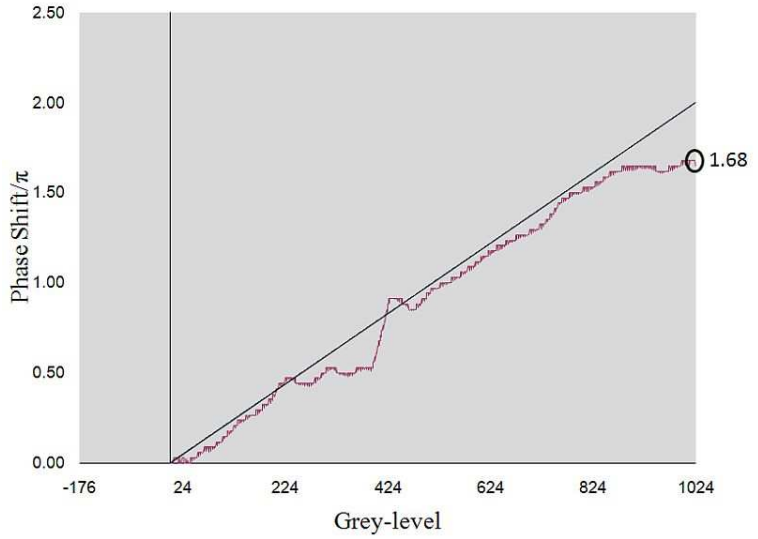

Fig. A7 The measured phase (red) and the desired phase shift (yellow).

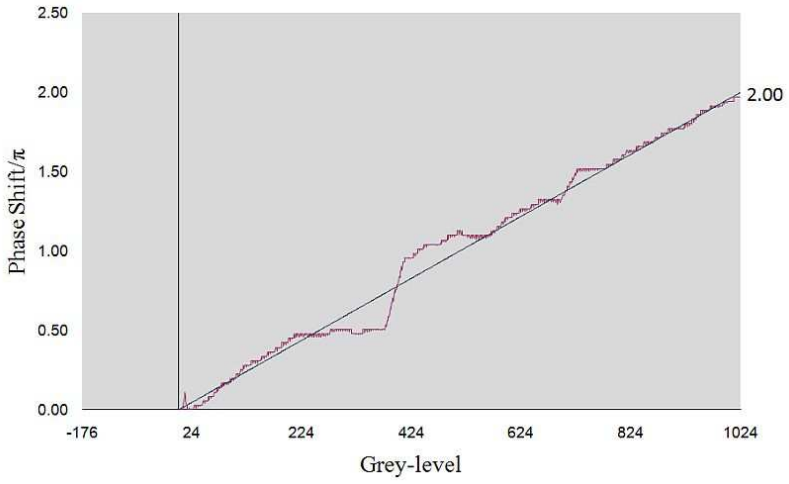

Fig. A8 The measured phase (red) and the desired phase shift (yellow) after the voltages have been adjusted appropriately.

B. Publications

Shape invariant higher-order Bessel beams

Yaseera Ismail[1,2], Vladimir Belyi[3], Gwendolyne Barnes[1], Thandeka Mhlanga[1], and Andrew Forbes[1,2*]

[1] *School of Physics, University of KwaZulu-Natal, Private Bag X54001, Durban 4000, South Africa*
[2] *CSIR National Laser Centre, PO Box 395, Pretoria 0001, South Africa*
[3] *B.I. Stepanov Institute of Physics, NASB, 68 Nezavisimosti ave., 220072 Minsk, Belarus*
** Author e-mail address: aforbes1@csir.co.za*

Abstract:

We present a method to higher-order Bessel beams with z-dependent cone angles. Such fields, if engineered correctly, are shape invariant during propagation and thus do not suffer from a transition from a Bessel-shaped intensity profile in the near field to an annular ring in the far field. We demonstrate the production of such fields in the laboratory with an optical system comprising a combination of two axicons and a lens, allowing for control of the cone angle of the resulting field. While the resulting shape invariant fields are not perfectly non-diffracting, they do maintain many of the some properties of Bessel beams, including self-reconstruction.

Keywords:

Non diffracting, Bessel beams, spatial light modulator, Laguerre-Gaussian beams, Bessel-like beams

1. Introduction

Bessel beams (BBs) have been extensively studied due to their non-diffracting and self reconstructive properties and are one of many solutions to the Helmholtz equation. Durnin et al. [1] outlined a method of producing zero order Bessel beams by illuminating a circular

slit followed by a Fourier transforming lens, and has since been followed by both internal [2,3] and external to the laser cavity [4,5]. One of the most efficient methods to create a zero order Bessel beam external to the laser cavity is to pass a Gaussian beam through a conical lens, or axicon, with the interfering conical waves producing the desired field within a well defined region (dependent on the cone angle of the axicon). Anywhere within this region the Bessel beam is both non-diffracting and self-reconstructing [6]. At the boundary of this non-diffracting region the Bessel beam undergoes an abrupt transformation from a Bessel-shaoed intensity profile (near-field) to an annular-ring-shaped intensity profile (far-field) of the conical field. Replacing the input Gaussian beam with any higher-order Laguerre-Gaussian (LG_{0l}) beam leads to the generation of higher-order Bessel beams [7] with the aforementioned properties. This abrupt change in intensity profile can be considered as a major disadvantage to such beams, for example, in the limited distance over which a particle may be optically trapped [8]. It has been shown that this limited region of validity of the Bessel beam can be overcome by generating Bessel beams with z-dependent cone angles. These beams, so-named Bessel-like beams (BLBs), and have the advantage of retaining their spatial intensity distribution as they propagate from the near- to the far-field: shape-invariant fields. Many techniques have been considered for the generation of BLBs, including introducing spherical aberrations into an optical system [9, 10]. The idea here is to form cone–like propagation in order to obtain a uniform on–axis profile. Alternatively these beams are generated using a defocused Galilean-type telescope in order to introduce negative spherical aberrations into the optical system[11,12] however it was recently shown that it is possible to create such BLBs using an aberration free method [13]. However, the properties are such beams have not been fully explored, nor have the techniques been shown to extend to the generation of higher-order Bessel beams.

In this paper we outline an optical system of a double axicon and a lens that may be used to generate BLBs of any order, and show that the generated beams remain shape invariant during propagation. We show that such BLBs remain self-reconstructing, but exhibit slow diffraction during propagation. The changing scale of the field suggests that the on-axis intensity gradient of such BLBs may be controlled, of relevance to optical trapping and

tweezing, while the encoded vortex is unaltered through the optical system, thus maintaining the orbital angular momentum properties of the field.

2. Generation of Bessel beams (BBs)

Mathematically a Bessel beam is said to exist over an infinite area and carry an infinite amount of power. This holds to be true in theory however this ideal case is not reproducible in the laboratory. In principle we are able to generate a Bessel-Gauss beam where the field is represented as [14]

$$E[r,z] = A\frac{w_o}{w(z)}exp\left[i\left(k-\frac{k_r^2}{2k}\right)z - i\zeta(z)\right]J_0\left[k_r r/(iz/z_R)\right] \times exp\left[\left(\frac{-1}{w^2(z)}+\frac{ik}{2R(z)}\right)\left(r^2+\frac{k_r^2 z^2}{k^2}\right)\right], \quad (1)$$

where A is the amplitude factor, w_0 is the beam waist, k is the wave vector given by $2\pi/\lambda$, k_r is the wave vector in the radial direction defined by $k\sin\theta$, z is the direction while $z_R, w(z)$, $R(z)$ and $\zeta(z)$ are the Rayleigh range, beam width, radius of curvature and Gouy phase shift respectively all of which are expressed as

$$z_R = \frac{\pi w_0^2}{\lambda}, \quad (2)$$

$$w(z) = w_0\sqrt{1+\left(\frac{z}{z_R}\right)^2}, \quad (3)$$

$$R(z) = z\sqrt{1+\left(\frac{z_R}{z}\right)^2}, \quad (4)$$

$$\zeta(z) = \tan^{-1}\left(\frac{z}{z_R}\right). \quad (5)$$

From the definition of Eq. 1, the field at z = 0 may be expressed as

$$E(r,0) = AJ_0(k_r r)\exp\left[-\left(\frac{r}{w_0}\right)^2\right] \tag{6}$$

Furthermore it is possible to produce various higher-orders Bessel beams by merely replacing the starting field by a Laguerre-Gaussian field. The field of a higher-order Bessel beam is represented by

$$E[r,z] = A\frac{w_0}{w(z)}\exp\left[i\left(k - \frac{k_r^2}{2k}\right)z - \zeta(z)\right]J_\ell(k_r r/(iz/z_R))\exp(\pm i\ell\varphi) \times \exp\left[\left(\frac{-1}{w^2(z)} + \frac{ik}{2R(z)}\right)\left(r^2 + \frac{k_r^2 z^2}{k^2}\right)\right], \tag{7}$$

where the order of the topological charge, ℓ ,determines the order of the Bessel beam, φ is the azimuthul phase while the rest of the parameters hold the same definition as expresses previously.

Prior to elaborating on the generation of BLBs, it is instructive to briefly review the generation of conventional BBs of any order. It is well known [15] that illuminating an axicon with a Laguerre-Gaussian beam of zero radial order and azimuthal order *l* results in a BB of order *l*, described by a J_l function. Such an optical set-up is shown schematically in Fig.1.

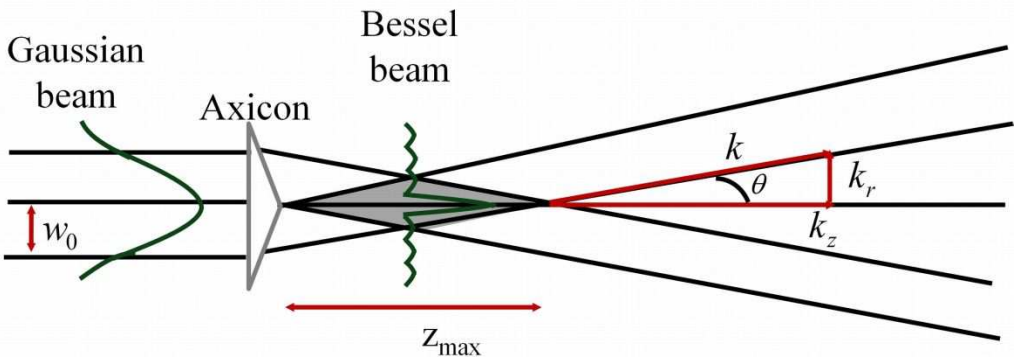

Fig.1. Design to generate a zero-order bessel beam using a single axicon.

We first reproduce the results of [ref] using green laser source (frequency doubled Nd: YAG laser, MG-532C-2000), suitably collimated, and passed through an axicon of cone angle $\gamma = 5^{o}$. The results are as expected: the $l = 0$ Laguerre-Gaussian beam (Gaussian) is transformed into a BB of order $l = 0$ (J_l) with a Bessel profile in the region defined by z_{max} and an annular ring outside this region. Comparison of theory and experiment is shown in Fig. 2.

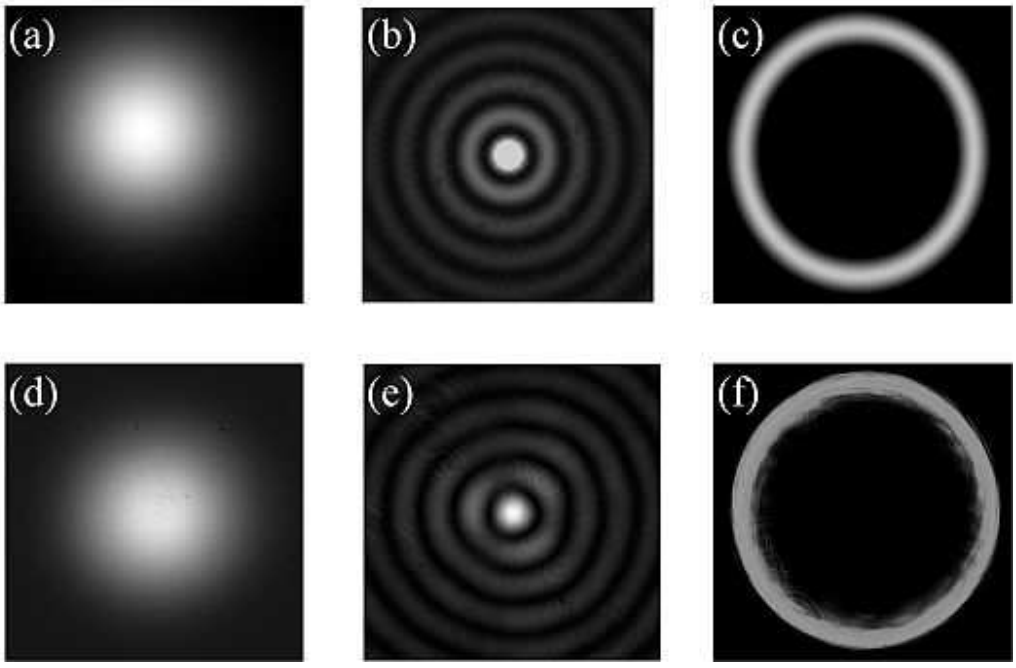

Fig.2. Theoretical and experimental images of the generation of a Bessel beam using a single axicon: (a) is an image of a theoretical Gaussian beam followed by the corresponding experimental image (b). (c) and (d) are theoretical and experimental images respectively of the near-field intensity profile of a bessel beam. As observed the intensity is greatest at the central position followed by concentric rings. The far-field intensity profile is a conical field depicted by a annular ring whereby (e) is the theoretical image of field while (f) is the experimental observation.

By replacing the input Gaussian beam by a Laguerre-Gaussian beam of azimuthal order l (LG_l) it is possible to produce higher-order Bessel beams (BB_l) [15]. Laguerre Gaussian beams belongs to a family of beam's that carry orbital angular momentum [16]. The orbital

angular momentum carried by a Laguerre Gaussian beam is dependent upon the order of the topological charge it carries and since it is the azimuthul phase term that leads to the amount of orbital angular momentum carried by the beam, the higher the topological charge, the greater the amount of orbital angular momentum carried by the beam. There are many ways to generate a LG_l beam; we opt here to create the azimuthal phase variation using a grey-scale digital hologram programmed onto a phase-only spatial light modulator (SLM), as illustrated in Fig. 3. The input Gaussian beam (a) was directed onto a SLM (Holoeye Pluto, 1080 x 1920 pixels) programmed with an appropriate grey scale phase pattern (b) in order to increase the azimuthal index of the field from 0 to *l*.

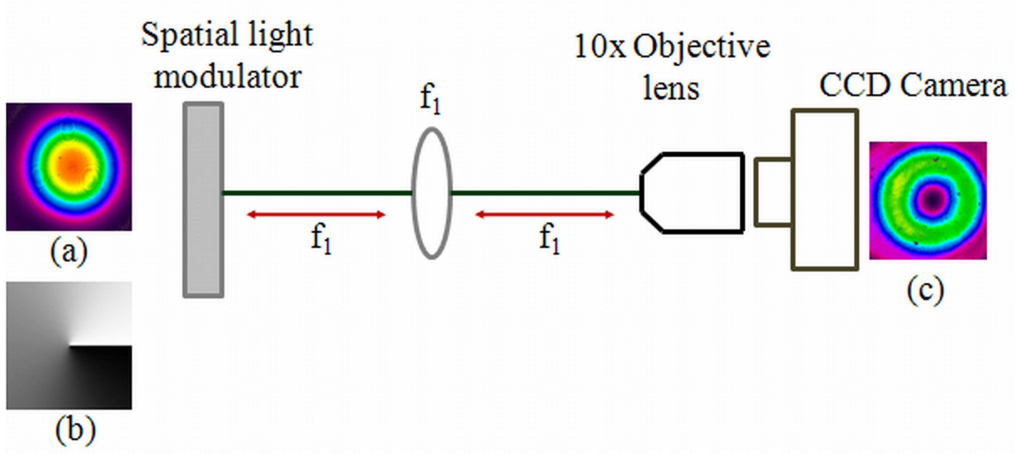

Fig.3. Optical system to generate various orders Laguerre-Gaussian beams consisting of a spatial light modulator used to manipulate the phase of the incoming beam accordingly followed be a single lens of focal length 100mm that relayed the plane at which the beam was imaged which was captured by a Scorpion IEEE 1394 CCD camera (model SCOR-20S0). A 10x objective lens was used to magnify the beam onto the camera.

This procedure was carried out for various orders of *l* by appropriate choice of hologram. The experimental results obtained are represented in Fig. 4, showing that the vortex of the input beam could be adequately controlled.

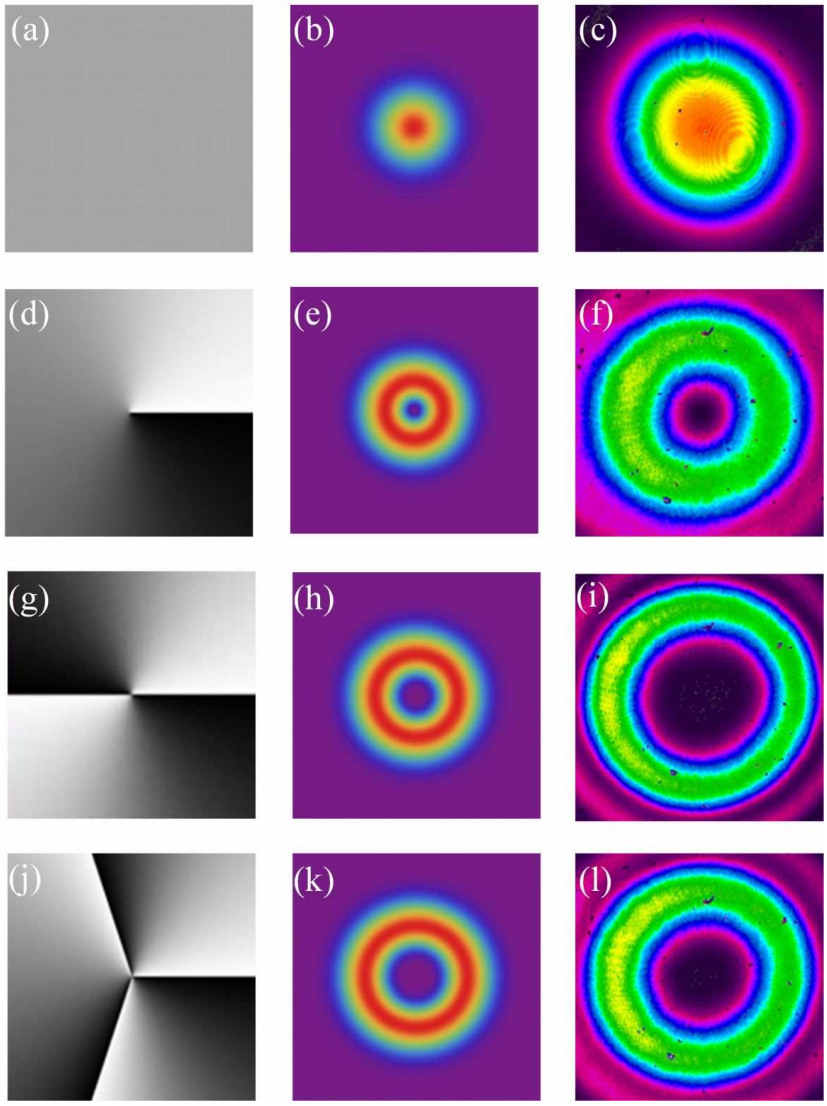

Fig.4. Experimental images of the generation of various orders Laguerre-Gaussian beam using a SLM. When a uniform grey scale pattern was addressed to the screen of the SLM (a), the phase of the beam remained unaltered hence theoretical (b) and experimentally (c) we generated a Gaussian beam. However by changing the grey scale pattern to modulate from black to white (d) once such that the phase of the beam is said to be altered from 0 to 2π once we obtained a first order Laguerre-Gaussian beam both theoretically (e) and experimentally (f). Higher-order Laguerre-Gaussian beams were generated by increasing the number of times the phase varied from 0 to 2π by changing the grey scale pattern accordingly.

In order to produce high-order BBs, the generated LG_l beams were propagated through the optical scheme illustrated in Fig.1. As with the zero-order Bessel beams, higher-order Bessel beams exist for a finite propagation distance and have an annular ring as the far-field intensity profile. The results are shown in Fig. 5, and are consistent with those found by others [14].

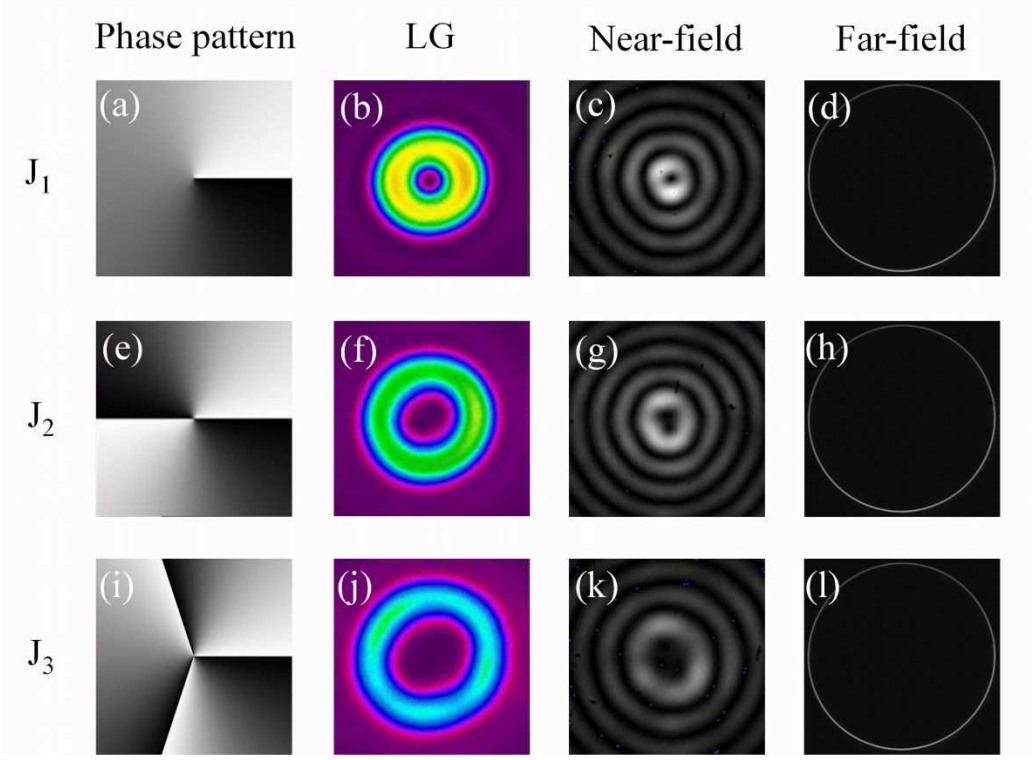

Fig.5. Experimental images of the various higher-order Bessel beams.

A BB_l beam carrying a topological charge of one, as seen in Fig. 7(c), has a central zero in intensity associated with the vortex of the beam. As the order of the vortex increases so does the region of the central null intensity, and likewise for negative topological charge. The far-field intensity profile in all cases was an annular ring.

Having reviewed the known generation of zero and higher-order Bessel beams, which exist for a finite propagation distance, we now turn our attention to the subject of this paper: the generation of shape invariant Bessel beams.

3. Generation of Bessel-like beams (BLBs)

Thus far a single axicon was used to generate Bessel beams of any order, with the Bessel beam existing over a finite propagation distance. The scheme illustrated in Fig. 6 consists of two axicons and a single lens which will be used to overcome this abrupt change in intensity profile from the near- to the far-field. When a Gaussian beam is passed through the lens and the first axicon an annular ring is produced at a distance *f* after the lens (the Fourier transform of the Bessel field produced by the first axicon alone). This annular ring is thereafter illuminated onto the second axicon. It has been shown that this system results in a Bessel beam with a cone angle that changes with propagation distance, tending to zero in the limit of very large z [13]. A consequence of this is that the radial profile of the field remains Bessel-like in shape during propagation from the near- to the far-field.

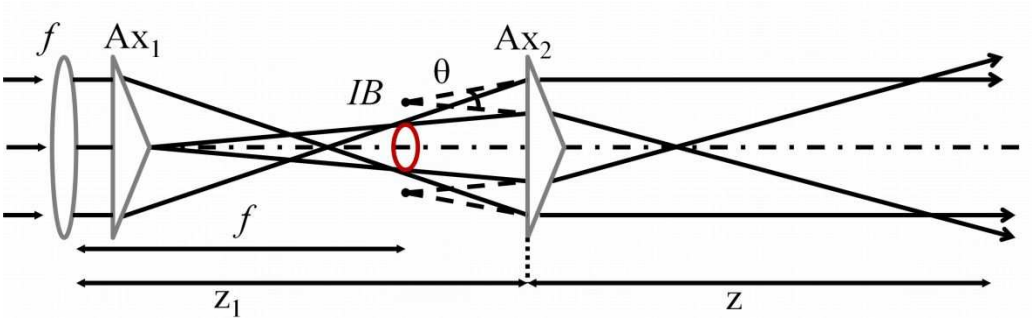

Fig.6. Optical scheme used to generate Bessel-like beams with z-dependent cone angles [13].

Experimental observation of the generation of a zero-order Bessel-like beam is illustrated in Fig. 7. When the system was illuminated by a Gaussian beam as seen in Fig. 7(a) a zero-order Bessel-like beam was produced in the near field as illustrated in Fig. 7(b), while after propagating a distance far greater than z_{max} (124.25 mm) the field remains shape invariant (Fig. 7(c)). Such a field has several useful properties, including the capability to have a higher concentration of energy in the core of the beam as opposed to the conventional non-diffracting beams [11, 12].

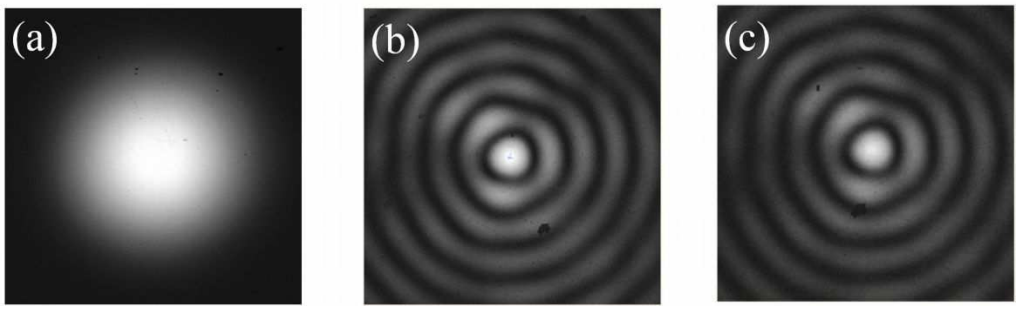

Fig.7. Experimental images of the generation of a zero-order Bessel-like beam in the near- and far-field.

We now combine the results of the previous section, with the concept in this section, to produce shape invariant BLBs for the first time. In order to incorporate the scheme in Fig. 6 into an experimental setup, a frequency doubled Nd: YAG laser (λ = 532 nm) was directed onto a phase-only SLM (HoloEye PLUTO VIS SLM with 1920×1080 pixels and calibrated for a 2π phase shift at λ = 532 nm). The SLM was used to vary the beam illuminating the axicon. By means of changing the phase pattern depicted on the screen of the SLM, the phase of the initial beam was modulated accordingly. Thereafter the respective beam was passed illuminated onto the first axicon followed by a Fourier lens of focal length 40 mm and thereafter passed through the second axicons. Both axicons were placed a distance 75mm apart. The images were captured on a Scorpion IEEE 1394 CCD camera (model SCOR-20S0). The following setup as constructed in the laboratory is shown in Fig. 8

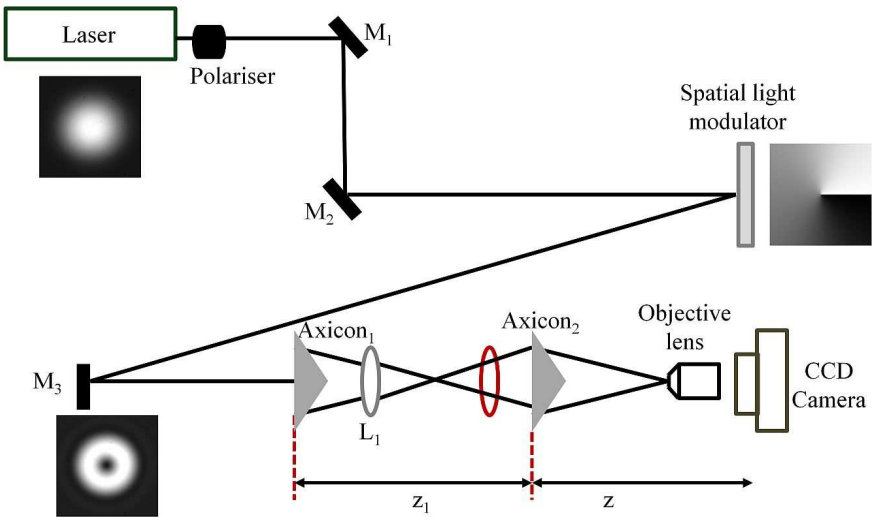

Fig.8. Experimental setup to generate z-dependent Bessel-like beams where an SLM (HoloEye PLUTO VIS) was used to modulate the phase of the beam that was passed through the double axicon system which consisted of a Fourier lens L_1 with a focal length of 40 mm and 4x objective lens was used to magnify the beam onto the camera.

By traversing through the optical system such that a Gaussian beam as seen in Fig. 9(a) was directed onto the SLM containing a grey scale phase pattern that modulated the phase of the incoming beam from 0 to 2π once which produced a first order Laguerre-Gaussian as represented in Fig. 9(b). It is apparent that the Laguerre-Gaussian beam had central zero intensity since it contained a central dark hole. This beam was thereafter illuminated onto the first axicon and a Bessel beam was generated. Thereafter using a lens with a focal length of 40 mm the Bessel beam was Fourier transformed to form an annular ring. This annular ring was thereafter passed through the second axicon such that a Bessel-like beam was produced (near-field intensity profile) that contained central zero intensity surrounded by concentric rings as represented in Fig. 9(c). By Fourier transforming this BLB we observed that in the far-field the beam retains is shape as observed in Fig. 9(d).

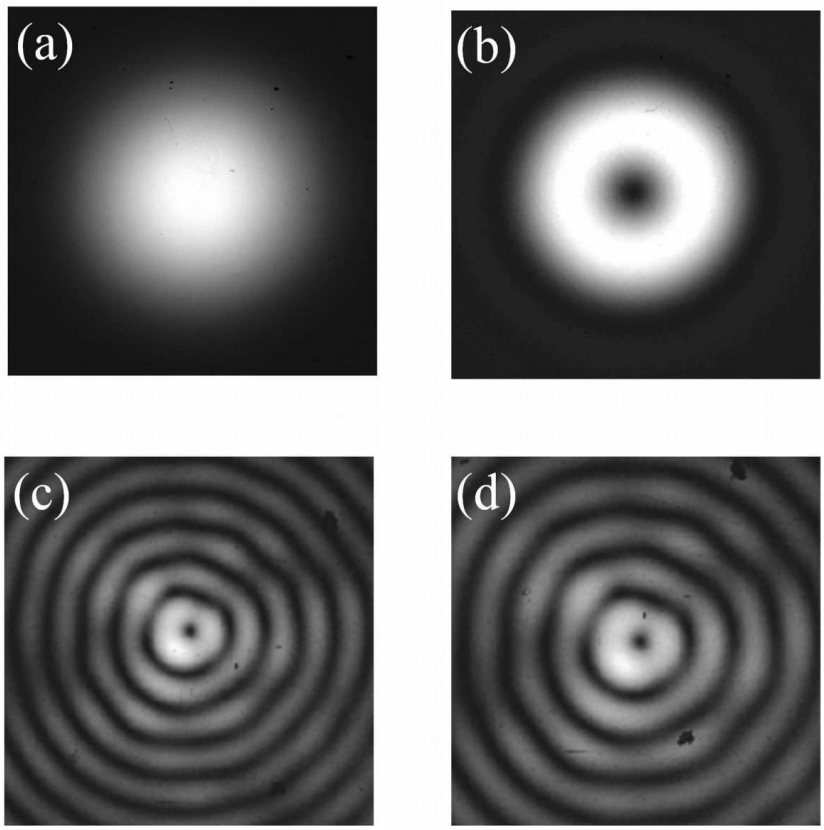

Fig.9. Experimental images of the generation of a higher-order Bessel-like beam carrying a topological charge of one in the near- and far-field.

This procedure was carried out for various order Bessel-like beams by passing a Laguerre-Gaussian beam (Gaussian) through the double axicon and lens system and a summary of the results obtained are represented in Fig. 10.

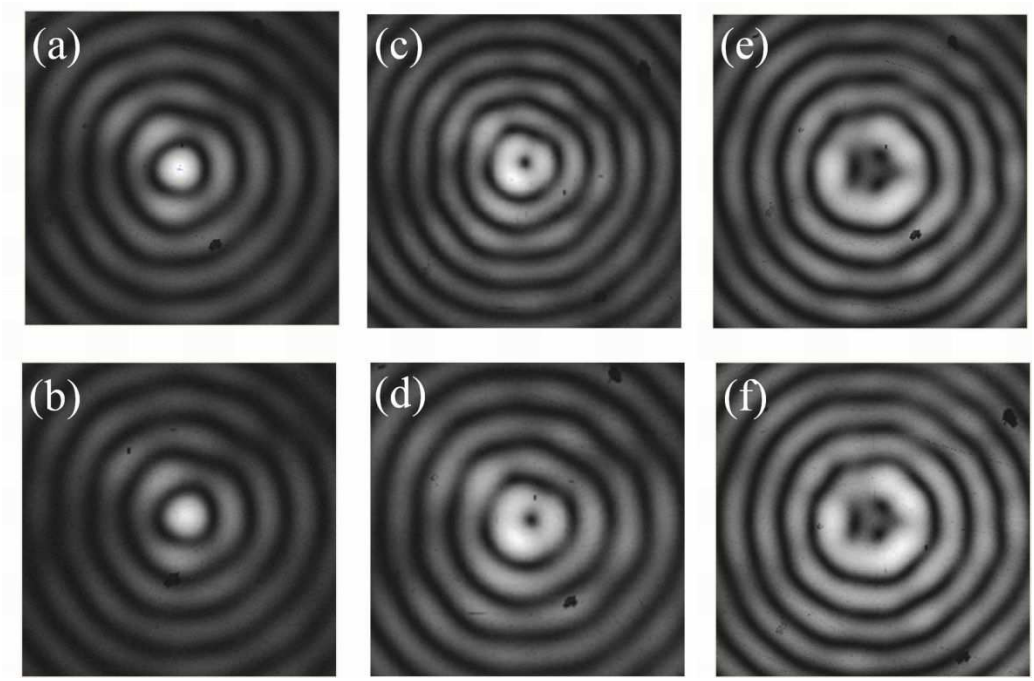

Fig.10. Summary of the experimental observation of z-dependent Bessel-like beams.

The self reconstruction properties of Bessel beams have been extensively studied over the years [17, 18]: it is now understood that if an obstruction is placed within the validity region of a Bessel beam it will self-reconstruct after some distance defined as the shadow region measured by $D / 2\tan((n-1)\gamma)$ where D is the diameter of the obstruction, n is the refractive index of the axicon and γ is the cone angle of the axicon [19]. Furthermore we note that if the obstruction is placed off the optical axis then the conventional non-diffracting Bessel beam will only partially self-reconstruct. Here we show that BLBs also exhibit this characteristic. To illustrate that these beams also possess the ability to self-reconstruct upon encountering an obstruction a ball bearing of diameter 0.12 ± 0.001 mm was placed in the path of a first order BLB as shown in Fig. 11. The Bessel-like beam before reconstruction is represented in Fig. 11(a). Upon placing the ball bearing 200 mm away from the second axicon we observed that the central region of the beam was overshadowed by the obstacle as seen in Fig. 11(b) however the outer rings of the beam are still seen. Taking into account the diameter of the obstruction the shadow region was

calculated to be 239.08 mm after the obstruction. By placing the camera on a rail we were able to image the beam at various positions after the obstruction to determine the distance at which self reconstruction occurs. We noticed that approximately 250 mm from the obstruction the beam started to reconstruct and at a distance 525 mm from the obstruction we noticed a complete reconstruction of the beam as illustrated in Fig. 11(c). Since the BLBs are not confined to distances $z < z_{max}$, the axial position at which the obstruction has to be placed is not a limiting factor. More particularly since BLBs retain their spatial distribution as they propagate there is a continuous interference of light rays throughout the optical axis. Due to this an obstruction placed outside the z_{max} region or even off the optical axis will still result in a successful reconstruction of the beam. In our case the obstruction was placed approximately 75.6 mm outside the z_{max} region and noticeably we obtained a well reconstructed BLB.

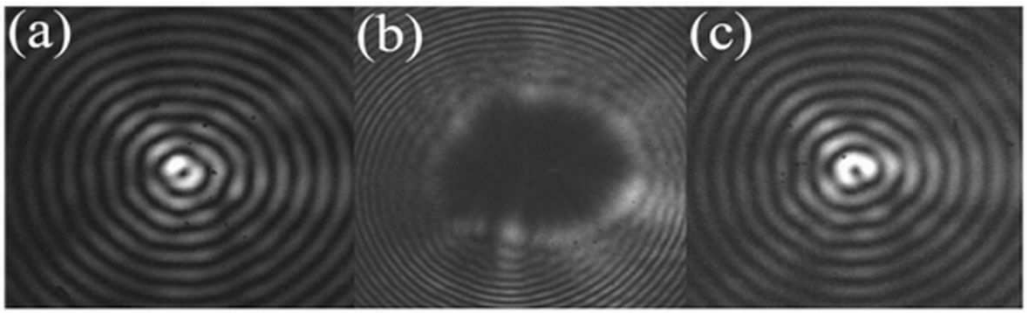

Fig.11. Self reconstruction of a Bessel-like beam carrying a topological charge of one: (a) the beam before encountering an obstruction; (b) overshadowing of the beam due to the obstruction being placed in its path and (c) the Bessel-like beam has undergone a complete self-reconstruction.

Finally we remark on the free-space propagation of such fields. While we have shown them to be shape invariant, they are no longer non-diffracting. We measured the diffraction of the various order BLBs by placing the camera on a rail and thereafter imaged the beam at a range of positions along the axis of propagation in increments of 100 mm intervals. The central region of the beams was measured and the results obtained are illustrated in Fig. 12. We observed that in all cases there was a linear increase in the width of the central region

as the propagation distance was increased. This effects was influenced by the order of the BLB such that the higher the order the greater the diffraction.

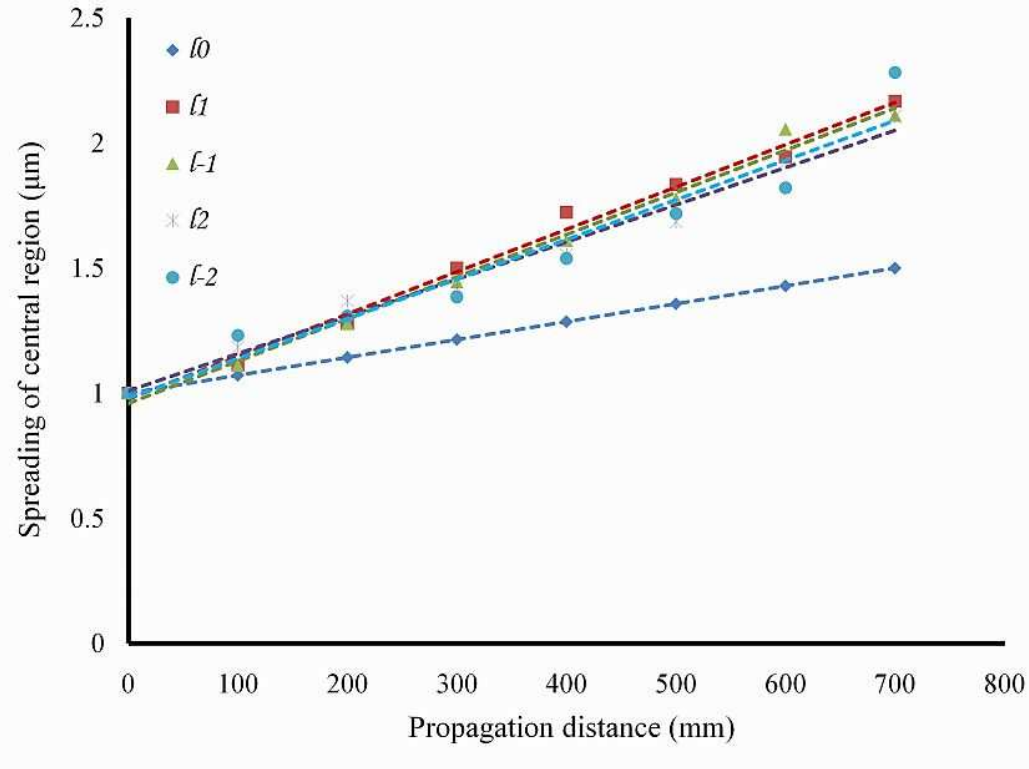

Fig.12. Graph illustrating an increase in divergence of various orders Bessel-like beams as they propagate from the near- to the far-field.

To further illustrate this increase in diffraction, Fig. 13 and 14 represents intensity profiles of a zero- and a higher-order Bessel-like beam (with a topological charge of one) at over a distance of a 1000 mm. Furthermore we measured the central region of the zero-order BLB in Fig.13 (frame a) to be approximately 13 μm which compared to frame (t) where the central region was measured to be 25 μm concludes that these BLBs slightly diffract as they propagate. This confirms that there is change in the size of the beam which is noticeable when comparing each of the frames in both figures.

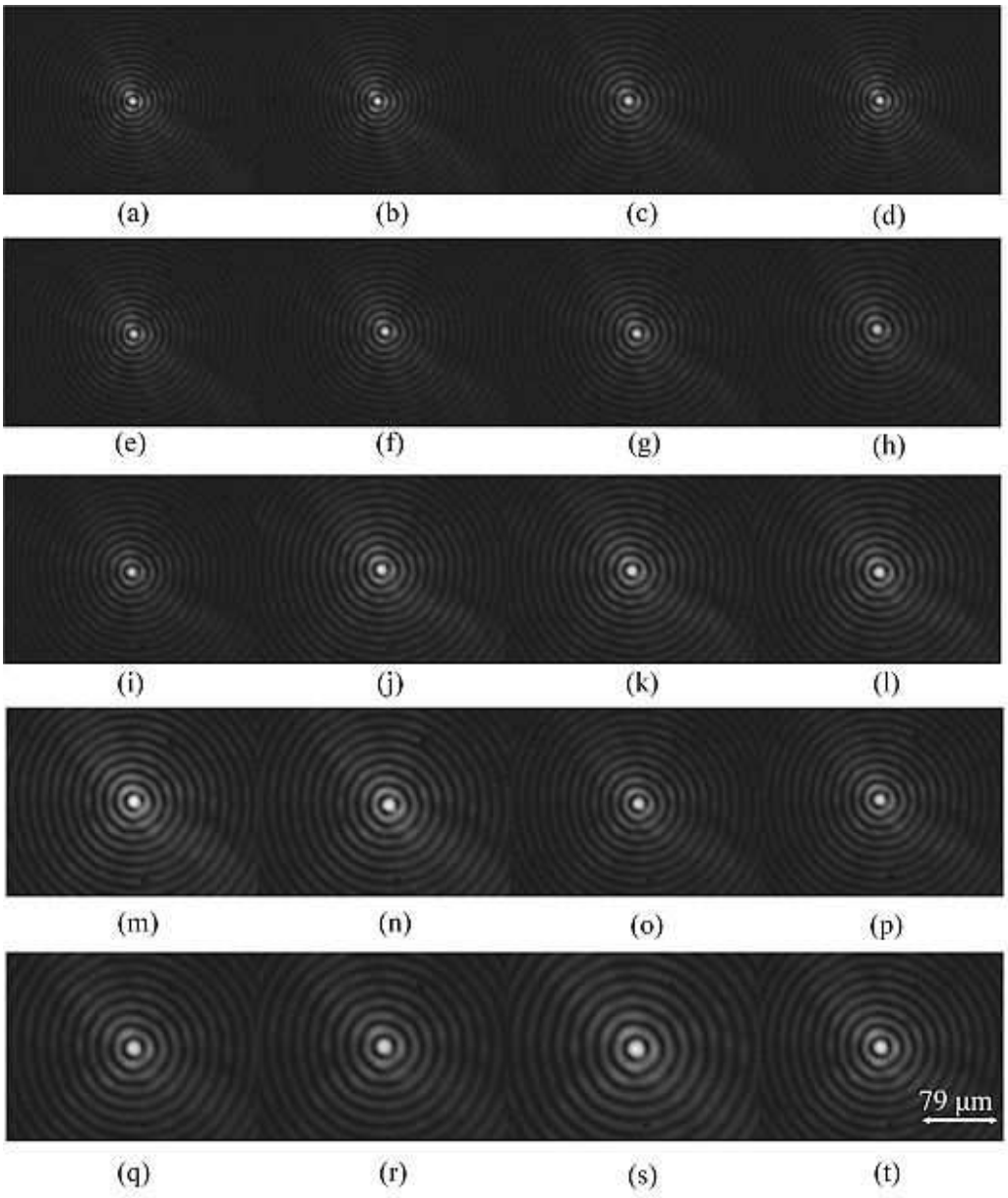

Fig.13. Images of a zero-order Bessel-like beam retaining its spatial distribution as it propagates from the near- to the far-field.

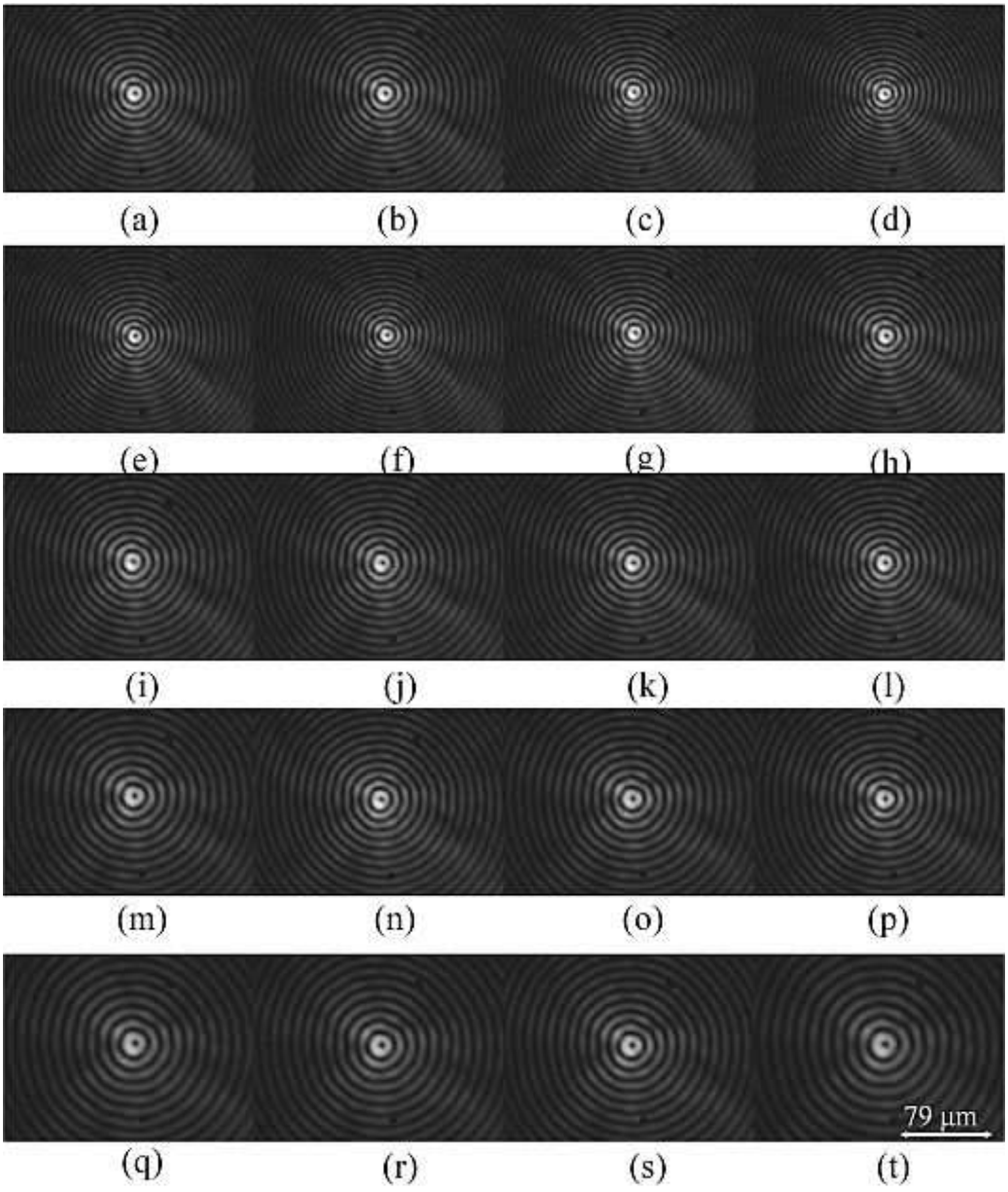

Fig.14. Images of a higher-order Bessel-like beam carrying a topological charge of one retaining its spatial distribution as it propagates from the near- to the far-field.

4. Conclusion

We have verified previously reported results on the generation of Bessel beams of zero and higher-order, and exploited these techniques for the demonstration of shape invariant higher-order Bessel-like beams. These beams were shown to have similar near- and far-field intensity profiles, albeit with a scale factor difference, indicating the reduction in the non-diffracting nature of such fields as compared to ideal Bessel beams. Although they are not perfectly non-diffracting, such fields have an on-axis intensity gradient in the direction of propagation which can be useful in certain applications, for example, in optical trapping for accelerating trapped particles along the Bessel column.

5. References

[1]J. Durnin, J.J.Micelli, J.H. Eberly, Physics Review Letters, 58 (1987) 1499-1501
[2]J. Rogel-Salazar, G.H.C. New, S. Chavez-Cerda, Opt. Communs. 190(2001) 117-122
[3]A. N. Khilo, E. G. Katranji, A. A. Ryzhevich, J. Opt. Soc. Am. A 18(2001) 1986-1992
[4]A. Vasara, J. Turunen, A. T. Friberg, J. Opt. Soc. Am. A 6(11) (1989) 1748-1754
[5] R.M. Herman, T.A. Wiggins, J. Opt. Soc. Am. A 8(1991) 932-942
[6]Z. Bouchal, J. Wagner, M. Chlup, Opt. Commun. 151 (1998) 207-212
[7]J. Arlt, K. Dholakia, Opt. Commun. 177 (2000) 297-301
[8]J. Arlt, V. Garces-Chavez, W. Sibbett, K. Dholakia, Opt. Commun. 197 (2001) 239-245
[9]N. Davidson, A. A. Friesem, E. Hasman, Opt. Lett. 16 (1991) 523-525
[10]Z. Jaroszewicz , J. Morales, J. Opt. Soc. Am. A 15 (1998) 2383-2390
[11]T. Aruga, Appl. Opt. 36(16) (1997)3762–3768
[12]T. Aruga, S. W. Li, S. Y. Yoshikado, M. Takabe, R. Li, Appl. Opt. 38(15) (1999)3152–3156
[13]V. Belyi, A. Forbes, N. Kazak, N.Khilo, P. Ropot, Opt. Express. 18 (2010)1966-1973
[14]F. Gori, G. Gauttari ,C. Padovani, Opt. Commun. 65(6) (1987) 491-495
[15]J. Arlt, K. Dholakia, Opt. Commun. 177 (2000) 297–301
[16]L. Allen, M. W. Beijersbergen, R. J. C. Spreeuw , J. P. Woerdman, Phys. Rev. A 45 (1992)8185–8189

[17]Z. Bouchal, J. Wagner, M. Chlup, Opt. Commun., 151 (1998) 207-212.

[18]S. Sogomonian, S. Klewitz, S. Herminghaus, Opt. Commun. 139 (1997) 313-319

[19] I. A. Litvin, M. G. McLaren, A. Forbes. Opt. Commun. 282 (2009) 1078-1082

Higher-order Bessel like beams with z-dependent cone angles

Y.Ismail[a,b], G Barnes[b], T Mhlanga[b], V. Belyi[d], A. Forbes[a,b†]
[a]CSIR National Laser Centre, Box 395, Pretoria 0001, South Africa
[b]School of Physics, University of KwaZulu-Natal, Private Bag X54001, Durban 4000, South Africa
[d]B.I. Stepanov Institute of Physics, NASB, 68 Nezavisimosti ave., 220072 Minsk, Belarus

ABSTRACT

As in the case of zero-order Bessel beam being produced by illuminating an axicon with a Gaussian beam, higher-order Bessel beams are generated by substituting the Gaussian beam with a Laguerre Gaussian (LG) beam. These beams hold similar properties to zero-order Bessel beams except they carry orbital angular momentum (OAM). They also undergo an abrupt spatial transformation at the boundary of their non-diffracting regime whereby the near-field intensity distribution is a Bessel function which transforms into an annular ring (far-field profile). This can be considered a disadvantage to such beams in comparison to a Gaussian beam that is propagation invariant. By using a double axicon lens system this Bessel beams with z-dependent cone angles can be produced however at the expense of its non-diffracting nature. Here we outline an optical design to produce higher-order Bessel-like beams with z-dependent cone angles that will retains its spatial distribution as $z \rightarrow \infty$.

Keywords: Higher-order Bessel beam, Laguerre Gaussian beams, axicon

1. INTRODUCTION

Since the inception of zero-order Bessel beams being the simplest solution to the one dimensional Helmholtz equation introduced by Durnin in 1987, researchers of the photonics community has extensively studied the subject further. Over the years a few techniques have been proposed to generate these beams experimentally. One of the most well known method introduced by Durnin himself, is the annulus method whereby a lens and ring slit aperture is used to produce such beams [1].

Other methods include using a conical lens known as an axicon [2, 3]. This is the most efficient method since there is almost a hundred percent transmission of the initial beam intensity that produces the Bessel beam. A more advance method is using holography which involves the use of diffractive optical elements. Recently the development of spatial light modulators has lead to generation of not only Bessel beam but numerous other novel beams as well [4].

The interesting characteristic of Bessel beams are that they non-diffracting as well as self-reconstructive within their validity region [3]. They downfall is that they exist for a finite distance hence outside their boundary region a Bessel function undergoes a spatial transformation and forms a conical field.

Here we will demonstrate the generation of zero- and higher-order Bessel beams using a conical lens. We will also outline a method that overcomes the limitation of propagation distance hence instead of obtaining an annular ring in the far-field the Bessel beam will retain its spatial spectrum to form a Bessel beam in the far-field as well [5].

2. GENERATION OF BESSEL BEAMS USING A SINGLE CONICAL LENS

Mathematically Bessel beams exists over an infinite area carrying an infinite amount of power. This ideal case however is not reproducible experimentally. As mentioned previously there are a few techniques to demonstrate the existence of Bessel beams however due to its efficiency an axicon is chosen to demonstrate the generation of these beams as illustrated in Fig. 1.

† Corresponding author: Andrew Forbes; tel: +27 12 841 2368; fax: +27 12 841 3152; email: aforbes1@csir.co.za

Laser Beam Shaping XI, edited by Andrew Forbes, Todd E. Lizotte, Proc. of SPIE Vol. 7789, 77890C · © 2010 SPIE · CCC code: 0277-786X/10/$18 · doi: 10.1117/12.863345

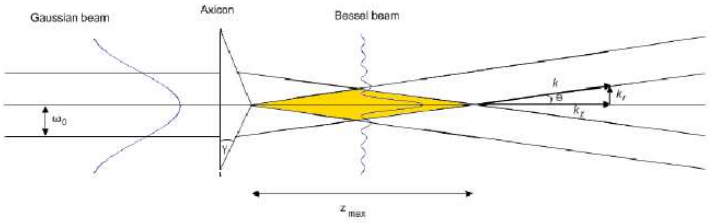

Figure 1: Schematic of the optical design to demonstrate the existence of Bessel beams using an axicon lens.

An axicon lens with a cone angle of 5^0 is illuminated by a Gaussian beam. Since an axicon is a conical lens, the light rays propagate along a cone to form a diamond shaped region in which interference occurs and hence a Bessel beam is produced. Unlike a Gaussian beam which are propagation invariant, Bessel beams exist for a finite region which is inversely proportional to the divergence defined by (1),

$$z_{\max} = \frac{k}{k_r}\omega_0 \approx \frac{\omega_0}{\theta} \tag{1}$$

where wo is the beam radius and θ is the divergence defined by Eq.(2)

$$\theta = (n-1)\gamma \tag{2}$$

Eq. 2 confirm that Bessel beams are non-diffracting within its validity region however at the boundary they undergo a transformation from a Bessel function (near-field profile) to a conical field characterized as an annular ring intensity distribution (far-field profile). The above optical design was incorporated into an experimental setup whereby the theoretical as well as experimental results are depicted in Fig. 2. As observed there is a good agreement between the theoretical and experimental results obtained.

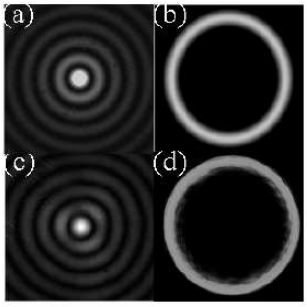

Fig.2: Theoretical as well experimental generation of zero-order Bessel beam: (a) theoretical image of zero-order Bessel beam (near-field profile), (b) theoretical image of the zero-order Bessel beam (far-field profile), (c) experimental image of a zero-order Bessel beam (near-field profile) and (d) experimental image of a zero-order Bessel beam (far-field profile).

Taking this a step further and illuminating the axicon lens with higher-order Laguerre Gaussian (LG) beams instead of a Gaussian beam leads to the generation of higher-order Bessel beams. LG beams carry orbital angular momentum (OAM) which is dependent on the order of the topological charge, l. They are generated using a spatial light modulator. The grayscale phase pattern as well as the corresponding LG beam obtained experimentally is illustrated in Fig. 3.

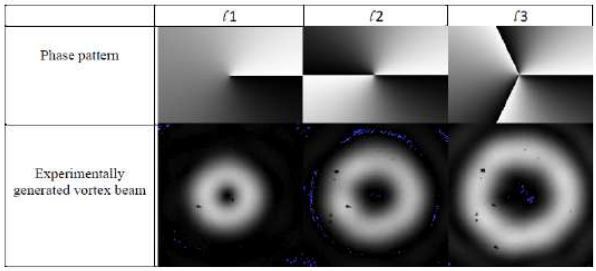

Fig.3: Grayscale phase patterns for the different order vortex beams as well as the corresponding vortex beam.

It can be deduced that Higher-order Bessel beams are composed of a Bessel beam engulfed by a LG Beam hence they also carry OAM. Fig.4 illustrates the experimental results obtained for different higher-order Bessel beams in the near- and far-field.

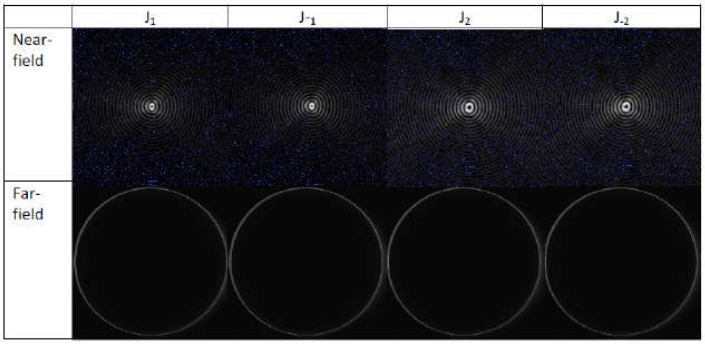

Fig.4: Near- and far-field images of Higher-order Bessel beams.

The higher the order of the Bessel beam, the greater the amount of OAM carried by the beam. As in the case of zero-order Bessel beams, higher-order Bessel beams also exist for a finite region as well as they are non-diffracting.

3. Z-DEPENDENT BESSEL-LIKE BEAMS

This abrupt change in intensity distribution from the near- to far-field can be considered a disadvantage to such beam and can be avoided using a double axicon and lens system illustrated in Fig.5. Upon propagating a well collimated Gaussian beam through axicon, Ax_1 and a spherical lens of focal length F, a conical field is produced. The conical field thereafter passes through the second axicon, Ax_2 which refracts the light rays in the direction of beam propagation such that the crossing angles, θ,decreases as the propagation distance increases. This implies that a Bessel function is still produced as $z \rightarrow \infty$.

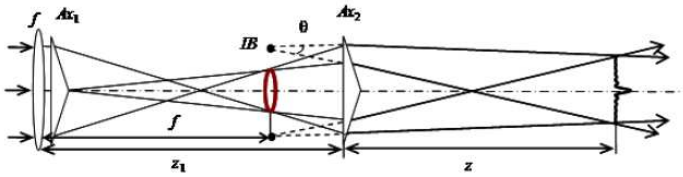

Fig.5: Optical design to generate z-dependent Bessel-like beams

4. CONSIDERING A MATHEMATICAL APPROACH TO EXPLAINING Z-DEPENDENT BLB'S

The stationary phase method is implemented in order to confirm that the field entering the second axicon is conical. From Fresnel integral the field at the input plane of the second axicon is defined by Eq. 3,

$$a_1(\rho, z_1) = -\frac{i}{\lambda z_1}\exp\left(\frac{ik_0\rho^2}{2z_1}\right)\int_0^{2\pi}\int_0^{R_{a2}}\exp\left(-\frac{\rho_1^2}{\rho_0^2} - ik_0\gamma_2\rho_1 - \frac{ik_0\rho\rho_1}{z_1}\cos(\varphi-\varphi_1)\right)\rho_1^2 d\rho_1 d\varphi_1 \quad , \tag{3}$$

Where w_0 is the beam radius of the Gaussian beam, k_0 is the wave number is given by Eq.4

$$\frac{1}{\rho_0^2} = \frac{1}{w_0^2} + \frac{ik_0}{2F} - \frac{ik_0}{2z_1}, \tag{4}$$

Thereafter applying the stationary phase method, the above equation yields:

$$a_1(\rho, z_1) = -\frac{i\rho F^2}{(z_1-F)^2}\left(1-\frac{\gamma_2 z_1}{\rho}\right)^{3/2}\exp\left[\frac{ik_0}{2z_1}\left(\rho^2 + \frac{z_1/F-1+iz_1/z_0}{(z_1/F-1)^2+(z_1/z_0)^2}(\rho-\gamma_2 z_1)^2\right)\right] . \tag{5}$$

As calculated above the field some arbitrary distance z after the second axicon is thereafter determined from Eq. 6

$$a_2(\rho, z) = -\frac{i}{\lambda z}\int_0^{2\pi}\int_0^{R_{a2}} a_1 \exp\left(\frac{ik_0(\rho^2+\rho_1^2-2\rho\rho_1\cos(\varphi-\varphi_1))}{2z} - ik_0\gamma_2\rho_1\right)\rho_1^2 d\rho_1 d\varphi_1 \tag{6}$$

$$= \exp\left(\frac{ik_0\rho^2}{2R(Z)}\right)\left[g_+(\rho, z)\exp(ik_0\gamma(z)\rho) - ig_-(\rho, z)\exp(ik_0\gamma(z)\rho)\right] .$$

Where

$$g_\pm(\rho, z) = \frac{f}{2(z+z_1-f)}\sqrt{\gamma_2 - \gamma_1(1+\frac{z_1}{z}) \pm 1}, \tag{7}$$

$$R(z) = z\left[1+\frac{z}{z_1-f}\right] , \tag{8}$$

and we define:

$$\gamma(z) = \frac{\gamma_2 z_1 + (\gamma_1 - \gamma_2) f}{z_1 + z - f} \quad . \tag{9}$$

From the zero-order Bessel function of the first kind, $J_0 \approx \sqrt{\frac{2}{\pi z}} \cos(z - \frac{\pi}{4})$, Eq. 10 is attained

$$a_2(\rho, z) \approx \frac{1}{2} \sqrt{\frac{\pi k_0 \gamma(z) \rho}{2}} (g_+(\rho, z) + g_-(\rho, z)) \exp\left[\frac{ik_0}{2}\left[\frac{\rho^2}{z} + \frac{\rho^2}{R(z)} - \gamma^2(z) R(z)\right]\right] J_0\left[k_0 \gamma(z) \rho\right] . \tag{10}$$

Eq. 9 clearly shows that the cone angle, γ, is dependent upon the longitudinal distance z as well as it confirms that an increase in z will lead to decrease in the cone angle. Similarly the above mathematical approach can be carried out on higher-order z-dependent BLB's [6].

5. EXPERIMENTALLY GENERATED Z-DEPENDENT BESSEL-LIKE BEAMS

From the above in can be deduced that these beams are Bessel-like hence they are so named z-dependent Bessel-like beams. These beams are produced however at the expense of losing its non-diffracting nature which will be validated shortly. Incorporating the optical design outlined in Fig. 5 into an experimental setup results to the generation of BLB's in the near- and far-field illustrated in Fig. 6.

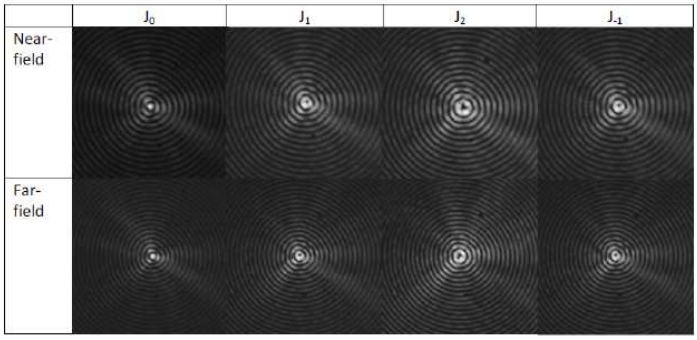

Fig. 6: z-dependent Bessel-like beams.

As mentioned previously z-dependent BLB's are produced at the loss of their non-diffracting nature. An experimental system was design to validate the above statement. It was observed that there is a linear increase in diffraction as the propagation distance was increased. The results obtained are illustrated in Fig. 7. It can be deduced that the higher the order of the BLB'S the quicker the beam diffracts.

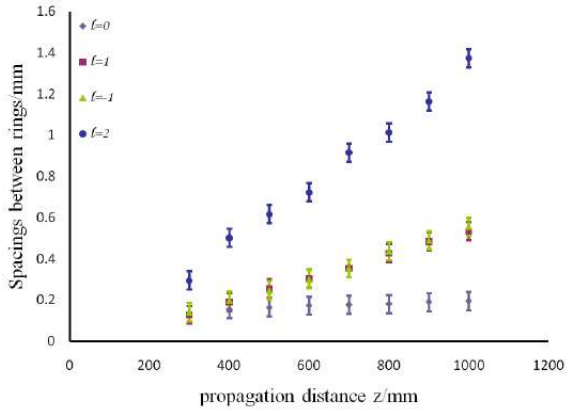

Fig. 7: Graph illustrating the divergence of z-dependent Bessel-like Beams.

6. CONCLUSION

Here it was shown that by the use of ordinary optical elements found in the laboratory, a new method for generating Bessel beams in the far-field is possible. This was achieved by basically varying the cone angle such that as $z \to \infty$, $\gamma \to 0$ hence zero- and higher-order Bessel-like beams in the far-field are easily reproducible. Conclusively this new design for generating long range z-dependent Bessel-like beams can be an advantage for many applications especially in optical trapping.

REFERENCES

[1] Durnin J., "Exact solution for nondiffracting beams: I. The scalar theory," J.Opt. Soc. Am, B 4(4), 651-654 (1987).
[2] Litvin I.A., McLaren M.G., and Forbes A., "A conical wave approach to calculating Bessel-Gauss beam reconstruction after complex obstacles," *Opt. Commun.*, **282**, 1078–1082 (2009).
[3] Bouchal z., Wagner J. and Chulup M.,"Self-reconstruction of a distorted nondiffracting beam," Opt. Commun. 151(4-6), 207-211 (1998)
[4] Vasara A., Turunen J. and Friberg A.T., "Realization of general nondiffracting beams with computer-generated holograms," J. Opt. Soc. Am. A6(11), 1748-1754 (1989)
[5] Belyi V., Forbes A., Kazak N., Khilo N. and Ropot P.,"Bessel-like beams with z-dependent cone angles," Opt. Express 18,1966-1973 (2010)
[6] Belyi V., Forbes A., Kazak N., Khilo N. and Ropot P.,"Higher-order z-dependent-Bessel-like beams," In preparation